Controlled Synthesis of Magnetic Particles

by

SU KYUNG SUH

B.S. Chemical Engineering, Pohang University of Science and Technology, South Korea (2005)

M.S. Chemical Engineering Practice, Massachusetts Institute of Technology (2008)

Submitted to the Department of Chemical Engineering
in partial fulfillment of the requirements for the degree of

Doctor of Philosophy in Chemical Engineering

at the

MASSACHUSETTS INSTITUTE OF TECHNOLOGY

December 2011
[February 2012]

Signature of Author.....
Department of Chemical Engineering
December, 2011

Certified by.....
T. Alan Hatton
Ralph Landau Professor of Chemical Engineering Practice
Thesis Supervisor

Certified by.....
Patrick S. Doyle
Professor of Chemical Engineering
Thesis Supervisor

Accepted by.....
William M. Deen
Carbon P. Dubbs Professor of Chemical and Biological Engineering
Chairman, Committee for Graduate Students

Abstract

Controlled Synthesis of Magnetic Particles

by
Su Kyung Suh

Submitted to the Department of Chemical Engineering on December 12th, 2011,
in partial fulfillment of the requirements for the degree of
Doctor of Philosophy in Chemical Engineering Practice

Magnetic particles have been used for many applications demanding a broad range of particles morphologies and chemistries. Superparamagnetism is advantageous over ferromagnetism because it enables us to control and recover magnetic nanoparticles during and after chemical processing. Superparamagnetic particles have an oriented magnetic moment under a magnetic field but lose this behavior in the absence of a field. Ferromagnetic materials can be superparamagnetic when they consist of a single size domain, which is on the order of 10s of nanometers. However, since the magnetic force is proportional to the volume of the particle, one needs to apply higher gradient of magnetic field to recover smaller particles. Therefore, large particles are preferred for easy manipulation using external forces. For this reason, the synthesis of large, superparamagnetic particles is very important and is desirable for future applications. The purpose of this work is (1) to examine the three synthesis methods of superparamagnetic units, (2) to understand the behavior of particles created using these methods as well as the synthesis mechanisms, and (3) to investigate the potential applications of these particles.

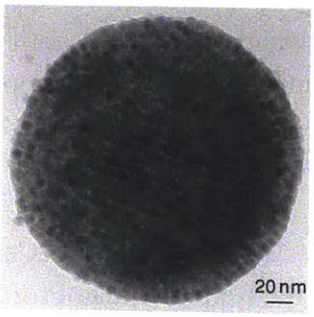

Large paramagnetic particles can be made by assembling superparamagnetic nanoparticles. We developed a method for the **process-dependent clustering of monodisperse magnetic nanoparticles** using a solvent evaporation method from solid-in-oil-in-water (S/O/W) type emulsions. When polymers that are incompatible with the nanoparticle coatings were included in the emulsion formulation, monolayer- and multilayer-coated polymer beads and partially coated Janus beads were prepared. The precise number of nanoparticle layers depended on the polymer/magnetic nanoparticle ratio in the oil droplet phase parent emulsion. The magnetic nanoparticle superstructures responded to the application of a modest magnetic field by forming regular chains with alignment of nonuniform structures (e.g., toroids and Janus beads) in accordance with theoretical predictions and with observations in other systems.

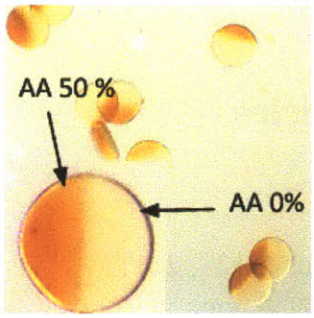

In addition, we synthesized **non-spherical magnetic microparticles** with multiple functionalities, shapes and chemistries. Particle synthesis is performed in two steps; polymeric microparticles homogenously functionalized with carboxyl groups were generated using **stop-flow lithography,** and then ***in situ*** **co-precipitation** was used to grow magnetic nanoparticle at these carboxyl sites. With successive growth of magnetic nanoparticles, we obtained polymeric particles with saturations magnetization up to 42 emu per gram of microparticle, which is significantly greater than what can be obtained commercially. We also investigated the physical properties of magnetic nanoparticles grown in polymeric microparticles, and provide an explanation of the properties.

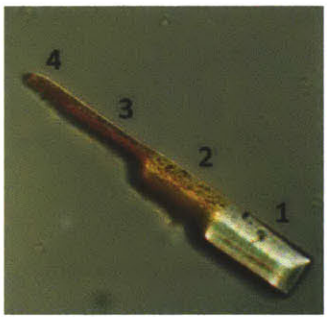

Lastly, we used experimentation and modeling to investigate the synthesis of opaque microparticles made via stop-flow lithography. Opaque **magnetic beads incorporated into hydrogel microparticles** during synthesis changed the height and the degree of cross-linking of the polymer matrices formed. The effect of the concentration of the opaque material on the particle height was determined experimentally, and agreed well with model predictions based on the photo-polymerization process over a wide range of UV absorbance. We also created particles with two independent anisotropies, magnetic and geometric, by applying magnetic fields during particle synthesis. Our work provides a platform for rational design of lithographic patterned opaque particles and also a new class of structured magnetic microparticles.

Overall, this work demonstrates three strategies for creating magnetic substrates containing superparamagnetic nanoparticles and characterization of their resulting properties.

Thesis Supervisor: T. Alan Hatton
Title: Ralph Landau Professor of Chemical Engineering Practice

Thesis Supervisor: Patrick S. Doyle
Title: Doherty Professor of Chemical Engineering Practice

Acknowledgments

Completing a Ph.D. degree is one of the biggest achievements in my life. It could not be finished without other's help. First, I would like to thank my advisors, Professor Hatton and Professor Doyle, for consistent support and direction. Without your confidence in me, I could not write this at this moment. Alan – thank you for your guidance, and for showing me how to put creativity into science. Pat – thank you for teaching me how to think problems logically and critically. Also, I would like to thank to my committee members, Prof. Love, Prof. Olsen, and Prof. Stellacci, for insights and helpful discussions. I would like to acknowledge Singapore-MIT Alliance for the generous funding and support to the projects.

I loved being a Hatton group member. Tatsushi – I enjoyed very much to work with you. You taught me many experimental skills and how to structure scientific problems. Fei – thank you for not only giving me a lot of scientific assistance but also cheering me up. I felt like having my older brother in my office. Ying – thank you for countless discussions and conversations over past five years. Asha, Kristin, Abhinav, Huan, and Smeet – thank you for being great neighbors in my office. Because of you, I could enjoy spending time every day. Nate, Emily, and Mike – thank you for being great safety managers.

There are many Doyle group members who have been helpful during my Ph.D. Rilla – thank you for working with me for magnetic micro particle project. I am so glad we finally made this project worked. Kai – thank you for making so many particles without any complaint. You are the greatest UROP I have ever met. Bong – thank you for initiating the opaque particle project.

Steve – thank you for your help about bioassays. Jason, Harry, Rathi, Matt, and Nakwon– thank you for your support especially when my experiment did not work.

Outside of Hatton and Doyle groups, I would like to thank Prof. van der Sande for discussions about TEM images. Dr. Chu, Dr. Yong, and Mr. Boisver – thank you for teaching me how to use equipments in DMSE centers. Suzanne, Katie and Joel, thank you for providing administrative helps.

Last but not least, I appreciate my family and friends for your endless support and love.

Table of Contents

List of Figures

List of Tables

Chapter 1

Introduction

The work written in this thesis involves three strategies for creating magnetic substrates containing superparamagnetic nanoparticles and characterization of their resulting properties. Magnetic particles have been used for many applications; to meet application broad range of needs, various types of particles morphologies and chemistries are desired. This chapter outlines (1) the usages of magnetic particles, (2) principles of magnetic particles, and (3) importance of larger magnetic units for various applications.

1.1 Magnetic particles

Magnetic particles are of increasing interest in chemical processes, due to their potential use in various fields, such as separations[1-3], catalysis[4], analysis[5] and diagnostics.[5] These applications are enabled by the ability to manipulate the particles under external magnetic fields, transfer energy selectively to magnetic particles using oscillating magnetic field, and to have large surface to volume ratio by reducing the size of magnetic particles, as shown in Figure 1-1. Because of these attributes, magnetic particles are an ideal model for controllable substrates.

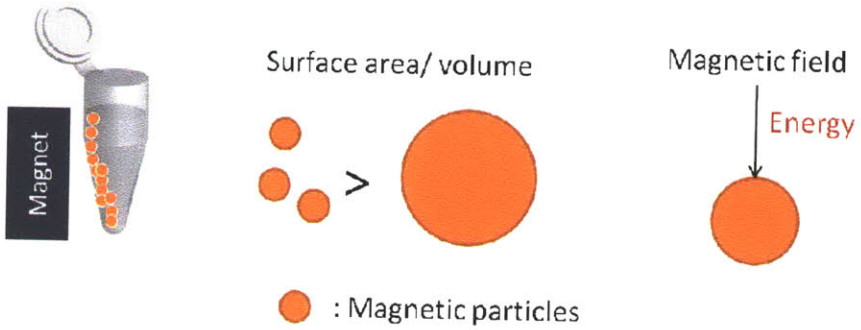

Figure 1-1: Properties of magnetic particles that enable many applications

1.2 Wide usage of magnetic particles

The most common application of magnetic particles is the separation of materials from complex mixtures.[2-3,6] The method of high gradient magnetic separation (HGMS) involves two successive processes, using special magnetic particles that have tuned adsorptive properties. HGMS is performed by attaching an adsorbent, which can selectively capture desired chemicals to the surface of magnetic nanoparticles. After the absorption, one can recover the magnetic particles and adsorbed molecules with a magnetic field. The recovered particles can be used several times, reducing the cost of the process.

Magnetic nanoparticles have been studied extensively for biomedical applications such as magnetic hyperthermia, and magnetic resonance imaging (MRI). Magnetic hyperthermia is a new type of cancer treatment which has several advantages over other therapies. As magnetic particles can absorb and release energy depending on the conditions of the magnetic field they are subjected to, they can be used to control local temperature using external oscillating fields. This property enables us to increase the temperature of specific locations within human body. In the presence of magnetic particles, magnetic particles have been used to increase the temperature tumor cells, either killing the cells or making them vulnerable.[7]

Magnetic particles can also be used as contrast agents. MRI is an imaging process for clinical diagnostics, measuring the magnetization of protons in water via time-varying magnetic fields. Different tissues have different water concentrations, creating contrast in imaging. The addition of magnetic nanoparticles in targeted area can either enhance or reduce this contrast to improve imaging for a desired area.[8-9]

Magnetic nanoparticles are also an attractive platform for ultra-high density information storage. The self assembly properties of magnetic nanoparticles can produce patterned media, which are required for digital data storage. The magnetic moment of each particle can have a different orientation, storing 1 bit.[10] In theory, storage media utilizing 10 nm-sized particles could have a storage capacity of about 1 terrabyte/in^2.[11]

1.3 Properties of magnetic particles

Magnetic particles exhibit unique properties. This section will describe a few basic theories about magnetization of superparamagnetic materials. Most information explained below is adapted from Rosensweig' book.[12]

1.3.1 Domains

Magnetic solids contain domains, which are defined by as regions of uniform magnetization. Each domain, in which the electric dipoles of all of the atoms are oriented in the same direction, is separated from other domains by a domain wall. As illustrated in Figure 1-2, crystals can have more than one domain.

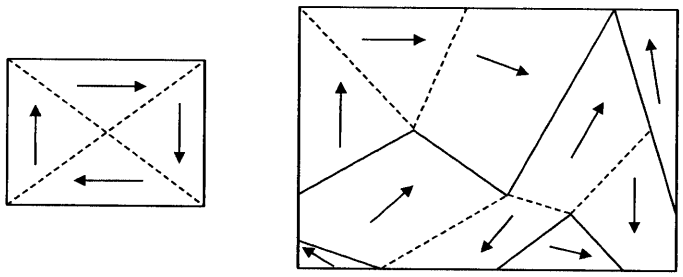

Figure 1-2: Domain structure for single crystal and polycrystalline. Dashed lines represent domain walls, while solid lines are crystal walls [12].

Magnetic materials create domains to minimize the field energy, ΔE_{MS}, but they cannot make infinite number of domains because the generation of domain walls requires a certain amount of energy, E_{DW}. Magnetostatic energy, ΔE_{MS}, is proportional to the volume of the particles, while domain wall energy increases proportionally to the area of domain walls. For small particles, the energy cost of making domain walls is greater than the magnetostatic energy reduction caused by

their creation; therefore, they have only a single domain. The maximum single domain particle size is called the critical diameter and occurs when $\Delta E_{MS} = E_{DW}$. The critical diameter can be expressed as follows,

$$D_c \approx 18\frac{\sqrt{AK_{eff}}}{\mu_0 M^2} \qquad (1\text{-}1)$$

where A is the exchange constant, K_{eff} is the anisotropy constant, μ_0 is the permeability of free space and M is the saturation magnetization.[12-13]

1.3.2 Hysteresis

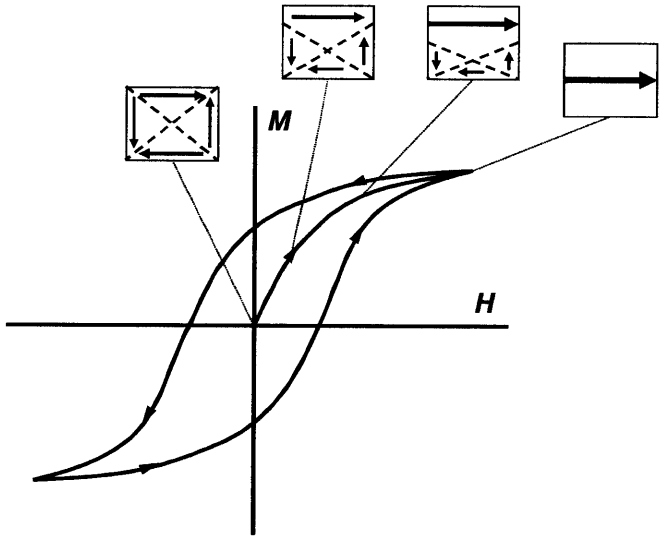

Figure 1-3: Hysteresis circle of a multi-domain magnetic particles and domain wall displacement in such a material.[12]

When a magnetic field is applied to single crystal particles with multiple domains, they initially exhibit domain displacement as shown in Figure 1-3, where ***H*** is the magnetic field strength and ***M*** is intensity of magnetization. This corresponds to the arrow starting from origin in Figure 1-3. After magnetic saturation of the particles, particles will still exhibit some magnetization even if the magnetic field is reduced to back to zero. This offset amount is called the retentivity or remanence. This behavior, ferromagnetism, is an example of hysteresis and can be observed in particles with multiple domains. The existence of hysteresis is not preferred for applications requiring precise control of magnetic particles. Single domain magnetic particles, termed

superparamagnetic materials, do not exhibit hysteresis, making them advantageous for such applications.

1.3.3 Stability requirements

Magnetic fluids are colloidal single phase dispersions that respond rapidly to external forces due to their short time and length scales for equilibration. For colloidal magnetic fluids, colloid stability should be considered carefully depending on the application. Magnetic particles having long chain molecules on their surface are more stable than those without such stabilizers. They prevent van der Waals attraction via steric repulsion. The stabilizers are usually chosen to have similar properties to the surrounding fluid. The stability of the colloidal particle suspension is affected by various energies, including thermal, magnetic, gravitational, dipole-dipole contact and dipole fluctuation energies. The expressions for these energies are the following, where k is Boltzmann's constant, L is the elevation in the gravitational field, A is the Hamaker constant, l is surface-to-surface separation distance between particles over radius of particles.

$$\text{Thermal energy} = kT$$

$$\text{Magnetic energy} = \mu_0 MHV$$

$$\text{Gravitational energy} = \Delta\rho VgL$$

$$\text{Dipole} - \text{dipole contact energy} = \frac{1}{12}\mu_0 M^2 V$$

$$\text{Dipole fluctuation energy} = -\frac{A}{6}\left[\frac{2}{l^2+4l}+\frac{2}{(l+2)^2}+\ln\frac{l^2+4l}{(l+2)^2}\right]$$

Considering the stability against settling of particles, particles will prefer to be separated, rather than aggregated, in field-free space when:

$$\frac{\text{thermal energy}}{\text{magnetic energy}} = \frac{kT}{\mu_0 MHV} \geq 1$$

The above equation is equivalent to following criterion:

$$d \leq \left(6kT / \pi\mu_0 MH\right)^{1/3} \qquad (1\text{-}2)$$

At room temperature, Fe_3O_4 is known to be stable when d $\leq$ 8.1 nm according to the equation above. The relative stability of magnetic fluids against other forces can be calculated similarly using the previous equation with the energy expressions given. Also, the dipole fluctuation

energy equation indicates that prevention of contact is important. Steric hindrance of stabilizers can block the particle contact.[12]

1.3.4 Magnetization

In the absence of a magnetic field, the magnetic moment of each particle is oriented randomly. Thus, the average magnetization is zero. However, magnetic moments start aligning with as a magnetic field is and thermal energy is overcome. The torque density acting on magnetic moments in a magnetic field can be expressed as

$$\tau = mH \sin\theta \tag{1-3}$$

where m is the magnetic dipole moment and θ is the angle between the applied magnetic field and magnetic moment. The expended energy to rotate particles from an initial angle to 0 requires integration from 0 to θ,

$$W = \int_0^{\theta} \tau d\theta = mH\left(1-\cos\theta\right) \tag{1-4}$$

The Boltzmann distribution assumes that the probability of a given state is proportional to $e^{-W/kT}$ when the associated energy of that state is W. Therefore, average magnetization is,

$$\overline{m} = \langle m\cos\theta \rangle = \frac{\int_0^{\pi} m\cos\theta \exp\left(mH\cos\theta / kT\right)\sin\theta d\theta}{\int_0^{\pi} \exp\left(mH\cos\theta / kT\right)\sin\theta d\theta} \tag{1-5}$$

After this integration, the resulting relationship is

$$\frac{M}{\phi M_d} = \coth\alpha - \frac{1}{\alpha} \equiv L(\alpha) \tag{1-6}$$

where ϕ is the volume fraction of magnetic solids in the fluid, M_d is the saturation magnetization of the bulk material, $\alpha = \pi\mu_0 MHd^3/6kT$ and $L(\alpha)$ is denoted as the Langevin function. This relationship describes the magnetization of non-interacting superparamagnetic particles, displaying saturated curves at high field strengths and a linear region in low fields.[12]

1.3.5 Relaxation

1.3.5 Relaxation

Since magnetic nanoparticles are used for many applications, it is important to understand the properties of relaxation. There are two magnetization relaxation mechanisms acting on colloidal ferrofluids in the presence of a change in applied field. They are Brownian relaxation and Neel relaxation. The rotation of particles in the fluid produces Brownian relaxation, which has a characteristic rotational diffusion time, τ_B, of,

$$\tau_B = 3V\eta_0 / kT \qquad (1\text{-}7)$$

where η_0 is the viscosity of the carrier fluid. Neel relaxation is the rotation of the magnetic moment vector within the particle, independent of any particle movement. The Neel relaxation characteristic time, τ_N, is

$$\tau_N = \frac{1}{f_o}\exp\left(\frac{K_{eff}V}{kT}\right) \qquad (1\text{-}8)$$

where f_0 is a frequency, approximately 10^9 Hz. When $K_{eff}V \ll kT$, the energy barrier for moment rotation is much smaller than the thermal energy, and thus the moment can be flipped easily by thermal energy.

In the case where $\tau_N \ll \tau_B$, relaxation is governed by Neel relaxation process and the material is considered to exhibit intrinsic superparamagnetism. For the opposite case, the relaxation is dominated by the Brownian mechanism and the material is said to possess extrinsic superparamagnetism.[12,14]

1.4 Importance of large magnetic units with superparamagnetism

As we discussed above, superparamagnetism is advantageous over ferromagnetism because it enables us to control and recover magnetic nanoparticles during and after chemical processing. Superparamagnetic particles have an oriented magnetic moment under a magnetic field but lose this behavior in the absence of a field. Ferromagnetic materials can be superparamagnetic when they have single size domain, namely, small particle size (~20 nm).[12] However, since the magnetic force is proportional to the volume of the particle, one needs to apply higher gradient of magnetic field to recover smaller particles. Therefore, large particles are more easily manipulated by external forces than are small particles. In this situation, synthesis of large, superparamagnetic particles is very important and is desirable for future applications. Therefore,

ability to create large magnetic units would provide large improvements in the performance over the previously mentioned materials.[2]

1.5 Current methods to create bigger magnetic units

Large paramagnetic particles can be made by assembling superparamagnetic nanoparticles, or by dispersing such magnetic nanoparticles throughout a unit's matrix. The first approach utilizes the clustering of nanoparticles, which can be achieved via self assembly of nanoparticles [15-17] or by using emulsions as templates.[18-19] Depending on the application, further coating or functionalization can be achieved. Clusters can be cores or shells.[20-21] The second approach relies on the incorporation of nanoparticles within porous structures. Magnetic nanoparticles can be grown[22-24] or entrapped in polymer matrices.[25-27] While magnetic nanoparticle clusters tend to exhibit higher saturation magnetization than polymer-based paramagnetic particles due to higher magnetic material density, polymer substrates provide great flexibility in terms of chemical functionality and mechanical properties.

1.5.1 Assemblies of magnetic nanoparticles

Initially, assemblies of metallic nanoparticles were investigated when developing methods to stabilize nanoparticles in solutions in order to prevent aggregation. In the absence of ligands, nanoparticles tend to form clusters spontaneously, which is energetically favorable. With sufficient amounts of ligand, nanoparticles tend to stay as discrete particles, while those with less ligand aggregate to form clusters.[15,28-30] Furthermore, many research groups have used chemical or physical forces between ligands such as hydrogen bonding[31], dipole interaction[32], or electrostatic forces[33] in order to build interesting structures. For example, gold nanoparticles coated with single stranded DNA can be built to structures via interaction with complementary DNA as shown in Figure 1-4.[34]

Another method for assembly involves the use of templates. Emulsions are one example. When emulsions contain magnetic nanoparticles, they separate nanoparticles from the continuous phase.[16,18-19,35] The discontinuous phase, containing the nanoparticles, can be concentrated to form nanoparticle clusters. This method can be applied to various metallic and non-metallic nanoparticles. The main advantage is that emulsion based self-assembly can be applied to a broad range of particles, with no chemistry dependence so long as the particles can be contained within emulsions. Using solid-in-oil-in water emulsions as a colloidal template, one can precisely control the clusters as shown in Figure 1-4.

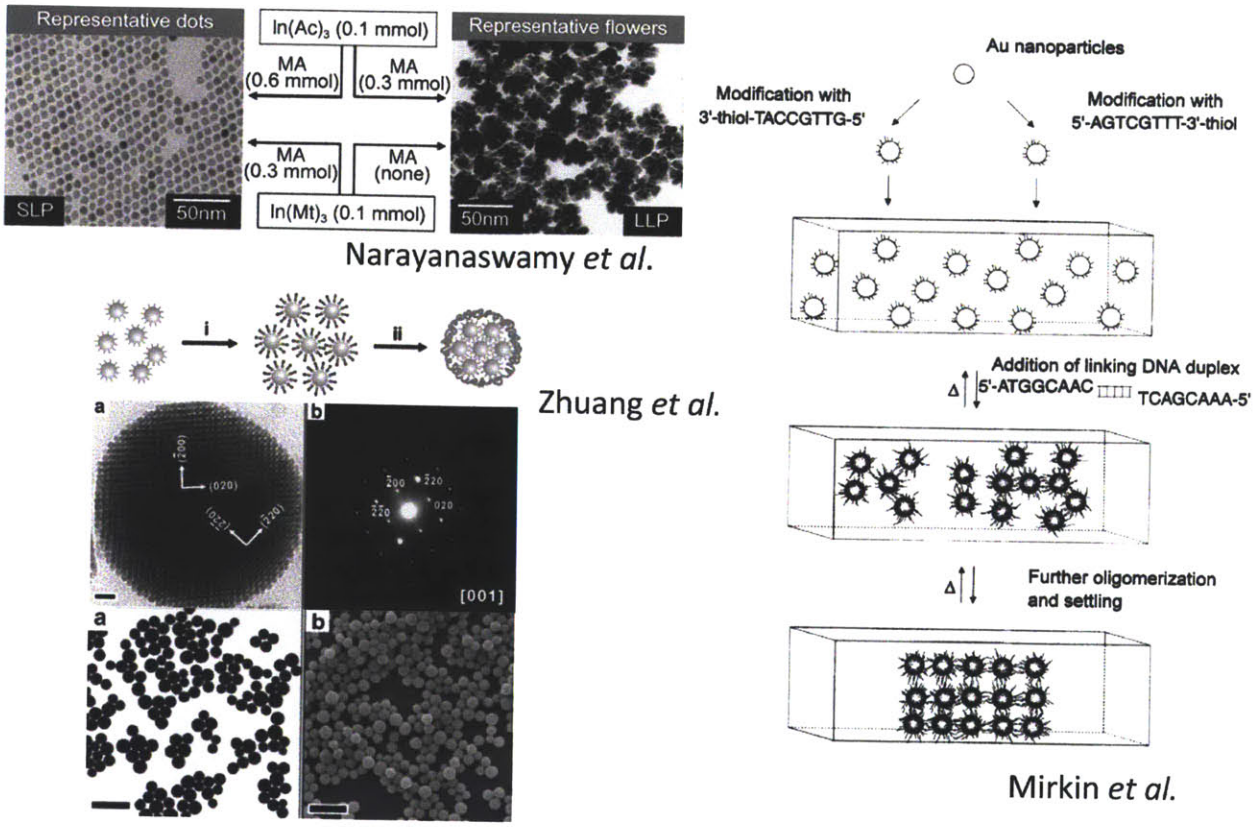

Figure 1-4: Examples of nanoparticle assemblies. Controlling amount of ligands [28], interaction of ligands [34] or using emulsions [19], nanoparticles can be assembled to bigger units.

1.5.2 Polymer templated magnetic particles

When using the bottom-up methods for cluster formation described in the previous section, it is difficult to create micron-scale clusters with well-controlled structure. For this reason, various techniques to include nanoparticles in bigger polymer particles have been explored. Preformed magnetic nanoparticles can be embedded in polymer particles to create structural hierarchy. In one example, magnetic nanoparticles were mixed into monomer solutions, such that during polymer particle formation via polymerization, the nanoparticles were entrapped.[24-25,27,36] Another approach is to absorb nanoparticles into swollen polymeric matrices.[37-38] Typically, polymers attract nanoparticles via electrostatic interactions. However, these techniques that

utilize preformed nanoparticles are not readily compatible with high nanoparticle loadings, often resulting in nanoparticle aggregation.[39]

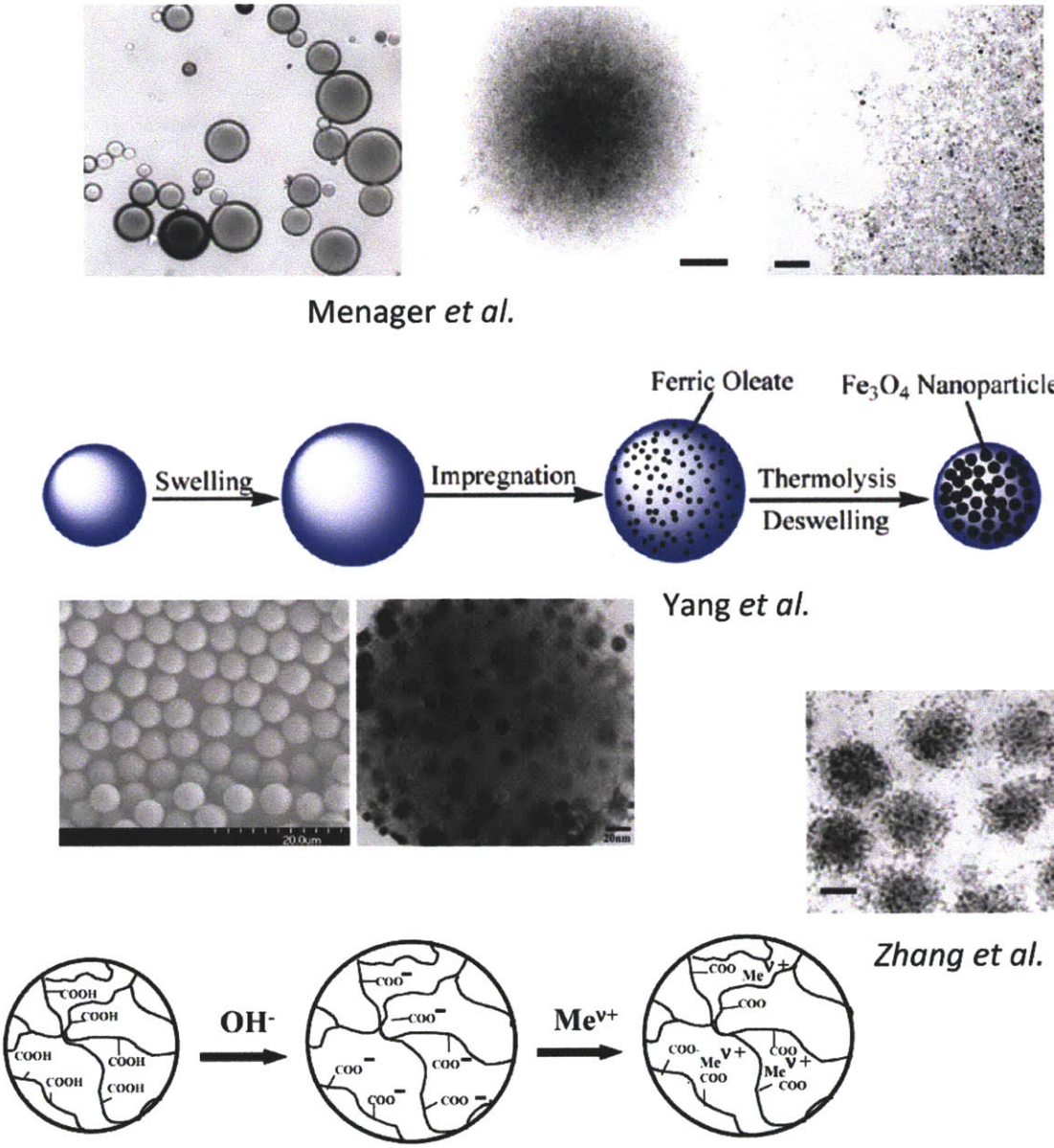

Figure 1-5: Magnetic particles generated with polymer templates. Menager *et al.* performed emulsion polymerizations in the presence of magnetic nanoparticles [27]. Yang *et al.* [26] and Zhang *et al.* [23] reported *in-situ* synthesis of magnetite in polymeric particles.

One of the approaches to overcome the challenge of high nanoparticle loading is to use *in-situ* magnetic nanoparticle synthesis within polymer matrices. Ugelstad *et al.* have reported magnetic nanoparticle precipitation in the pores of swollen polystyrene microspheres.[22] For hydrophilic magnetic particles, cationic polymers were utilized as templates to attract ferrous or ferric ions in the particles.[23,40] Using these templates, the precipitation of magnetic nanoparticles in polymer were performed using external stimuli, temperature and pH. Many of these methods are used to create commercially-available beads used in biomedical applications.

1.6 Research overview

The purpose of this work is to examine the three synthesis methods of superparamagnetic units, to understand the behavior of particles created using these methods as well as the synthesis mechanisms, and to investigate the potential applications of these particles. The organization of this work is following:

Chapter 2 describes clustering superparamagnetic nanoparticles into controlled structures.

Chapter 3 explains *in-situ* precipitation of magnetic nanoparticles in polymeric microparticles.

Chapter 4 describes the polymerization of hydrogel particles in the presence of magnetic beads and the development of a mathematicl model of the process.

Chapter 5 discusses potential application of the magnetic particles created using these methods for biomolecule detection and building secondary structures.

Chapter 6 outlines the findings of this thesis and discusses future work.

1.7 Reference

(1) Miltenyi, S.; Müller, W.; Weichel, W.; Radbruch, A. *Cytometry* **1990**, *11*, 231.

(2) Bucak, S.; Jones, D. A.; Laibinis, P. E.; Hatton, T. A. *Biotechnol Progr* **2003**, *19*, 477.

(3) Ditsch, A.; Lindenmann, S.; Laibinis, P. E.; Wang, D. I. C.; Hatton, T. A. *Ind Eng Chem Res* **2005**, *44*, 6824.

(4) Stevens, P. D.; Fan, J.; Gardimalla, H. M. R.; Yen, M.; Gao, Y. *Organic Letters* **2005**, *7*, 2085.

(5) Gupta, A. K.; Gupta, M. *Biomaterials* **2005**, *26*, 3995.

(6) Miltenyi, S.; Muller, W.; Weichel, W.; Radbruch, A. *Cytometry* **1990**, *11*, 231.

(7) Mornet, S.; Vasseur, S.; Grasset, F.; Duguet, E. *J Mater Chem* **2004**, *14*, 2161.

(8) Berry, C. C.; Curtis, A. S. G. *Journal of Physics D: Applied Physics* **2003**, *36*, R198.

(9) Pankhurst, Q. A.; Connolly, J.; Jones, S. K.; Dobson, J. *J Phys D Appl Phys* **2003**, *36*, R167.

(10) Ross, C. Annual Review of Materials Research **2001**, 31, 203.

(11) Zhou, H.; Narayan, J. *J Nanopart Res* **2006**, *8*, 595.

(12) Rosensweig, R. E. *Ferrohydrodynamics*; Dover Publications: Mineola, N.Y., 1997.

(13) Lu, A. H.; Salabas, E. L.; Schuth, F. *Angew Chem Int Edit* **2007**, *46*, 1222.

(14) Frenkel, J. *The kinetic theory of liquids*; Dover: New York, 1955.

(15) Ditsch, A.; Laibinis, P. E.; Wang, D. I. C.; Hatton, T. A. *Langmuir* **2005**, *21*, 6006.

(16) Ge, J.; Hu, Y.; Yin, Y. *Angewandte Chemie* **2007**, *119*, 7572.

(17) Lattuada, M.; Hatton, T. A. *J Am Chem Soc* **2007**, *129*, 12878.

(18) Bai, F.; Wang, D.; Huo, Z.; Chen, W.; Liu, L.; Liang, X.; Chen, C.; Wang, X.; Peng, Q.; Li, Y. *Angewandte Chemie International Edition* **2007**, *46*, 6650.

(19) Zhuang, J. Q.; Wu, H. M.; Yang, Y. A.; Cao, Y. C. *J Am Chem Soc* **2007**, *129*, 14166.

(20) Shang, H.; Chang, W. S.; Kan, S.; Majetich, S. A.; Lee, G. U. *Langmuir* **2006**, *22*, 2516.

(21) Lambert, E. M.; Viravaidya, C.; Li, M.; Mann, S. *Angewandte Chemie* **2010**, *122*, 4194.

(22) Ugelstad, J.; Berge, A.; Ellingsen, T.; Schmid, R.; Nilsen, T. N.; Mork, P. C.; Stenstad, P.; Hornes, E.; Olsvik, O. *Prog Polym Sci* **1992**, *17*, 87.

(23) Zhang, J. G.; Xu, S. Q.; Kumacheva, E. *J Am Chem Soc* **2004**, *126*, 7908.

(24) Kroll, E.; Winnik, F. M.; Ziolo, R. F. *Chemistry of materials* **1996**, *8*, 1594.

(25) Hwang, D. K.; Dendukuri, D.; Doyle, P. S. *Lab Chip* **2008**, *8*, 1640.

(26) Yang, C. L.; Shao, Q.; He, J.; Jiang, B. W. *Langmuir* **2010**, *26*, 5179.

(27) Menager, C.; Sandre, O.; Mangili, J.; Cabuil, V. *Polymer* **2004**, *45*, 2475.

(28) Naravanaswamy, A.; Xu, H. F.; Pradhan, N.; Peng, X. G. *Angew Chem Int Edit* **2006**, *45*, 5361.

(29) Shen, L.; Laibinis, P. E.; Hatton, T. A. *Langmuir* **1999**, *15*, 447.

(30) Liu, B.; Zeng, H. C. *J Am Chem Soc* **2004**, *126*, 8124.

(31) Boal, A. K.; Ilhan, F.; DeRouchey, J. E.; Thurn-Albrecht, T.; Russell, T. P.; Rotello, V. M. *Nature* **2000**, *404*, 746.

(32) Klajn, R.; Bishop, K. J. M.; Fialkowski, M.; Paszewski, M.; Campbell, C. J.; Gray, T. P.; Grzybowski, B. A. *Science* **2007**, *316*, 261.

(33) Kalsin, A. M.; Fialkowski, M.; Paszewski, M.; Smoukov, S. K.; Bishop, K. J. M.; Grzybowski, B. A. *Science* **2006**, *312*, 420.

(34) Mirkin, C. A.; Letsinger, R. L.; Mucic, R. C.; Storhoff, J. J. *Nature* **1996**, *382*, 607.

(35) Iskandar, F.; Gradon, L.; Okuyama, K. *Journal of colloid and interface science* **2003**, *265*, 296.

(36) Xulu, P. M.; Filipcsei, G.; Zrinyi, M. *Macromolecules* **2000**, *33*, 1716.

(37) Chung, T. H.; Pan, H. C.; Lee, W. C. *Journal of Magnetism and Magnetic Materials* **2007**, *311*, 36.

(38) Sauzedde, F.; Elaissari, A.; Pichot, C. *Colloid & Polymer Science* **1999**, *277*, 846.

(39) Xu, X.; Majetich, S. A.; Asher, S. A. *J Am Chem Soc* **2002**, *124*, 13864.

(40) Huang, J.; Wan, S.; Guo, M.; Yan, H. *J. Mater. Chem.* **2006**, *16*, 4535.

Chapter 2

Controlled synthesis of magnetic nanoparticles clusters

2.1 Introduction

As methods to synthesize monodisperse nanoparticles bearing ligands have been successfully developed, self-assemblies of nanoparticles became a tool to create new materials with well-ordered structures.[1] Monodisperse magnetic nanoparticles can be generated through thermal decomposition of organometallic compounds in high boiling-point organic solvents containing stabilizing surfactants.[2] This approach is known to provide tight control over size and shape. Methods using metal acetylacetonates, metal cupferronates, or carbonyl as metal precursors have been reported[3-5] using fatty acid, oleic acid or hexadecylamine as stabilizers to disperse particles in non-polar solvents. Furthermore, it is possible to obtain a range of nanocrystal size and shape by using precursors of the correct reactivity and concentration.[6]

When magnetic nanoparticles are stabilized with hydrophobic ligands, a solid in oil in water (S/O/W) type emulsions can be used to contain nanoparticles and the desired polymers.[7-8] Solvent evaporation of the S/O/W emulsions results in nanoparticle/polymer clusters with controlled morphologies.[9-10] Recently, the synthesis of micro-sized colloidal crystal spheres made using latex beads was reported.[11-12]

This chapter presents a solvent evaporation method to produce monomdisperse, spherical magnetic nanoparticle clusters with controlled packing patterns such as crystalline or amorphous

superlattices, and doughnut-shaped structures. Using this method, we produce monolayer and multilayer-coated polymer beads as well as Janus nanoparticles. These clusters, which are 100s of nanometers in dimension, respond to applied magnetic fields, forming chain structures as predicted with theory. Here, we describe our approaches used to form these structures and control their morphologies and demonstrate a more rapid processes utilizing pervaporation. The material in this chapter was reproduced from Isojima, Suh, vander Sande and Hatton, *Langmuir*, 2009.[13]

2.2 Experimental setup

2.2.1 Materials

Iron tri(acetylacetonate) ($Fe(acac)_3$) (97%), 1,2-tetradecanediol (90%), oleic acid (OA) (90%), oleyl amine (OAm) (70%), benzyl ether (99%), sodium dodecyl sulfate (SDS) (99%), hexane (99%), and polyethylene (PE) (M_w: 35000) were purchased from Sigma Aldrich. Methanol (99.8%) and chloroform (100%) were purchased from Mallinkrodt. Polystyrene (PS) (M_w: 125000 - 250000) was purchased from Alfa Aesar. All water utilized in the experiments was Milli-Q (Millipore) deionized water.

2.2.2 Synthesis of magnetic nanoparticles

Magnetic Fe_3O_4 nanoparticles were prepared by using Sun's method[2] with minor modifications. Before thermal decomposition, iron tri(acetylacetonate) (2 mmol), 1,2-tetradecanediol (10 mmol), oleic acid (6 mmol), oleylamine (6 mmol), and benzyl ether (20 ml) was mixed under constant flow of nitrogen for 30 min to prevent oxidization. The temperature of the solution was gradually increased to 100 °C and maintained for 30 min. The solution was then heated to 200 °C and kept there for 40. Finally, the mixture was refluxed (~290 °C) for 1 hr and then cooled to room temperature. Figure 2-1 shows the temperature setpoint over time. All heating processes were performed under nitrogen blanket. After heating and subsequent cooling, 40 ml of methanol was added; the solution was centrifuged and aspirated to remove benzyl ether and un-reacted ligands. The precipitate was dispersed in 20 ml hexane and centrifuged again to remove any un-dispersed residue. The magnetic nanoparticles were precipitated with excess methanol and separated using an electromagnet. The ethanol and hexane were removed by drying the solution at 80 °C. The dried nanoparticles were dispersed in hexane as concentration of 3 wt% and sonicated for 3 mins.

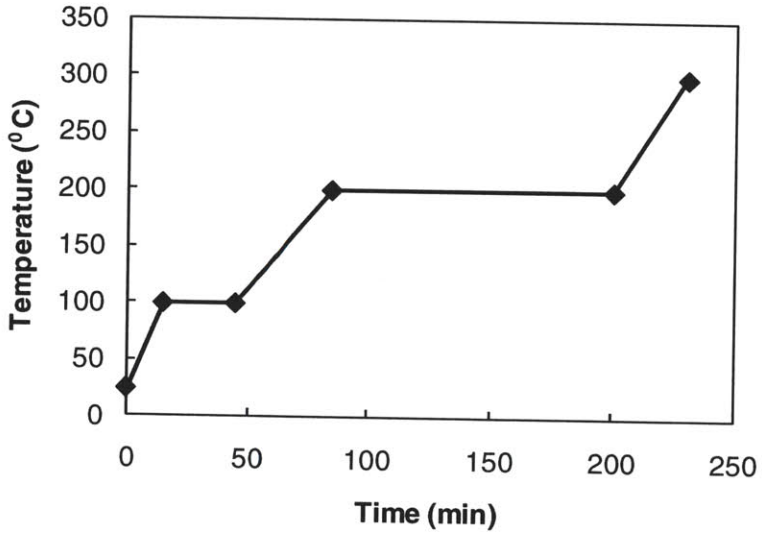

Figure 2-1: Temperature control to create monodisperse magnetic nanoparticles

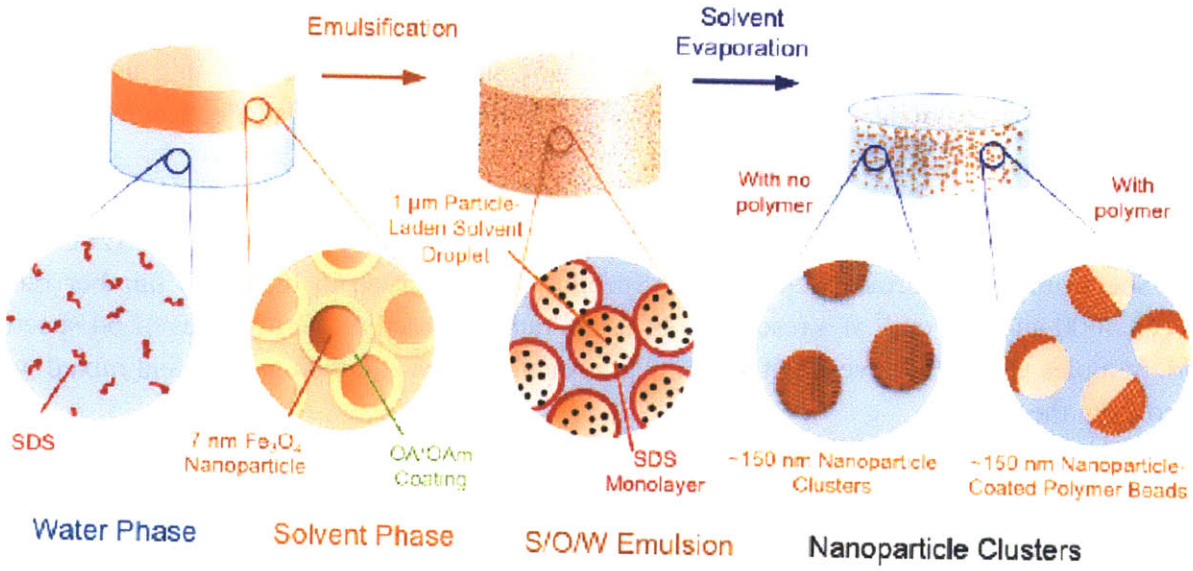

Figure 2-2: Schematic of the synthesis procedure for the preparation of magnetic nanoparticle clusters.

2.2.3 *Clustering of magnetic nanoparticles*

A 0.3 ml dispersion of magnetic nanoparticles in hexane was mixed with 10 ml of 1 wt% SDS to create S/O/W emulsions. This mixture was then homogenized for 30s using an ultrasonic homogenizer. Finally hexane was evaporated under mechanical stirring using specific temperatures and durations to achieve the desired result.

2.2.4 *Magnetic nanoparticle coated polystyrene beads*

For mono- and multi-layer coated polystyrene (PS) beads, we added 0.3 ml of a mixture containing PS (3.0 wt % for a mono-layer or 0.7 wt % for multi-layer) and magnetic nanoparticles (3.0 wt %) in chloroform into 10 ml of 1 wt% SDS aqueous solution. To make Janus spheres, we added 0.3 ml of a mixture containing magnetic nanoparticles (either 1.0 or 1.5 wt %) and 3.0 wt % PS in chloroform into 0.3 ml of hexane. After mixing, the solutions were kept in homogenizer for 30s. Chloroform and hexane were evaporated under mechanical stirring at 40 °C for 12 hr.

2.2.5 *Characterizations*

Transmission and Scanning Electron Microscopy (TEM and SEM). TEM and SEMwere performed using JEOL 200CX or JEOL 6320FV with accelerating voltages of 200 kV and 5kV, respectively. Samples were prepared by dropping an aqueous solution containing nanoparticle clusters on carbon-coated and lacey carbon-coated, 200-mesh copper grids (Electron Microscopy Sciences).

Fourier Transform Infrared Spectroscopy (FTIR.) FTIR was performed using the NEXUS 870 FTIR Spectrometer (Thermo Nicolet Inc.). Spectra were observed in the wave number range between 4000 and 400 cm^{-1} at a resolution of 2 cm^{-1} and recorded as the averages of 64 spectral scans. Samples were dried overnight at 80 °C in a vacuum oven and then ground and mixed with KBr to form the pellets.

Thermogravimetric Analysis (TGA). TGA was performed using a Q50 (TA Instruments) under a constant flow of mixture gas of nitrogen (90ml/min) and helium (10ml/min). The samples were heated at a rate of 15 °C /min. The temperature range for the measurements was between 30 °C and 600 °C. Samples were prepared by drying in a vacuum oven overnight at 80 °C prior to analysis.

Dynamic Light Scattering (DLS). DLS was performed using a Brookhaven BI-200SM (Brookhaven Instruments Corporation) with the measurement angle set at 90°. The Contin program was chosen from the DLS correlation functions to determine hydrodynamic diameter.

Zeta Potential Measurements. All zeta potential measurements were performed using a zeta potential analyzer (Brookhaven ZetaPALS, Brookhaven Instruments Corporation). We used the Smoluchowski equation to calculate the zeta potential from the electrophoretic mobility.

Gaussmeter. A carbon-coated TEM grid was placed in the center of the parallel two permanent magnets in order to assemble magnetic nanoparticle clusters under a uniform external magnetic field. A gaussmeter (Bell-5180, Sypris Solutions, Inc.) was used to measure the magnetic field, which had a magnitude of 160 mT.

2.2.6 Pervaporation

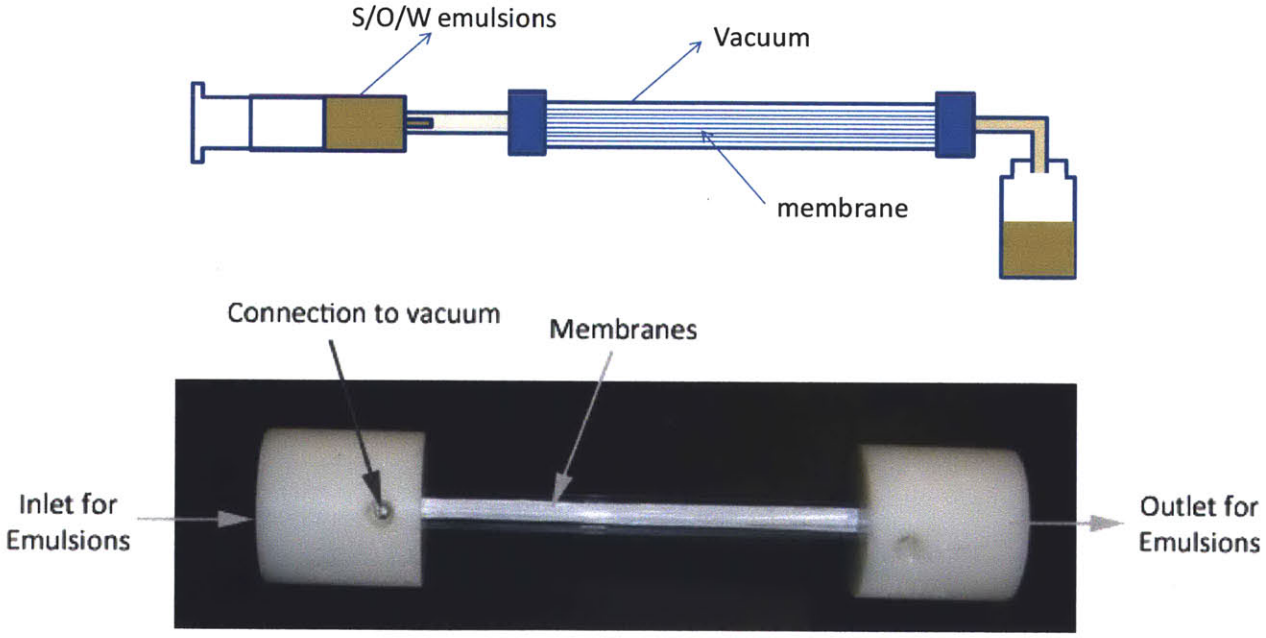

Figure 2-3: Pervaporation unit. At the center, the unit has 120 fibers with a diameter of 300 μm.

Pervaporation units were purchased from AMT Inc (MPV-XX-01). This mini module contains 120 polysiloxane membrane fibers each with a diameter of 300 μm in order to allow the rapid

permeation and evaporation of hexane under vacuum. The white center part of the apparatus in Figure 2-3 is the bundle of membrane fibers. The transparent sleeve around the bundle is a chamber that controls evaporation by the application of a vacuum or other gases for selective evaporation. With volumetric flow rate of 0.1 ml/min, S/O/W emulsions were injected in to the pervaporation unit under vacuum. For a longer residence time, the process was repeated, with complete evaporation of the oil phase typically after 60 min.

2.3 Result and discussions

2.3.1 Magnetic nanoparticles

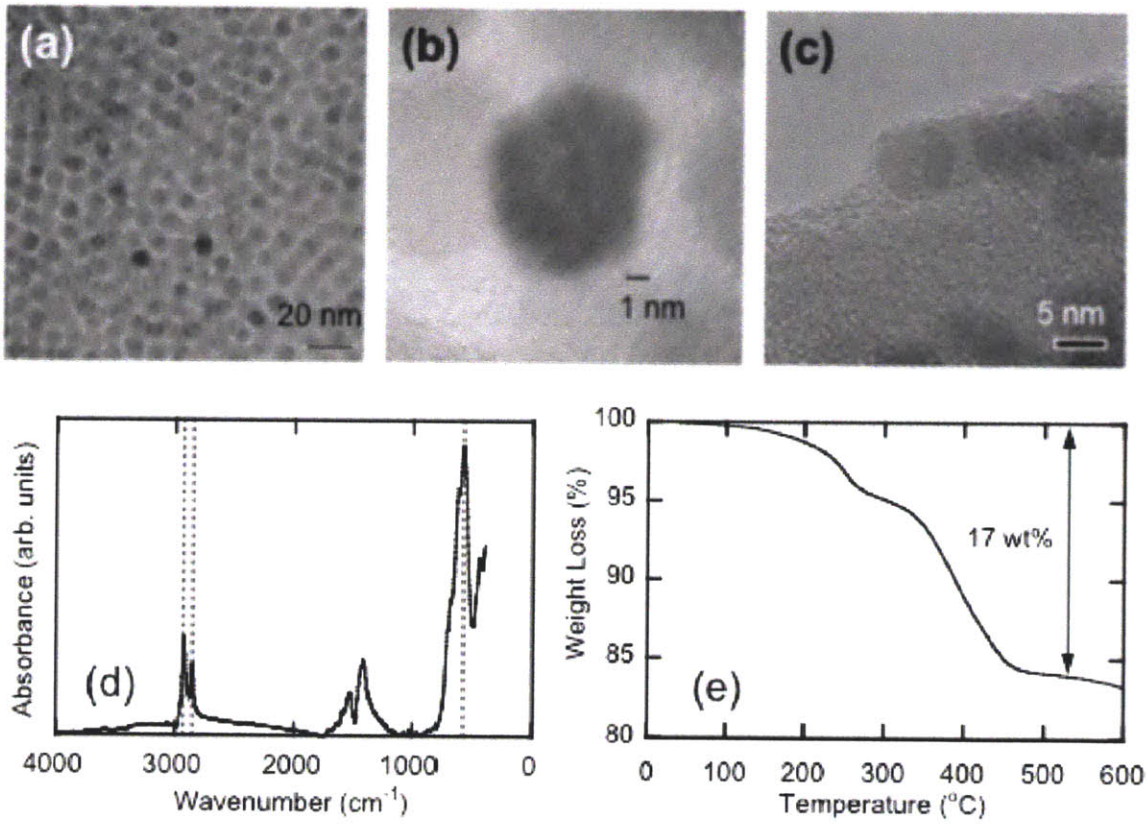

Figure 2-4: TEM images of magnetic nanoparticles and their characterization. (a) TEM images of magnetic nanoparticles (b) HR-TEM showing atomic planes of nanoparticles (c) HR-TEM showing stabilizers OA/OAm (d) FTIR measurement (e) TGA measurement.

Monodisperse 7 nm magnetic nanoparticles, stabilized in a non-polar organic solvent with a mixture of oleic acid and oleyl amine (OA/OAm) surface monolayer, were synthesized using the method provided by Sun *et al.*[2] The synthesis of monodisperse, single crystal structures is important as these structures act as the building block for nanoparticles. As shown in Figure 2-4 (a), the nanoparticles have narrow size distribution with a diameter of 7 nm. To increase the contrast between nanoparticles and stabilizer, we used lacey carbon grids or thin perforated carbon films instead of carbon film TEM grids. The resulting TEM images are shown in Figure 2-4 (c). Individual nanoparticles are in the form of hexagons with an OA/OAm shell of ~0.5nm. According to the FTIR spectrum of the OA/OAm magnetic nanoparticles in Figure 2-4 (d), the magnetite (Fe_3O_4) has adsorption band at 586 cm^{-1} and OA/OAm has the bands at 2852 and 2927 cm^{-1}. The OA/OAm bands originate from methylene groups present. TGA measurements indicate that the OA/OAm account for 17 wt% of the total nanoparticle mass.

2.3.2 Clusters of magnetic nanoparticles

Self-assembled structures of clusters made using 7 nm magnetic nanoparticles were controlling by adjusting the solvent evaporation temperature of hexane in the S/O/W emulsion shown in Figure 2-2. Depending on the evaporation temperature, the resulting secondary particles could be categorized as Nanoparticles Crystal (NPC), Nanoparticles Amorphous (NPA) and Nanoparticles Doughnut (NPD). NPC was prepared by removing hexane at room temperature for 3 days, while NPA and NPD are created at 60 °C for 12 hours and 80 °C for 8 hours, respectively. With slow evaporation of hexane from the S/O/W emulsion, we obtained a crystal like structure. The slow evaporation allowed nanoparticles to move to a close packed structure with a low energy configuration. At 40 °C, we observed a polycrystal structure as shown in Figure 2-5 (c). Interestingly, this configuration appears both for clusters and single magnetite particles. The superimposed figure at the top of the single magnetite image in Figure 2-6 (b) was obtained from Figure 2-6 (a). Additionally, the black small circles in Figure 2-6 (b) are a group of atomic plane, while Figure 2-6 (a) includes magnetic nanoparticles.

When the oil phase solvent was removed more rapidly at 60 °C, the particles could not organize in a well order structure, resulting in an amorphous structure. At 80 °C, which is higher than the boiling point of hexane, the magnetic nanoparticles immediately form clusters that encapsulate a hexane liquid core. Vaporized hexane escapes from the core to outside of the S/O/W emulsion, which results in the formation of doughnut-like structures. The sizes of the emulsion are about 1 μm and secondary particles formed after evaporation are stabilized by the negative charge (-60 to -90 mV) of the surfactant, SDS. The zeta potentials of each cluster type are listed in Table 2-1. Alkyl chains on the surface of magnetic nanoparticles participate in both nanoparticle-nanoparticle and nanoparticle–surfactant interactions, which stabilize the self-assembled clusters.

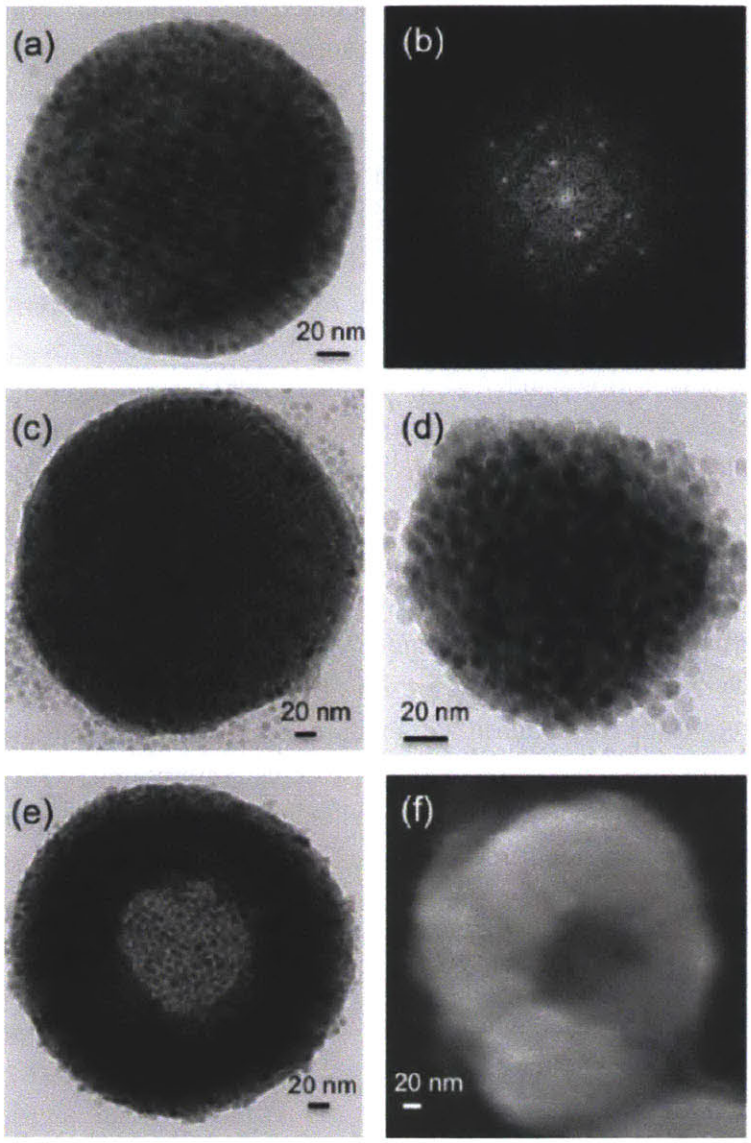

Figure 2-5: Magnetic nanoparticle clusters: (a) TEM image of a single-domain crystalline superlattice formed at low temperature (25 °C), (b) fast Fourier transform diffraction pattern for particles in (a) showing BCC (110) structure, (c) TEM image of a multidomain crystalline superlattice formed at intermediate temperatures (50 °C), (d) TEM image of amorphous cluster formed at higher temperatures (60 °C), and (e) TEM image and (f) SEM image of toroidal structures formed at 80 °C, above the solvent boiling point. The TEM image in (e) was paired with an image of the same cluster tilted at an angle of 30° for stereoscopic visualization to show that the toroidal aggregates have a true doughnut-like structure.

When the evaporation process is performed at room temperature for 3 days, the nanoparticles are arrayed with well-ordered structures resulting in NPC formation. We confirmed the structure of NPC using TEM as shown in Figure 2-5(a). We also confirmed the super lattice structure of the magnetic nanoparticles. The FFT (Fast Fourier Transform) image of the inside of the NPC is shown in Figure 2-5(b). The single crystal spot indicates (110) of the BCC (Body Centered Cubic). If the evaporation is performed at 60 °C for 8 hrs, magnetic nanoparticles in the emulsion can not be arrayed with a well-order structure, resulting in particles with an amorphous structure. The structure of NPA is confirmed in Figure 2-5(c). The FFT image in Figure 2-5(d), indicates a homogenous (disordered) structure of NPA. With a rapid hexane evaporation at 80 °C for 8hr, a doughnut like structure was observed. Considering that the boiling point of hexane is 69 °C, the rapid evaporation condition can be defined as when this. We hypothesize that doughnut structures are formed through a transitional structure with hollow cores surrounded by shells of nanoparticles that are ruptured when trapped hexane is released from the emulsion core. The NPD structure is confirmed in Figure 2-5(e) and (f). Figure 2-5(f) was taken by tilting the particle in Figure 2-5(e) at an angle of 30°. We confirmed the doughnut structures of Figure 2-5(e) and (f) by Stereoscope (Type F-71, Forestry Suppliers Inc.).

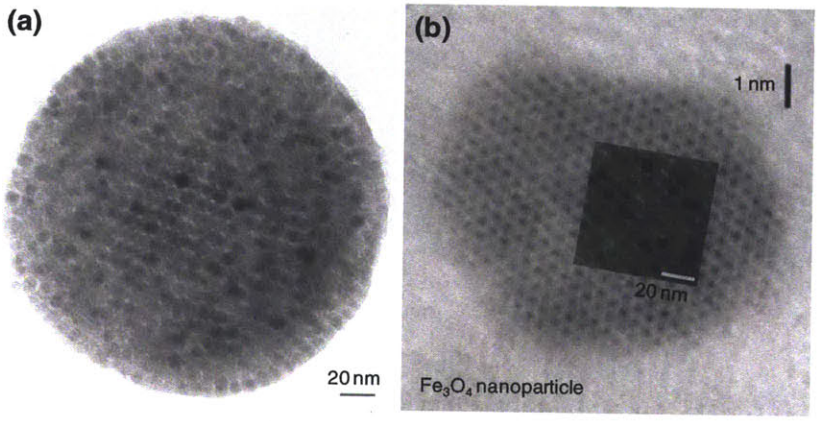

Figure 2-6: Nanoparticle lattice mirrors molecular ordering. (a) TEM image of nanoparticle clusters (b) HR-TEM image of magnetic nanoparticles. Inset image is from (a)

2.3.3 Magnetic nanoparticle coated polymer beads

We used chloroform as a non-polar, volatile organic solvent because PS has poor solubility in hexane. Both chloroform and hexane dissolve magnetic nanoparticles with shells bearing alkyl chains. We used specific concentrations of PS and magnetic nanoparticles to obtain different morphologies, namely monolayer, multilayer-coated, and Janus type PS beads. Before evaporation of the non-polar solvent, PS and magnetic nanoparticles are in a homogeneous state. As the oil phase solvent evaporates, solvophophic interactions between water and PS makes the PS condense. This action forces magnetite to deposit on the PS surface, pushing the magnetic nanoparticles out. We can control the ratio of PS and magnetic nanoparticles. If we estimate that the PS beads are 100nm in diameter, and the magnetic nanoparticles are 7 nm in diameter, the required ratio of magnetic nanoparticles to PS would be about 6 (volume ratio), or ~1.2 (weight ratio: using 1.0 g/cm^3 as PS density and 5.2 g/cm^3 as Fe_3O_4 density respectively) to achieve a monolayer coating.

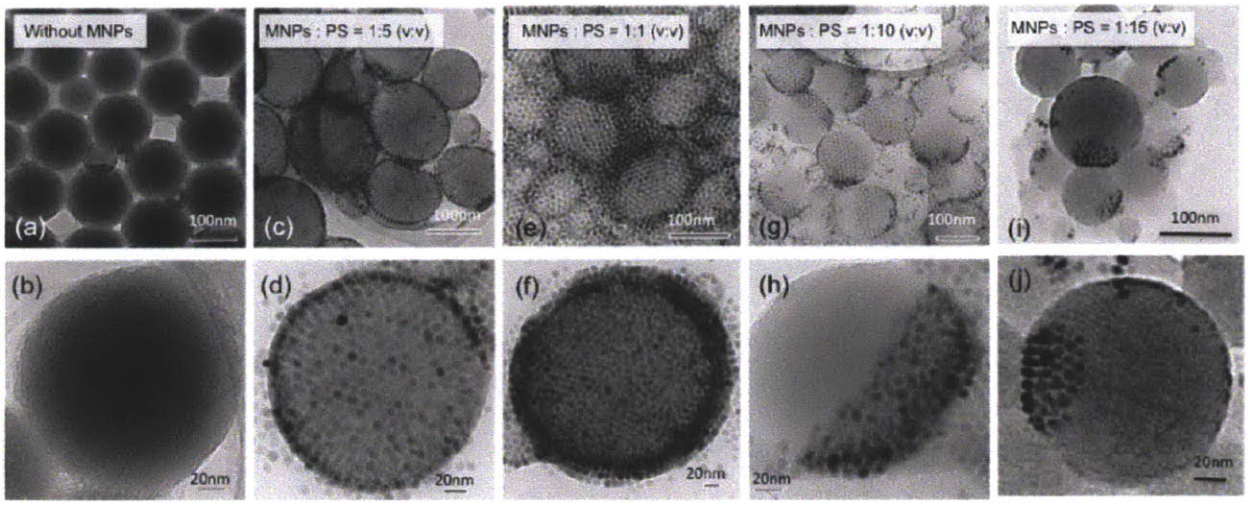

Figure 2-7: Magnetic nanoparticle coated polymer bead. (a, b) beads without nanoparticles, (c, d) monolayer-coated beads, (e, f) bilayer-coated beads, (g-j) Janus beads with different surface coverages depending on the initial nanoparticle/polystyrene ratio. In (g)-(j), the solvent used was a mixture of hexane and chloroform.

For Janus clusters, we used a mixture of chloroform and hexane as the non-polar organic solvent. Chloroform evaporates faster than hexane because of the lower boiling point (61.4 °C for chloroform). PS is segregated from hexane because it is a poor solvent for PS but good one for the magnetic nanoparticles. Finally, magnetic nanoparticles are arrayed on one side of the PS

beads, forming Janus clusters. If chloroform was used as the only solvent for the Janus clusters, the magnetic nanoparticles tend to be arrayed randomly on the PS bead, resulting in patchy bead formations. The solvent evaporation methods for S/O/W emulsions allow us to create PS beads coated with monodisperse magnetic nanoparticles by mixing the PS in the oil phase.

Figure 2-7 shows different types of magnetite-coated PS with various ratios of magnetic nanoparticles to PS. The monolayer coated PS beads with magnetic nanoparticles are confirmed in Figure 2-7 (a) and (b). The estimated volume fraction of PS against magnetic nanoparticles is about 5 for PS beads with a monolayer magnetic nanoparticle shell. The dark edge of the PS beads is the monolayer magnetic nanoparticles shell. Figure 2-7 (c) and (d) show the multilayer-coated PS beads (the estimated volume ratio of PS to magnetic nanoparticles is about 1). In this case, the shell of magnetic nanoparticles is darker than the monolayer case. The Janus-type clusters covered with magnetic nanoparticles only in certain portions of the PS are clearly seen in Figure 2-7 (e) and Figure 2-7 (f) (the estimated volume fraction of PS to magnetic nanoparticles is about 10). When we used polyethylene (PE) instead of PS with PE/magnetic nanoparticle ratios of 5, the monolayer PE beads were also confirmed. These techniques are useful tools for encapsulation, which can be used in applications such as targeted drug delivery systems.

Table 2-1. Zeta potential and DLS

	Zeta potential (mV)	**Hydrodynamic diameter (nm)**
PS bead	-74.5	174
NPC	-62.3	170
NPA	-89.0	154
NPD	-68.4	184
Mono- layer PS bead	-77.9	176
Multi-layer PS bead	-60.8	121
Janus PS bead	-72.2	155

2.3.4 Assemblies of magnetic clusters and magnetic particle coated PS

The PS/magnetic nanoparticle clusters can be arrayed using weak external magnetic fields (160 mT). Singh predicted ring-type clusters such as NPD under an external magnetic field, concluding that the magnetic rings are linked together along their edge in the direction of the applied magnetic field because of the minimum energy configuration with the direction of the

applied field.[14] Our results corroborate this prediction. The arrangement of the secondary particles of NPC and NPD under external magnetic field is confirmed in (a), (d) and (b), (c), respectively. Under an external magnetic field, the Janus clusters can be arrayed in the direction of the field as shown in (c) and (f). The Janus clusters interact with each other forming a zigzag chain structures.

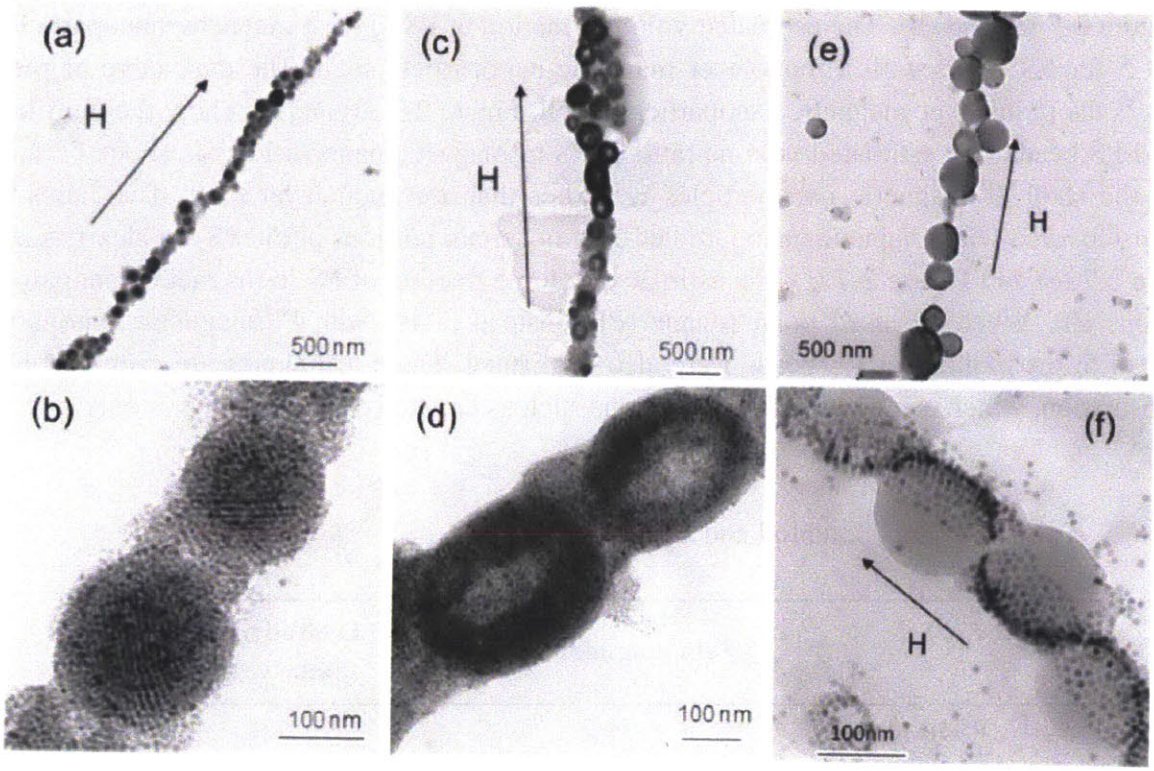

Figure 2-8: Nanowire with clusters under magnetic field: (a, b) crystalline superlattices, (c, d) toroidal clusters, and (e, f) Janus beads.

2.3.5 Evaporation using the pervaporation unit

While the evaporation process can bring great control over the morphologies of nanoparticle clusters, the procedures reported were lengthy and inefficient, with typical experimental times of 8 to 24 hours. Pervaporation can be used to speed up the removal of the oil phase solvent using vacuum as a driving force to selectively pull that solvent through a membrane. When we remove the oil phase solvent using pervaporation, the process takes only 1 hour to generate nanoparticle crystals. To monitor the process, we observed the clusters with TEM every 20 min, as shown in Figure 2-9. When emulsions contain solvent, the nanoparticles exhibit Brownian motion. Therefore, the outside of particles spread out during the preparation of TEM samples. The

boundary of the clusters becomes better defined and the nanoparticles pack more closely as time goes by. After 1 hour of pervaporation, most of the hexane in the emulsions was removed. Comparing to 24 hours using the previous evaporation process, pervaporation significantly reduces the time for solvent removal. Although the structure of clusters might not be as well-ordered as observed from our previous process, we think the fast process is very useful for applications because the clusters have similar superparamagnetic properties.

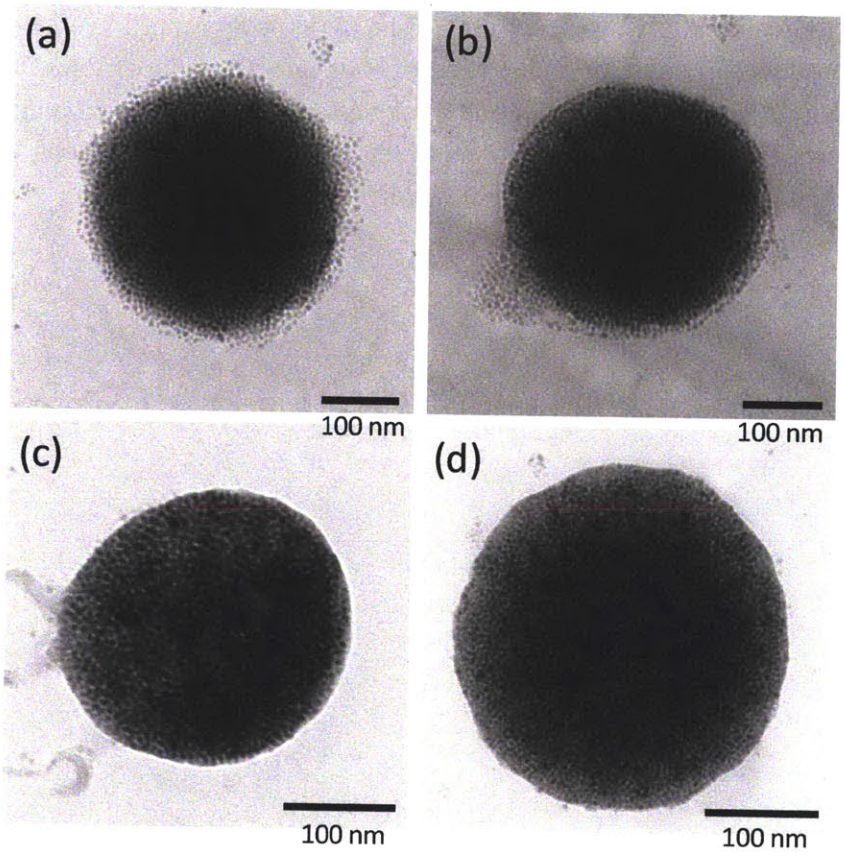

Figure 2-9: TEM images of clusters obtained for processing times of 20, 40, 60 and 180 minutes respectively. The surfaces become less diffuse with longer contact times as the clusters are dried more thoroughly. Scale bars are 100nm.

2.4 Conclusion

In summary, we report the synthesis of spherical nanoclusters with OA/OAm-coated 7 nm monodisperse magnetic nanoparticles, resulting in NPC, NPA, and NPD morphologies. We made monolayer and multilayer-coated polymer beads, and Janus clusters through a novel solvent evaporation method in S/O/W emulsion. The NPC, NPA, and NPD were made by controlling the evaporation speed of the oil phase using set evaporation temperatures of room temperature, 60 °C, and 80 °C, respectively. The monolayer, multilayer and Janus cluster formation were produced depending on the ratio of PS/magnetic nanoparticles in the oil phase of the S/O/W emulsion. This simple technique is a versatile and powerful method for creating uniquely structured self-assembled nanoparticles through manipulation of the surface interactions between the magnetic nanoparticles, solvent and polymer.

2.5 References

(1) Lu, A. H.; Salabas, E. L.; Schuth, F. *Angewandte Chemie-International Edition* **2007**, *46*, 1222.

(2) Sun, S.; Zeng, H. *Journal of the American Chemical Society* **2002**, *124*, 8204.

(3) Rockenberger, J.; Scher, E. C.; Alivisatos, A. P. *J Am Chem Soc* **1999**, *121*, 11595.

(4) Farrell, D.; Majetich, S. A.; Wilcoxon, J. P. *The Journal of Physical Chemistry B* **2003**, *107*, 11022.

(5) Jana, N. R.; Chen, Y.; Peng, X. *Chemistry of materials* **2004**, *16*, 3931.

(6) Li, Z.; Sun, Q.; Gao, M. *Angewandte Chemie International Edition* **2005**, *44*, 123.

(7) Shang, H.; Chang, W. S.; Kan, S.; Majetich, S. A.; Lee, G. U. *Langmuir* **2006**, *22*, 2516.

(8) Andersson, N.; Kronberg, B.; Corkery, R.; Alberius, P. *Langmuir* **2007**, *23*, 1459.

(9) Saito, N.; Kagari, Y.; Okubo, M. *Langmuir* **2006**, *22*, 9397.

(10) Kietzke, T.; Neher, D.; Kumke, M.; Ghazy, O.; Ziener, U.; Landfester, K. *Small* **2007**, *3*, 1041.

(11) Velev, O. D.; Lenhoff, A. M.; Kaler, E. W. *Science* **2000**, *287*, 2240.

(12) Prevo, B. G.; Kuncicky, D. M.; Velev, O. D. *Colloids and Surfaces A: Physicochemical and Engineering Aspects* **2007**, *311*, 2.

(13) Isojima, T.; Suh, S. K.; Sande, J. B. V.; Hatton, T. A. *Langmuir* **2009**, *25*, 8292.

(14) Singh, H.; Laibinis, P. E.; Hatton, T. A. *Langmuir* **2005**, *21*, 11500.

Chapter 3

In-situ co-precipitation of magnetic nanoparticles in microgels

3.1 Introduction

The ability to make superparamagnetic particles with precise control over particle morphology is desirable for many applications. As the induced mechanical stress on magnetic particles can be controlled by an external magnetic field, magnetic particles with various shapes enable researchers to study simplified versions of complex systems.[1-2] Also, non-spherical magnetic particles introduce magnetic anisotropies in the system, which allow the assembly of complex structures such as flowers, double helices and zigzag chains.[3-7] With the ability to control the shapes and functionalities of the building blocks used for assembly, the interaction between the components can be engineered precisely. Up to now, the synthesis of non-spherical magnetic particles has been achieved primarily using soft lithography in the presence of magnetic nanoparticles.[8-11] Unfortunately, magnetic nanoparticles absorb a considerable amount of the UV irradiation used to cure the particles, preventing photolysis and thus limiting the number of magnetic nanoparticles successfully incorporated into the polymeric particles.

As particles with lower magnetization require higher magnetic fields to yield reasonable response times, it is desirable to create particles with the maximum possible superparamagnetic properties. Here, we demonstrate a versatile method to generate complex, non-spherical magnetic particles with high magnetization. The Doyle group has developed a method to create hydrogel particles with configurable shapes and chemistries via Stop-Flow-Lithography (SFL).[12] Using SFL, we synthesized polymeric particles bearing carboxyl groups capable of capturing

ferric and ferrous ions which were then co-precipitated to form magnetic nanoparticles embedded within the polymeric particle matrices. We generated multifunctional particles of varying magnetic content by successive growth of magnetic nanoparticles within the gel matrix, which procedure can be used to increase the saturation magnetization to up to 42 emu/g of total microparticles. The mechanism of successive growth has been elucidated to explain the increase of saturation magnetizations both nanoparticles and polymer/nanoparticles. The material in this chapter was reproduced from Suh, Yuet, Hwang, Bong, Doyle and Hatton, *JACS*, in revision.

3.2 Experimental method

3.2.1 Materials

Polymeric particles are made from poly(ethylene glycol) (700) diacrylate (PEG-DA 700, Sigma-Aldrich), acrylic acid (AA, Sigma-Aldrich) and 2-hydroxy-2-methylpropiophenon (Darocur 1173, Sigma-Aldrich) initiator. Tween-20 (Sigma Aldrich) was used at 0.05% to prevent particle loss due to sticking on pipette tips or tubes. To synthesize magnetic nanoparticles, we used ferric chloride hexahydrate ($FeCl_3 \cdot 6H_2O$, Sigma Aldrich), ferrous chloride tetradydrate ($FeCl_2 \cdot 4H_2O$, Sigma Aldrich), sodium hydroxide (NaOH, Sigma Aldrich) and ammonium hydroxide (NH_4OH, Sigma Aldrich).

3.2.2 Microfluidic fabrication

Microfluidic devices for SFL were fabricated with polydimethyl-siloxane elastomer (PDMS, Sylgard 184, Dow Corning) mixed at a ratio of 10:1 base to curing agent. The PDMS microchannels were molded by pouring elastomer on the patterned silicon wafer (SU-8 photoresist, Microchem) and baking in an oven at 65 ^{0}C for 2 hours. PDMS-coated glass slides used for the bottom of the devices were prepared by spreading a thin layer of elastomer on a slide and partially curing at 65 ^{0}C for 22 mins. The clean PDMS patterns from the wafer were assembled with the glasses and they were kept in the oven for 45 mins. The prepared microfluidic channel was assembled with inlets that were made of pipette tips (ART 10 Reach and ART 200, Molecular BioProducts, Inc) and outlet aluminum tubing (1/16", K&S) for collecting particles after synthesis. For particle synthesis, the channels were placed on an inverted microscope (Axiovert 200, Zeiss).

3.2.3 Stop-flow-lithography setup

We polymerize micro particles in microfluidic devices when flow is stopped. Then, particles are pushed out of the polymerization area with flow of the monomer solutions. This stop-expose-

flow cycle was commanded by a custom script that toggled a solenoid valve (Burkertt) to control the inlet pressure on the monomer streams from 0 psi to 3 psi and opened or closed a UV shutter (VS25, UniBlitz). Monomer solutions were polymerized with the UV source of Lumen 200 (Prior Scientific, 100 % setting). A UV filter (11000v2, Chroma) was used to provide the desired excitation for polymerization. Transparency masks (Bandon, OR) designed in AUTOCAD 2005 were used to shape the UV illumination used for particle synthesis. For multiple inlets, the thickness of inlet streams was controlled by a pressure valve (ControlAir, Inc) and a digital pressure gauge (DPG 100G, Omega Engineering, Inc.).

3.2.4 Polymeric particle synthesis

Homogenous micro particles were prepared from oligomer solutions consisting of 50% (v/v) AA, 45% (v/v) PEG-DA 700 and 5% (v/v) Darocur 1173. The Janus particles were obtained using two monomer solutions, one with 50% (v/v) AA, 45% (v/v) PEG-DA 700 and 5% (v/v) Darocur 1173 and the other with 45 % (v/v) PEG-DA 700, 5% (v/v) Darocur 1173 and 50 % (v/v) water. For the preparation of multi-compartmented particles, our inlet solutions contained 0, 15, 30 and 45 % (v/v) of AA, and 50, 35, 20 and 5 % (v/v) of water respectively in monomer solutions. The polymerization time was 75 ms for all particles.

3.2.5 In-situ magnetic nanoparticle synthesis

The schematic diagram in Figure 1 shows the co-precipitation process. The clean polymer particles were dispersed in 0.5 M NaOH solution for 10 mins to deprotonate the COOH group to COO^-. Particles with COO^- were washed 5 times with 0.5 % Tween 20 solution to reach neutral pH. 0.2 M $FeCl_3$ and 1 M $FeCl_2$ solutions was prepared in N_2 purged water and mixed with the polymer particles to meet the desired ratio of Fe^{3+} : Fe^{2+} = 1 : 75. After iron ions diffused into the polymer particles and were allowed to chelate with the deprotonated carboxyl groups for 30 mins, the excess iron salts were removed. Following adjustment of the pH with NH_4OH at 60 ^{0}C, magnetic nanoparticles nucleated and grew in the polymer particles. The magnetic microparticles were rinsed 5 times with Tween 20 solutions. For successive growth, the steps from the deprotonation were repeated.

3.2.6 Characterizations

The magnetization of particles in the applied magnetic field was measured using a *Superconducting Quantum Interference Device* (SQUID, MPMS-5S, Quantum Design). All SQUID measurements were performed at 300 K over the magnetic field range of 0 to 5 Tesla on 1 – 3 mg of dried particles. *Transmission Electron Microscopy* (TEM, 200-CX, JEOL) images were obtained at 200 kV. The samples were prepared by placing thin-sliced particles on lacey

carbon-coated 200 Mesh copper grids (Electron Microscopy Sciences). Dried micro particles were cured in Epoxy (Sigma Aldrich) for 24 hrs and were sliced with a Micotome (MT-X, Ultra Microtome) with a thickness of 40 nm. *Scanning Electron Microscopy* (SEM, 6060, JEOL) was used to analyze the surfaces of dried particles. Samples were prepared by dropping 10 µl of particle solution on the glass slides.

3.3 Results and discussion

3.3.1 Non spherical magnetic microparticles

We demonstrate the synthesis of magnetic microparticles using *in-situ* growth of nanoparticles in polymer particles pre-formed by SFL. Our approach provides a versatile, inexpensive method for obtaining multifunctional and non-spherical magnetic particles with strong magnetic properties. The PEG/PAA polymeric particles investigated in this study were synthesized using SFL as shown in Figure 3-1. We blended acrylic acid in our PEG monomer precursor in order to introduce anionic carboxyl groups in the polymeric particle substrate, which could act as iron ion binding sites for nanoparticle growth. We also generated Janus particles using SFL with two monomer streams (Figure 3-1); the top stream is composed of PEG-DA and photo initiator, while the bottom stream includes PEG-DA, AA and photo initiator. These Janus particles enable selective adsorption of ions only in one particle region.

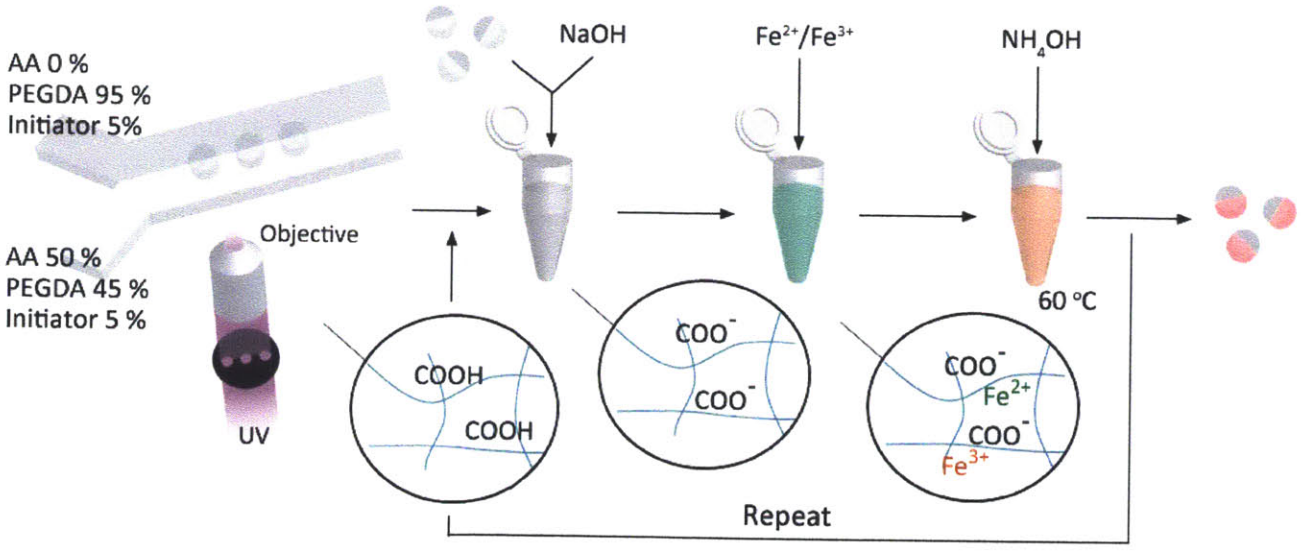

Figure 3-1: Schematics showing the synthesis process.

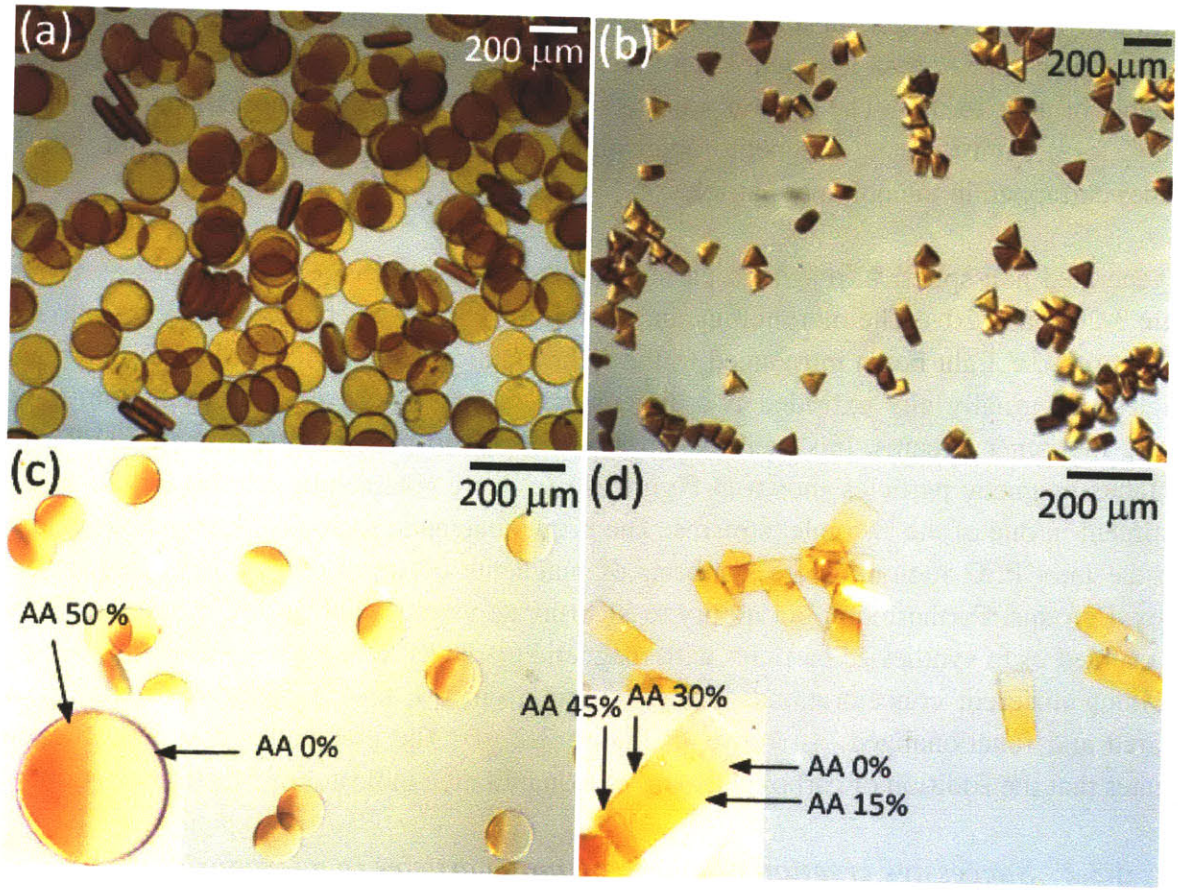

Figure 3-2: Optical images of various magnetic microparticles. (a) Homogenous magnetic disks. (b) Homogenous tranglular particles. (c) Janus disks (d) Gradient particles.

To create nanoparticles in the polymer gel matrices generated using SFL, the particles were suspended in a sodium hydroxide solution for the deprotonation of the COOH groups to COO^-. Electrostatic repulsion between these charged groups caused the PEG/PAA particle substrate to swell, increasing the osmotic pressure within the gel. Then, these anionic polymer particles were mixed with solutions of two iron ions. In order to create magnetite instead of other iron oxides that have low magnetizations, precise control of the Fe^{3+} /Fe^{2+} ratio was necessary. The Fe^{3+} ion is attracted to carboxyl ions more strongly than is Fe^{2+}, and thus, the bulk solution needed to contain more Fe^{2+} than Fe^{3+} to provide the optimal ratio within the particles. The optimal Fe^{3+}/Fe^{2+} ratio of 1:75 in the bulk was used to bring a ratio of Fe^{3+}/Fe^{2+} of 2 within the polymer particles needed to produce magnetite nanoparticles.[13] The polymeric particles were mixed in the iron solution for 30 mins during which the iron ions diffused into polymer particles and were

chelated with the carboxyl ions. With typical particle dimensions (L) of 15 μm and diffusivities of iron ions through the gel substrate (D) of 0.5 x10^{-9} m^2/s,[14] the diffusion time scale ($\tau = L^2/D \sim$ 1 s) was much shorter than the incubation time so that the ferric and ferrous ions penetrated the full depth of the particles. The pH was adjusted by adding NH_4OH and the temperature was held at 60°C for 15 mins during magnetite deposition. These processes create magnetite with bare surfaces entrapped in the polymer particles.

We generated non-spherical magnetic particles in the shapes of disks and triangles as shown in Figure 3-2 (a) and 2(b). The morphology and size of the particles were dictated by the mask used to shape the UV light beam introduced to the microfluidic channel during SFL. In this manner, particles of virtually any extruded two-dimensional shape can be created. With multiple co-flowing monomer streams, this method can also be used to generate multifunctional particles. The Janus magnetic particles shown in Figure 3-2 (c) were obtained by adding acrylic acid as a constituent in one of the two inlet streams. The brown magnetic region is clearly distinguishable from the inert PEG region, as the synthesis of magnetite occurred only in the presence of the carboxyl groups. Furthermore, our ability to incorporate various chemistries in one particle with SFL enabled us to synthesize particles with magnetic gradients. Using four inlets with monomers containing different concentrations of acrylic acid from 0% to 45%, gradient particles were prepared and functionalized, as shown in Figure 3-2 (d). The gradient in magnetic properties indicates that the addition of carboxyl groups is a quantitative indicator of functionalization.

3.3.2 Successive creation of magnetic nanoparticles in microparticles

Since magnetic functionalization is not perfectly efficient with respect to the active groups within the hydrogel, carboxyl groups remain in the particles after the magnetite nucleation and synthesis. These carboxyl groups can be used to strengthen the magnetic properties by repeating the nanoparticle synthesis procedure. The growth of nanoparticles, shown schematically in Figure 3-1, can be repeated several times successively to increase magnetic properties. Figure 3-3 contains optical images of microparticles subjected to several cycles of magnetic nanoparticle synthesis, in which the color of the particles becomes darker as the number of cycles increases and opaque particles are generated containing more magnetic nanoparticles.

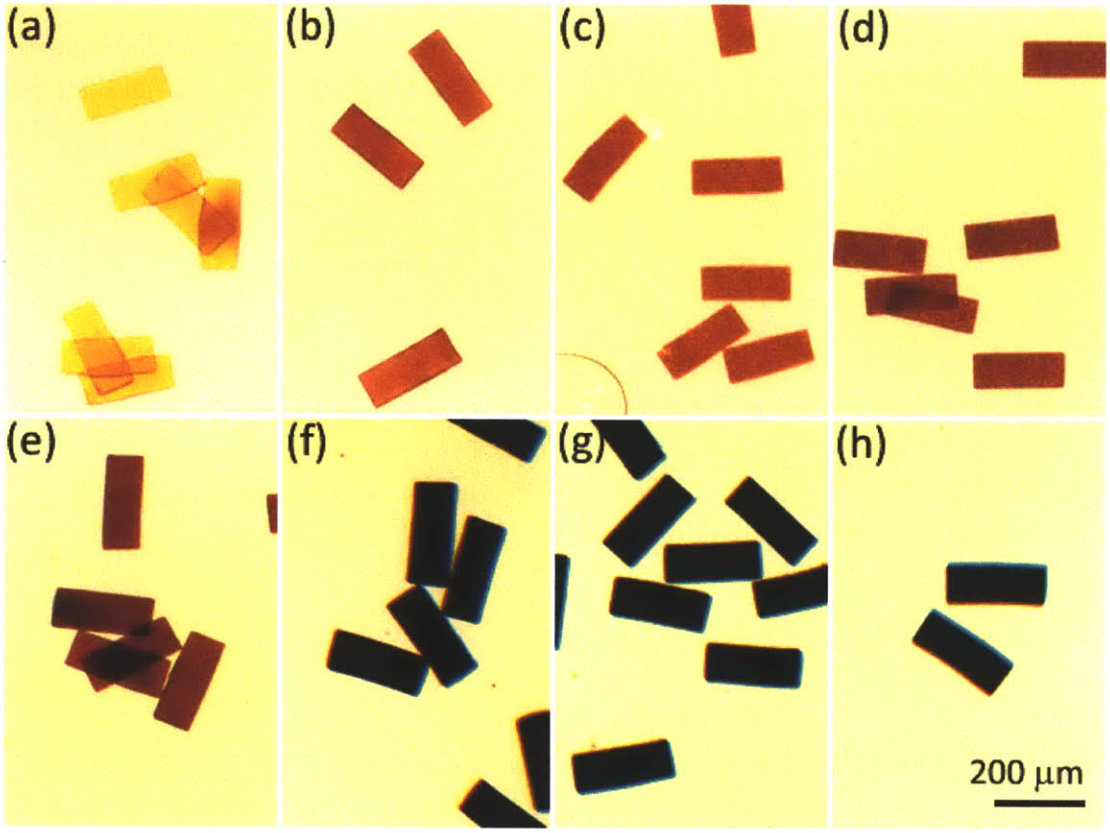

Figure 3-3: Successive synthesis of magnetite in micro polymer particles.

3.3.3 Magnetic properties

In order to determine the magnetic properties of the particles following each cycle, we obtained magnetization curves from SQUID measurements, as shown in Figure 3-4 (a). All magnetic particles exhibited superparamagnetism without remanence. The magnetization M of an assembly of monodisperse superparamagnetic nanoparticles of diameter d in the direction of an applied magnetic field H can be described by the Langevin function,

$$\frac{M}{\phi M_d} = \coth\alpha - \frac{1}{\alpha} \equiv L(\alpha) \qquad (3\text{-}1)$$

where ϕ is the solid volume fraction, M_d is the saturation magnetization of the bulk material based on volume, $\alpha = \pi\mu_0 M_d H d^3/6kT$, k is the Boltzmann constant, T is the temperature, and μ_0 is the permeability of free space.[15]

Nanoparticles synthesized by chemical co-precipitation are generally not monodisperse, however, and it is typically assumed that these magnetic nanoparticles follow a log-normal distribution in sizes,[16-17] with the probability density function given by

$$P(x) = \frac{1}{\sqrt{2\pi}\sigma x} e^{\frac{(\ln x - \mu)^2}{2\sigma^2}} \qquad (3\text{-}2)$$

where $x = D/D_p$ is the reduced diameter, μ is the mean of $ln\ x$, D_p is the median diameter, and σ is the standard deviation of the log-normal distribution.

The magnetization curve for a polydispersed collection of nanoparticles can be obtained by integrating the Langevin function over the particle size distribution to obtain

$$M(\alpha) = \frac{\pi}{6} M_d D_p^{\ 3} \int_0^\infty L(\alpha) x^3 P(x) dx \qquad (3\text{-}3)$$

Under high applied magnetic field strengths, this equation reduces to

$$M = \phi M_d \left(1 - \left[\frac{6}{\pi} \frac{kT}{\mu_0 M_d D_p^3} \int_0^\infty x^{-3} P(x) dx \right] \frac{1}{H} \right) \qquad (3\text{-}4)$$

The saturation magnetization of the nanoparticles, $M_s = \phi M_d$, was obtained from the intercept of the M versus inverse H plot of the data at large values of H. Assuming that we created mostly magnetite, instead of other oxides, we used M_d = 92 emu/g.[18] As was expected, the saturation magnetization of micro particles (Figure 3-4 (b)) increased with increasing number of cycles without loss of nanoparticles during the deprotonation of the carboxyl groups with NaOH. The saturation magnetization reached 42 emu/g after eight cycles. This value is on the high end for typical commercially available magnetic beads, which have saturation magnetizations in the range of 20 – 40 emu/g.

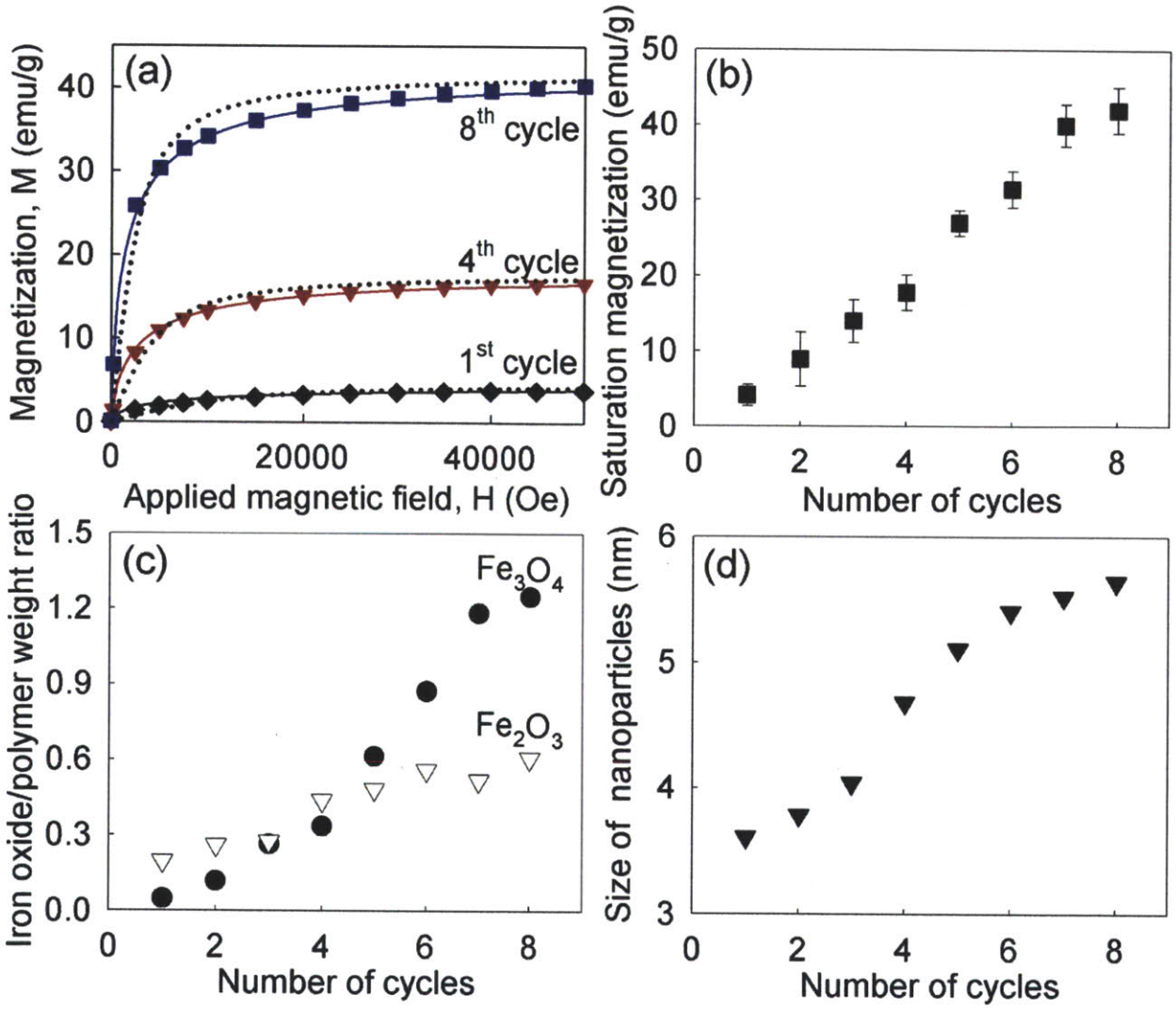

Figure 3-4: Magnetic properties of magnetic micro particles and nanoparticles. (a) Magnetization curves. The points were obtained from SQUID measurement, while solid lines were calculated using Chantrell's method shown in equation (6). The dotted line was obtained from the Langevin function assuming that particles were monodisperse. (b) Saturation magnetization values of polymer/nanoparticle complexes. (c) Magnetic nanoparticle content excluding the polymer matrix calculated using results panel (b) and TGA analysis. The ratios $x_{Fe3O4}/x_{PEG/PAA}$ and $x_{Fe2O3}/x_{PEG/PAA}$ are plotted. (d) Nanoparticle sizes calculated using Chantrell's method.

3.3.4 Size distribution of magnetic nanoparticles

The magnetization curves also yielded the average diameter and size distribution of the magnetic nanoparticles. Chantrell et al. reported that the median diameter (D_p) and standard deviation (σ) of the magnetic nanoparticles distributed according to the log-normal distribution can be obtained from the magnetization curves using[16]

$$D_p = \left(\frac{18kT}{\pi M_d} \left[\frac{\chi_i}{3\phi M_d H'} \right]^{1/2} \right)^{1/3} \tag{3-5}$$

$$\sigma = \frac{1}{3} \left(\ln \left(\frac{3\chi_i H'}{\phi M_d} \right) \right)^{1/2} \tag{3-6}$$

where χ_i is the initial magnetic susceptibility and H' is obtained from the $M = 0$ intercept of a graph of M versus $1/H$ at high applied field. Diameters of nanoparticles calculated in this manner are shown in Figure 3-4 (d) as a function of repetition cycle number. As can be seen, particle size increased with successive nanoparticle synthesis cycle as we loaded more magnetite into the polymer particles. Magnetite can be grown either on the surfaces of existing nanoparticles or at un-occupied carboxyl groups to form new nucleation points. Nanoparticle diameter did not increase as significantly at low cycle numbers as it did at later cycles, leading to the conclusion that at low cycle numbers, the nucleation of new nanoparticles at un-occupied carboxyl sites is the dominant form of magnetite incorporation. We note that the diameter of nanoparticles reached approximately 5.7 nm. The nanoparticle size cannot exceed the mesh size in polymer particles, since the mesh exerts physical constraints on nanoparticle growth. Hence, the maximum particle size is close to the mesh size of swollen polymer particles. The σ of nanoparticles varied from 0.32 to 0.43, increasing with the synthesis repetition cycle number. The higher values of σ at higher cycles imply that successive synthesis produced a wider range of particle sizes owing to both nucleation and growth occurring during the nanoparticle synthesis process. We believe that the range of polydispersity is acceptable, as co-precipitation is notorious for imprecise size control.

We performed TEM analysis to further characterize the magnetic nanoparticles within the hydrogel matrix of the microparticles. The microparticles were prepared as thin slices with a thickness of 40 nm using a Microtome. As shown in Figure 3-5, the nanoparticles grown within the polymeric particles were distributed uniformly indicating that the carboxyl groups effectively attracted iron ions from the bulk into polymer particles. Figure 3-5 (a) and (b) show the effect of successive synthesis of magnetite, with respect to both nucleation and growth, on the sizes

loading of the nanoparticles. Consistent with our expectation that we would load more magnetite with each successive co-precipitation, Figure 3-5 (b) with four cycles (4.98 nm) has larger particle sizes than Figure 3-5 (a) with one cycle (3.63 nm). In addition since both samples have the same thickness, the image from the fourth cycle, showing a darker appearance, indicates that more magnetite was incorporated into the polymer gels.

One can observe that the diameters of nanoparticles shown in Figure 3-5 are larger than those in Figure 3-4. This can be explained by investigating Chantrell's method for calculation particle size. The saturation magnetization value used in this calculation is that of bulk magnetite. However, as magnetic nanoparticles usually have a magnetite core and thin shell (0.8 nm) of nonmagnetic material, the responding magnetization would be smaller than nanoparticles composed of magnetite only[7]. Therefore, equation (3-5) underestimates the size of nanoparticles.

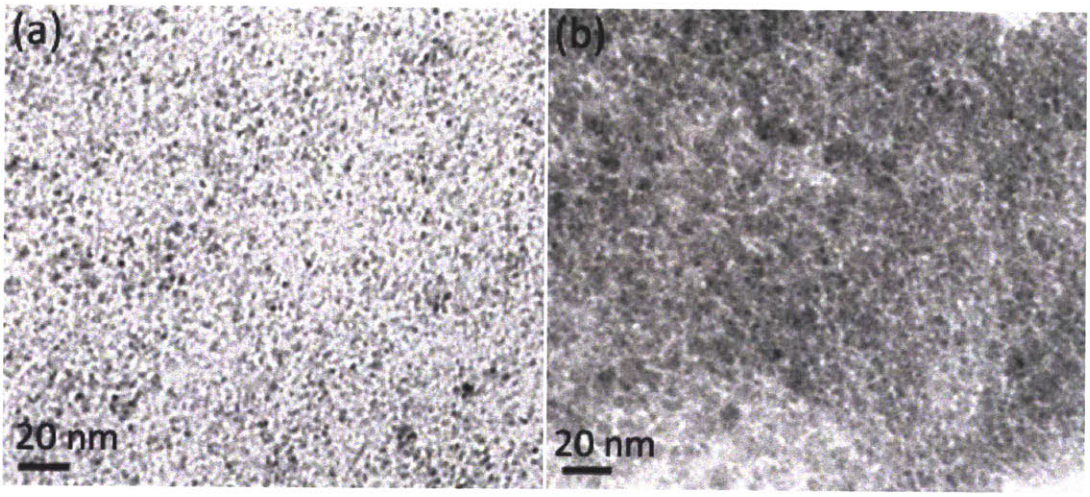

Figure 3-5: Cross-sectional TEM images of magnetite/polymer matrix. Magnetic nanoparticles in polymeric particles after (a) the first cycle and (b) the fourth cycle.

3.3.5 Contents of iron oxide

By exploring the saturation magnetization of particles and the weight content of total iron oxide, we can estimate the amount of magnetite (Fe_3O_4) and anti-ferromagnetic iron oxide (α-Fe_2O_3) in the polymeric particles. The TGA results provide the weight fraction of the PEG and PAA polymers comprising the particle, as polymers burn at high temperature (~600 °C). The material balance equations,

$$x_{\text{PEG/PAA}} + x_{Fe_3O_4} + x_{\alpha\text{-}Fe_2O_3} = 1 \quad (3\text{-}7)$$

$$\mathbf{M_d} x_{Fe_3O_4} = \mathbf{M_s} \quad (3\text{-}8)$$

where x is the weigh fraction of each component, can be used to determine the magnetite fraction in the particles. The calculated results are shown in Figure 3-4 (c). Microparticles contained more Fe_2O_3 than Fe_3O_4 after the first and second synthesis of nanoparticles, but the weight percent of Fe_3O_4 exceeds Fe_2O_3 beyond the fourth synthesis. Although the preferential synthesis of Fe_2O_3 in initial synthesis cycles was unexpected, it can be explained by investigation of our synthesis process. Before we increase the pH to precipitate magnetite, we do not wash out the excess iron ions in solution. As the diffusion timescale is short in our porous particles, washing steps rapidly extract the iron ions chelated in polymer particles. Therefore, we choose simply to remove the excess iron solution rather than wash the particles in fresh buffers. However, this leads to the creation of undesired iron oxides, as the bulk iron solution has the ratio of Fe^{2+} : Fe^{3+} = 75:1. With NH_4OH, non-magnetic iron oxides can be produced both in the bulk solution and on the surfaces of polymeric particles, where the ratio of irons is similar to the bulk, as shown schematically in Figure 7. The α-Fe_2O_3, known to be made of Fe^{2+} in high pH can be attached to the surface of polymer particles. The color of the solution, which has a light red hue, supports the formation of α-Fe_2O_3.[19]

The SEM images in Figure 3-6 indicate that the surfaces of microparticles after magnetic functionalization are not as smooth as those of the parent polymeric particles, but are coated with micron-size clusters. Comparison of the TEM images in Figure 3-5 and the SEM images in Figure 3-6 indicates that the clusters on the particle surface are different in size and shape than those formed within the microparticle. In addition, iron oxides are cation absorbents, and thus iron ions can be attracted to microparticles even though most of the carboxyl groups are occupied with magnetite previously synthesized.

The rapid increase of Fe_3O_4 content with synthesis cycle repetition, as shown in Figure 3-4 (c), can be caused by the larger quantity of iron oxide present in polymeric particles with each subsequent growth. However, there is again a physical constraint on the growth of magnetic nanoparticles with the limited mesh size in the polymer particles. Interestingly, the shapes of the curves for Fe_3O_4 in Figure 3-4 (c) and (d) are similar, indicating that more cations can be absorbed with larger nanoparticle size, but that a finite limit on size can be achieved due to mesh size limitations. In contrast to the trend seen for Fe_3O_4, the Fe_2O_3 content does not increase significantly after the first few synthesis cycles. Since Fe_2O_3 would be associated with the surfaces of the polymer particles, addition of Fe_2O_3 to the polymer particles would occur in the early cycles only as the surface quickly became saturated. Also, Fe_2O_3 on polymer particles will be detached when Fe_2O_3 particles are too large to adhere to the surfaces of the hydrogel particles during the washing cycle.

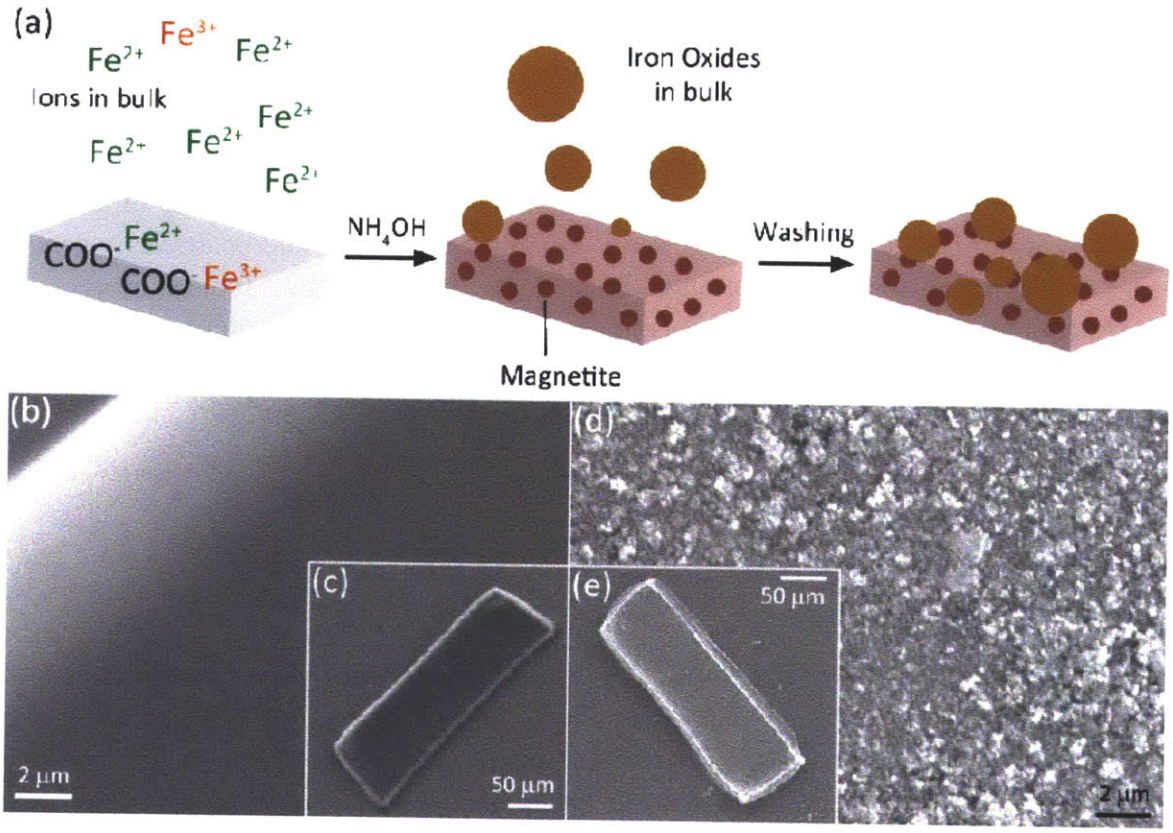

Figure 3-6: The mechanism of the synthesis. (a) Schematics to explain the synthesis mechanism. The ratio between Fe^{2+} and Fe^{3+} ions in bulk is different from that in the polymer matrix. (b) SEM image of PAA/PEG particles. (c) The particle in (b) imaged at low magnification. (d) PAA/PEG/Iron oxide particle surfaces. (e) The particle in (d) imaged at low magnification.

We can also account for the high loading of Fe_2O_3 in lower cycles as thin layers grown over a core of Fe_3O_4. If the shell thickness in 3 nm particles is the same as that in 5nm particles, the thin shells make up a larger volume percentage of the smaller than the larger particles. In other words, Fe_2O_3 is more abundant with smaller particles in low cycle numbers. In addition, the apparent Fe_2O_3 reflects the disordered layer at the nanoparticle surface, which becomes ordered as the new layers are added.

An alternate approach to making magnetic particles via microfluidic channels is to incorporate commercial magnetic beads (20 – 40 emu/g) in the monomer mix during synthesis.[6,9-10] As this method does not require post-synthesis functionalization, one might assume that it would be a

faster and simpler means to generate magnetic particles. However, the final magnetization of the polymeric particles prepared by this method will be considerably lower than that of the magnetic beads owing to the extra mass added by the polymeric substrate. For photo-polymerization, the presence of these opaque magnetic beads also makes polymerization challenging due to attenuation and limited penetration of the light into the reaction mixture because of absorbance by the beads. Hence, many reported superparamagnetic microparticles generated photochemically using direct-incorporation of magnetic materials have typical magnetization values of 5 emu/g or less due to limitations on magnetic loading. On the contrary, using our post-functionalization approach, we controlled not only the shape of particles but also the extent of functionalization, achieving saturation magnetizations of up to 42 emu/g, using successive growth.

3.4 Conclusion

In conclusion, we demonstrate the synthesis of non-spherical magnetic microparticles via stop-flow-lithography and *in-situ* magnetic nanoparticle synthesis. The method described here allows for the synthesis of multi-functional particles and highly magnetic particles depending on the number of successive nanoparticle synthesis cycles. We investigated the properties of the particles on both microscopic and nanoscopic scales, elucidating the mechanism of the synthesis process. The synthesis is straightforward and can be carried out under relatively low temperature and atmospheric pressure conditions using common chemicals. Also, this study can be adapted to the synthesis of other nanoparticles using co-precipitation, introducing the flexibility to create desired particle shapes with a great range of functionalities. Since particles have un-occupied carboxyl groups even after the first nanoparticle creation, this method can be use to add multiple functionalities, such as the addition of biomolecules, with subsequent reactions.

3.5 References

(1) Dreyfus, R.; Baudry, J.; Roper, M. L.; Fermigier, M.; Stone, H. A.; Bibette, J. *Nature* **2005**, *437*, 862.

(2) Ghosh, A.; Fischer, P. *Nano Lett* **2009**, *9*, 2243.

(3) Erb, R. M.; Son, H. S.; Samanta, B.; Rotello, V. M.; Yellen, B. B. *Nature* **2009**, *457*, 999.

(4) Zerrouki, D.; Baudry, J.; Pine, D.; Chaikin, P.; Bibette, J. *Nature* **2008**, *455*, 380.

(5) Smoukov, S. K.; Gangwal, S.; Marquez, M.; Velev, O. D. *Soft Matter* **2009**, *5*, 1285.

(6) Chen, C. H.; Abate, A. R.; Lee, D. Y.; Terentjev, E. M.; Weitz, D. A. *Adv Mater* **2009**, *21*, 3201.

(7) Lee, S. H.; Liddell, C. M. *Small* **2009**, *5*, 1957.

(8) Nunes, J.; Herlihy, K. P.; Mair, L.; Superfine, R.; DeSimone, J. M. *Nano Lett* **2010**, *10*, 1113.

(9) Bong, K. W.; Chapin, S. C.; Doyle, P. S. *Langmuir* **2010**, *26*, 8008.

(10) Kim, H.; Ge, J.; Kim, J.; Choi, S.; Lee, H.; Lee, H.; Park, W.; Yin, Y.; Kwon, S. *Nat Photonics* **2009**, *3*, 534.

(11) Yuet, K. P.; Hwang, D. K.; Haghgooie, R.; Doyle, P. S. *Langmuir* **2010**, *26*, 4281.

(12) Dendukuri, D.; Gu, S. S.; Pregibon, D. C.; Hatton, T. A.; Doyle, P. S. *Lab Chip* **2007**, *7*, 818.

(13) Huang, J. S.; Wan, S. R.; Guo, M.; Yan, H. S. *J Mater Chem* **2006**, *16*, 4535.

(14) Easteal, A. J.; Price, W. E.; Woolf, L. A. *J Phys Chem-Us* **1989**, *93*, 7517.

(15) Rosensweig, R. E. *Ferrohydrodynamics*; Cambridge University Press: Cambridge ; New York, 1985.

(16) Chantrell, R. W.; Popplewell, J.; Charles, S. W. *Ieee T Magn* **1978**, *14*, 975.

(17) Shen, L. F.; Laibinis, P. E.; Hatton, T. A. *Langmuir* **1999**, *15*, 447.

(18) Yamaura, M.; Camilo, R. L.; Sampaio, L. C.; Macedo, M. A.; Nakamura, M.; Toma, H. E. *J Magn Magn Mater* **2004**, *279*, 210.

(19) Cornell, R. M.; Schwertmann, U. *The iron oxides : structure, properties, reactions, occurrences, and uses*; 2nd, completely rev. and extended ed.; Wiley-VCH: Weinheim, 2003.

Chapter 4

Modeling and synthesis of opaque microparticles

4.1 Introduction

Hydrogels have become increasingly important in tissue engineering,[1] drug delivery,[2] and bioassays[3] due to their biocompatibility,[4] mechanical stability,[5] responsiveness to environmental cues,[6] controlled degradability,[7] and ease of functionalization.[8] Hydrogels in the form of particles, rather than a bulk substrate, are more attractive in certain applications as they have shorter length scales and can be easily manipulated. Hydrogel particles with spherical or sphere-like shapes can be synthesized using bulk emulsion polymerization[9] or two-phase microfluidic systems.[10-14] Recently, researchers have created various shapes of hydrogel particles using template molding.[15] Stop-flow lithography (SFL) enables photolithographic particle formation in a semi-continuous operation,[16-17] with various particle shapes and sizes,[18] and with multiple adjacent chemistries.[19] These hydrogel particles can have a variety of chemical functionalities depending on monomer selection and may also contain chemically and/or physically-entrapped materials,[20-24] which can enhance performance for certain applications.

Nanoparticles are also very important materials since they have large surface-to-volume ratios, can respond to external stimuli quickly, may exhibit interesting properties differing from those of bulk materials,[25] and can be distributed more homogeneously in desired systems than their larger counterparts. Because of these attributes, combinations of hydrogels and nanoparticles have been studied for many applications.[26-27] This combination is especially interesting when using hydrogel particles, which can add further functionalities with various shapes. Magnetic particles

have been used for many applications in imaging,[28] assembly,[29-33] separation[34-37] and applications requiring induced mechanical stress.[38-40] Efforts to include magnetic materials in hydrogel particles have been accomplished successfully using photolithography.[11,41-44] Multifunctional magnetic particles are particularly interesting as they assist in analyte detection by providing precise control over particles in solution,[42] color-coding of particles,[44] and controlled assembly of particles.[41]

Unfortunately, many of the materials to be embedded in hydrogel particles can inhibit photo-polymerization due to their absorbance of the UV light required for the photolysis reaction. We observe this phenomenon during particle synthesis with monomers containing magnetic materials or dyes. In order to better understand this process and develop more robust synthesis methods, we investigate here hydrogel particle synthesis with two opaque materials: magnetic beads and a UV absorbing dye. The latter is used as a model system.

Recently, we investigated the mechanism of the photo-polymerization reaction during particle synthesis in PDMS channels.[45] We found that during free-radical polymerization within a channel, oxygen diffuses through the PDMS thereby preventing polymerization near the PDMS surfaces. This leaves a lubricating layer of unpolymerized monomer, allowing the particles to flow out of the microfluidic channel easily. Starting from our previous model, we define a dimensionless parameter pertaining to UV absorbance which accounts for the inclusion of opaque materials in the monomer mix. We also study magnetic particle synthesis with and without an applied uniform magnetic field. Observing and understanding the effects of encapsulated opaque materials on hydrogel particle height and degree of cross-linking can provide valuable insight for the rational design of new particles with higher degrees of geometric and chemical complexity. The material in this chapter was reproduced from Suh, Bong, Hatton, and Doyle, *Langmuir*, 2011.[46]

4.2 Experimental methods

4.2.1 Materials

Polymeric particles are made from poly(ethylene glycol) (700) diacrylate (PEG-DA 700, Sigma-Aldrich), 2-hydroxy-2-methylpropiophenon (Darocur 1173, Sigma-Aldrich) initiator. We used 100 nm diameter carboxylate-modified magnetic bead solutions (Ademtech) or Allura Red AC (Sigma-Aldrich) solutions as opaque materials. Tween-20 (Sigma Aldrich) was used at 0.05% to prevent particles loss due to sticking on pipette tips or tubes. To easily observe particle heights, particles were redispersed in 30 % (v/v) poly(ethylene glycol) (200) (PEG 200, Sigma-Aldrich) in water.

4.2.2 *Microfluidic devices*

Microfluidic channels for SFL were fabricated using standard soft-lithography techniques. Polydimethyl-siloxane (PDMS, Sylgard 184, Dow Corning) in a 10:1 base-to-curing agent ratio was molded on a patterned silicon wafer (SU-8 photoresist, Microchem), then cured in an oven at 65 °C for 2 hours. Holes for connections to the inlet and outlet were punched with an 18 gauge luer stub adapter. Glass slides were coated with PDMS and partially cured at 65 °C for 22 min. The clean patterned PDMS was assembled with the PDMS coated glasses and then placed in the oven for 45 min. The prepared microfluidic channel was connected with inlets that were made by pipette tips (ART 10 Reach and ART 200, Molecular BioProducts, Inc) and outlet aluminum tubing (1/16", K&S) for collecting particles after synthesis. For particle synthesis, the devices were mounted on the inverted microscope (Axiovert 200, Zeiss).

4.2.3 *Stop-Flow-Lithography setup*

We create hydrogel particles in microfluidic devices when flow is stopped. Formed particles are then moved out of the polymerization area via the inflow of fresh monomer solutions. Pulsed flow was operated automatically for the generation of stop-polymerization-flow cycles, alternating the pressure at all four inlets simultaneously from 0 psi to 3 psi. The relative width of the inlet streams was controlled by a pressure valve (ControlAir, Inc) and a digital pressure gauge (DPG 100G, Omega Engineering, Inc.). The UV source of Lumen 200 (Prior Scientific, 100% setting) initiated polymerization reactions. Photomasks were placed in the field-top of the microscope. The desired excitation spectrum was selected using a UV filter (11000v2, Chroma). UV intensity with the 20× objective of an inverted microscope (Axiovert 200, Zeiss) was 3400 mW/cm^2, as measured by a UV power meter (Accu-Cal 30, Dymax). All images were taken with a digital SLR camera (D200, Nikon).

4.2.4 *Particle synthesis*

Figure 4-2 shows our synthesis procedure. The pre-polymer solutions consisted of 5% (v/v) solutions of Darocur 1173, 30% (v/v) PEG-DA 700 and 65% (v/v) opaque material solutions. The concentration of the opaque material solution was adjusted to ensure the desired final concentration of this material in the synthesized hydrogel particles. We generated particles with four distinct chemistries using a microfluidic synthesis device with four inlets. Different concentrations of opaque materials were incorporated in the different regions (Figure 1(a)); inlet solutions contained 0, 25, 50, and 75 mg/ml of magnetic beads in pre-polymer solutions, or 0, 9, 18, and 27 mg/ml of UV absorbing dye. In Allura Red AC pre-polymer solutions, 0.01 wt% of methacryloxyethyl thiocarbamoyl rhodamine B (Polysciences, Inc.) was added. After the

synthesis, un-reacted monomer solution was removed by rinsing particles with Tween 20 solutions.

4.2.5 UV Absorbance measurement

UV absorption measurements were performed with a UV-vis spectrometer (HP 8453, Hewlett-Packard). To measure highly concentrated solutions, we used quartz cuvettes with 0.1 mm path length (Starna Cells, Inc). Each sample was measured 5 times, and 5 samples were taken for each concentration. The UV absorbance at 365 nm (wavelength used for polymerization) was recorded.

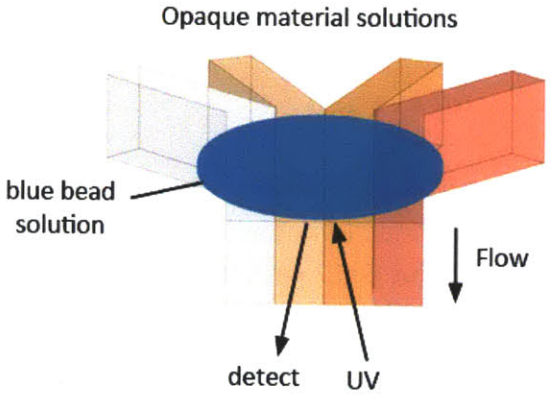

Figure 4-1: Schematic diagram of a microfluidic channel for measurements of relative UV absorbance.

Since some of the magnetite solutions used in this study were too concentrated to be observed with a UV-vis spectrometer (with a quartz cuvette with a 0.1 mm path-length), we measured the relative UV absorbance of these materials in a microfluidic channel. As illustrated in Figure 4-1, four solutions with varying concentrations of magnetite were flown through a microfluidic channel. The ceiling of the channel was coated with blue beads, which have an excitation wavelength of 360 nm and emission wavelength of 407 nm, and can be used to estimate the amount of UV penetrating the solutions. The UV projected from the objective passes through the monomer solutions to excite the blue bead-coated substrate and the emission from the beads travels back through the sample where it is then captured by objective for detection. Although this experiment was designed to study the absorption of the UV light (360 nm), some of the emitted blue visible light would also be absorbed by the opaque materials in the solutions, which would affect detection. However, the absorptivity of magnetite at 360 nm is three times larger than that at the emission wavelength, 407 nm.[47] Also, it is possible that the relative absorbance

between the four magnetite-containing monomer solutions at 407 nm is similar to the relative absorbance in 360 nm; therefore, our investigation of the relative absorbance at 360 nm is reasonable enough.

4.2.6 Particle Height Measurement

Bright field was used to image magnetic particles, while particles synthesized with the UV absorbing dye were observed with fluorescence microscopy. Particle heights were measured using Image J software. Straight lines were drawn throughout particle height cross-sections, and pixel intensity was plotted as a function of distance along the lines. The edges of the particles were well-defined for magnetic particles. For particles created with the dye, we measured fluorescence intensity, defining particle heights when the fluorescent signal is three times higher than noise (signal-to-noise = 3).

4.2.7 Magnetic characterization

Uniform magnetic fields were generated using a custom-made electromagnet with a DC power supply (GPS-2303, GW Instek). The induced magnetic field strength was measured with a gauss meter (SYPRIS).

4.3 Model Description

4.3.1 Governing equations

Table 4-1: Simplified reaction mechanism in our model

Reactions	Mechanism step
$PI \xrightarrow{h\nu} \dot{R}$	Photolysis
$\dot{R} + M \rightarrow R\dot{M}$	Chain initiation
$R\dot{M}_n + M \xrightarrow{k_p} R\dot{M}_{n+1}$	Chain propagation
$R\dot{M}_n + R\dot{M}_m \xrightarrow{k_t} RM_nM_m$	Chain termination
$R\dot{M}_n + O_2 \xrightarrow{k_o} RM_nOO$	Inhibition

We developed a one-dimensional model to describe particle synthesis in flow lithography, including photolysis, chain initiation, chain propagation, chain termination, and inhibition in the reaction mechanism as listed in Table 4-1. We build off our prior modeling efforts which did not consider UV absorbance.[45]

We based this model on our previous work, modifying it to allow also for the effect of the UV absorbing materials. Figure 4-2 (b) shows the channel geometry, illustrating UV absorption caused by both photoinitiator and magnetic beads. The light intensity *I(z)* can be expressed by the following equation, assuming that the two materials absorb UV light independently.

$$\frac{\partial I(z)}{\partial z} = -\left(\varepsilon_1[\mathrm{PI}] + \varepsilon_2[\mathrm{OM}]\right) I(z) \tag{4-1}$$

$$I(z) = I_0 \exp\left(-\left(\varepsilon_1[\mathrm{PI}] + \varepsilon_2[\mathrm{OM}]\right) z\right) \tag{4-2}$$

The ε_1 and ε_2 are the extinction coefficient of photoinitiator at the wavelength of 365 nm and magnetic beads or dye, respectively. The [PI] and [OM] represent concentrations of photoinitiator and magnetic beads or dye. I_0 is the UV intensity at $z = 0$. Since the rate of radical production, r_a, within dz is proportional to the volumetric UV absorption rate by the photoinitiator,

$$r_a = -\varphi \frac{\varepsilon_1[\mathrm{PI}]}{\varepsilon_1[\mathrm{PI}] + \varepsilon_2[\mathrm{OM}]} \frac{\partial I(z)}{\partial z} \tag{4-3}$$

$$r_a = \varphi I_0 \varepsilon_1[\mathrm{PI}] \exp\left(-\left(\varepsilon_1[\mathrm{PI}] + \varepsilon_2[\mathrm{OM}]\right) z\right) \tag{4-4}$$

where φ is the quantum yield of formation of initiating radicals. All the radicals listed in Table 1 were lumped into one term X in our model. The radical consumption rate, r_c, can be expressed as the summation of chain propagation and termination rates. The $[O_2]$ is the oxygen concentration.

$$r_c = k_t[\dot{\mathrm{X}}]^2 + k_o[\dot{\mathrm{X}}][\mathrm{O}_2] \tag{4-5}$$

Using the quasi-steady-state approximation, $r_a = r_c$, we derived the expression,

$$[\dot{\mathrm{X}}] = \frac{-k_O[\mathrm{O}_2] + \sqrt{\left(k_O[\mathrm{O}_2]\right)^2 + 4 r_a k_t}}{2k_t} \tag{4-6}$$

where k_o and k_t are the rate constant for chain termination, and oxygen inhibition, respectively. The concentration of monomer, [M], and [O_2] are expressed below as functions of z and time, t, using the mass transport equation. Diffusion of monomers was not considered here as they are relatively large compared to oxygen.

$$\frac{\partial[O_2]}{\partial t} = D_O \frac{\partial^2[O_2]}{\partial z^2} - k_O[O_2][\dot{X}] \tag{4-7}$$

$$\frac{\partial[M]}{\partial t} = -k_p[M][\dot{X}] \tag{4-8}$$

Non-dimensionalizing equations (7) and (8) using

$$\tau = tD_O / H^2,\ \theta = [O_2]/[O_{2,eqb}],\ \eta = z/H,\ \xi = [M]/[M_0]$$

$$Da_1 = \frac{k_O{}^2 H^2 [O_{2,eqb}]}{2k_t D_O},\ Da_2 = \frac{k_p k_O [O_{2,eqb}] H^2}{2k_t D_O}$$

$$\alpha = \frac{4\varphi\varepsilon[PI]I_0 k_t}{k_O{}^2[O_{2,eqb}]^2},\ \beta = (\varepsilon_1[PI] + \varepsilon_2[OM])H$$

we obtain the equations

$$\frac{\partial\theta}{\partial\tau} = \frac{\partial^2\theta}{\partial\eta^2} - Da_1\theta\left(-\theta + \sqrt{\theta^2 + \alpha\exp(-\beta\eta)}\right) \tag{4-9}$$

$$\frac{\partial\xi}{\partial\tau} = Da_2\xi\left(-\theta + \sqrt{\theta^2 + \alpha\exp(-\beta\eta)}\right) \tag{4-10}$$

where [$O_{2,eqb}$] is the equilibrium oxygen concentration, [M_0] is the initial oligomer concentration, D_O is the diffusivity of oxygen in oligomer solutions, k_p is the rate constant for chain propagation, and H is the channel height. The dimensionless parameter β includes the effects of additional UV absorbing materials present during synthesis. Using the parameter values listed in Table 2, the resulting values of the dimensionless groups Da_1, Da_2 and α, are 6×10^8, 3×10^4, and 6×10^{-7}, respectively.

4.3.2 *Boundary and Initial Conditions*

The initial and boundary conditions are following.

$$\theta(0,\tau)=1 \quad \theta(1,\tau)=1 \quad \theta(\eta,0)=1 \quad \xi(\eta,0)=1$$

4.3.3 *Numerical solution*

To solve the equations, we used the method of lines with MATLAB solver ode15s, discretizing equations (4-9) and (4-10) in the η direction. The simulations were run with 400 uniform mesh elements in the η-direction, and maximum dimensionless time step of 10^{-6}.

Table 4-2: Parameters used in this paper

Parameters	Value	Unit	Reference
k_p	25	m^3/mol s	48
k_t	2520	m^3/mol s	48
k_o	5×10^5	m^3/mol s	49
H	30	μm	Measured
I_0	3400	mW/cm^2	Measured
[PI]	329	mol/m^3	Measured
ε_I	1.6	m^3/mol m	50
$[O_{2,eqb}]$	1.5	mol/m^3	51
φ	0.6	unitless	50

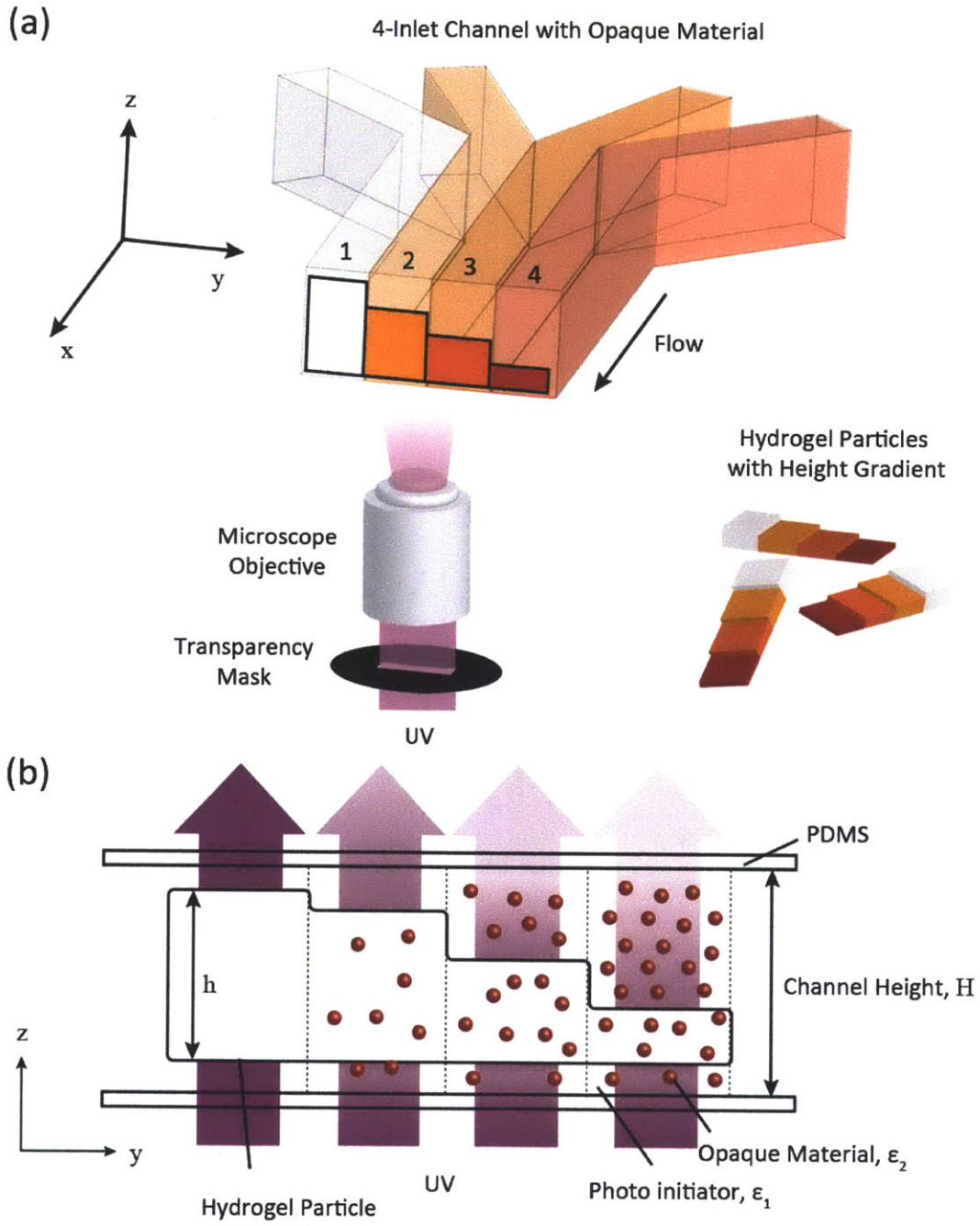

Figure 4-2: Schematic diagram of a microfluidic channel for stop-flow lithography in the presence of opaque materials.

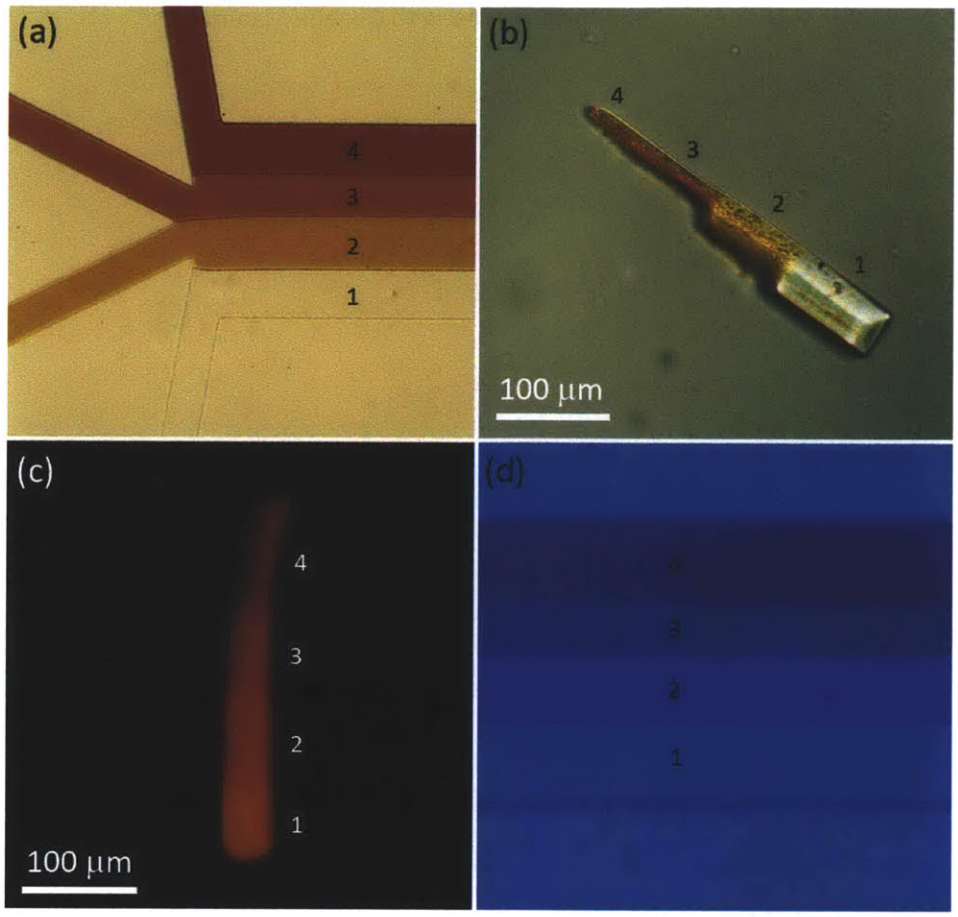

Figure 4-3: (a) Bright-field image of a 4-inlet microfluidic channel having 0, 25, 50 and 75 mg/ml magnetic bead monomer solutions. (b) Side-view of a particle synthesized in the channel depicted in (a). (c) Fluorescent side-view image of a particle created with a UV absorbing dye (Allura Red AC), where the pre-polymer solutions contained 0, 9, 18, 27 mg/ml of dye labeled 1, 2, 3, 4 on the particle respectively. (d) Fluorescent beads with an excitation wavelength of 360 nm and an emission wavelength of 407 nm were spread on the top of channel. The UV projected from the objective passes through the monomer solutions to excite the blue bead-coated substrate and the emission from the beads travels back through the sample where it is then captured by the objective for detection. The light intensity from the fluorescent beads depends on the concentration of magnetic beads in the channel.

4.4 Results and discussion

4.4.1 Synthesis of opaque particles

To study the effect of loading on polymerization, we introduced four monomer solutions with different magnetic particle concentrations as separate streams in parallel co-flow to the microfluidics channel, as shown in Figure 4-2 (a) and Figure 4-3 (a). Upon irradiation, the regions with higher concentrations of magnetic beads absorbed UV light more strongly than did those with lower bead concentrations, and therefore had the lowest UV intensities at the top of the channel, where $z = H$ (Figure 4-2 (b)). This UV intensity variation across the channel can be seen in Figure 4-3 (d) as a variation in the strength of the fluorescence emission from fluorescent blue beads spread on the top of the channel and excited at their excitation wavelength of 360 nm. The color changes across the channel correspond to the changes in UV penetration through each region of the monomer stream. The hydrogel particles formed under these conditions were stepped in height, reflecting the variations in transmitted UV illumination and in free radical generation required to initiate the polymerization reaction. Fewer radicals initiate fewer polymeriation reactions, and lead to regions where the conversion is less than the gel point and the weakly cross-linked polymers are then washed away during the particle recovery processes. As shown in Figure 4-3 (b), the synthesized magnetic particles showed a stepped height and color profile, since a different concentration of magnetic beads was incorporated in each region of the particles.

Likewise, we studied particles generated in the presence of a UV absorbing dye, again using four flow regions, but with different dye concentrations rather than magnetic beads. In Figure 4-3 (c), we observe variations in both the heights and fluorescence intensities along the particle, demonstrating that a height gradient can also result from particle synthesis with monomers containing materials other than UV absorbing beads. Importantly, these UV absorbing dyes need not be incorporated permanently in the resulting particles, since they can be washed out after synthesis. Therefore, one can use UV absorbing dye solutions as in-situ flow masks.[52]

4.4.2 Modeling result with various value of β

To understand better this phenomenon, we implemented our model described above. Simulation results for monomer conversion ξ as a function of position η in the synthesis channel are shown in Figure 4-4 for different values of the parameter β, an effective UV absorption coefficient accounting for both the photoinitiator and the UV absorbing materials. At $\xi = 0.98$, taken to be the critical conversion factor at which the gel first begins to form,[53] the particle height decreases as β increases, and the position at which gelation first occurs is the same regardless of β. These results are consistent with the experimental observations; particles synthesized with the magnetic

beads have a flat surface at the bottom and a stair-like profile on the far side of the light source (Figure 4-3 (b)), rather than the symmetric tapered shape about the x-y plane usually observed in the absence of absorbing additives. The fluorescent image for particles synthesized with the dye (Figure 4-3 (c)), on the other hand, do not have readily distinguishable boundaries in bright-field image, which can also be explained with our model. As β increases, the slope ($d\xi/d\eta$) near $\eta = 1$ decreases. Since there is a relatively wide region where $\xi = 0.98$, it is difficult to visualize distinct boundaries in the polymer matrix. However, the fluorescent signal from the incorporated rhodamine enables us to observe the boundary more readily. It should also be noted that monomer conversion along the direction η is not constant, creating a non-uniform polymer matrix. This ability to create particles with a monomer conversion gradient in the z-direction provides a means to control the third dimension of particle morphology during synthesis: particle shape and chemistry can be dictated in the x and y directions by varying inlet flows and transparency mask shapes, while UV absorbing dyes can be used to control height and monomer conversion in the z-direction.

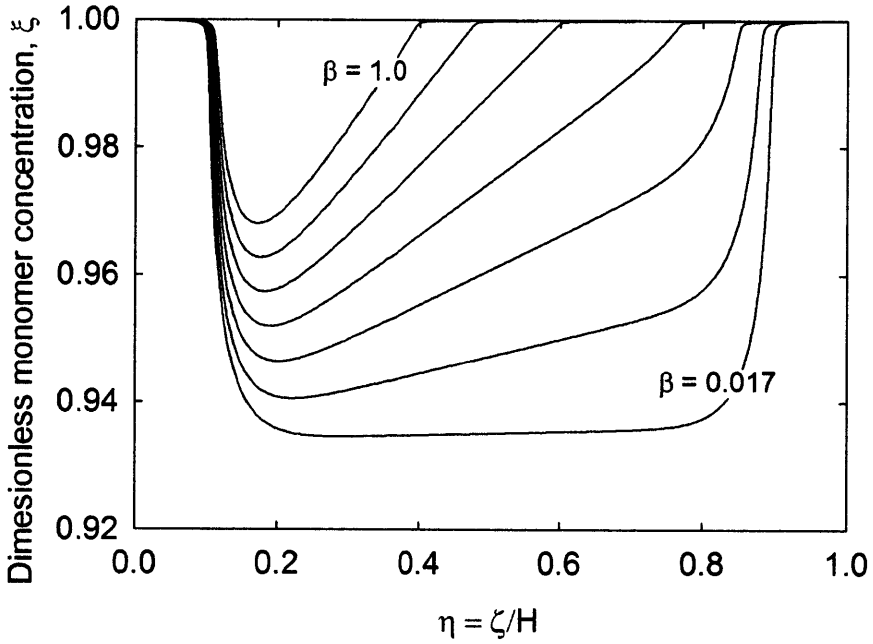

Figure 4-4: Uncross-linked monomer concentration (ξ) profile between the bottom ($\eta = 0$) and the top ($\eta = 1$) of the channel for various values of β (0.017, 0.17, 0.34, 0.51, 0.68, 0.85, 1.0). These results were obtained numerically by solving equations (9) and (10).

4.4.3 Comparison of experimental data and modeling results

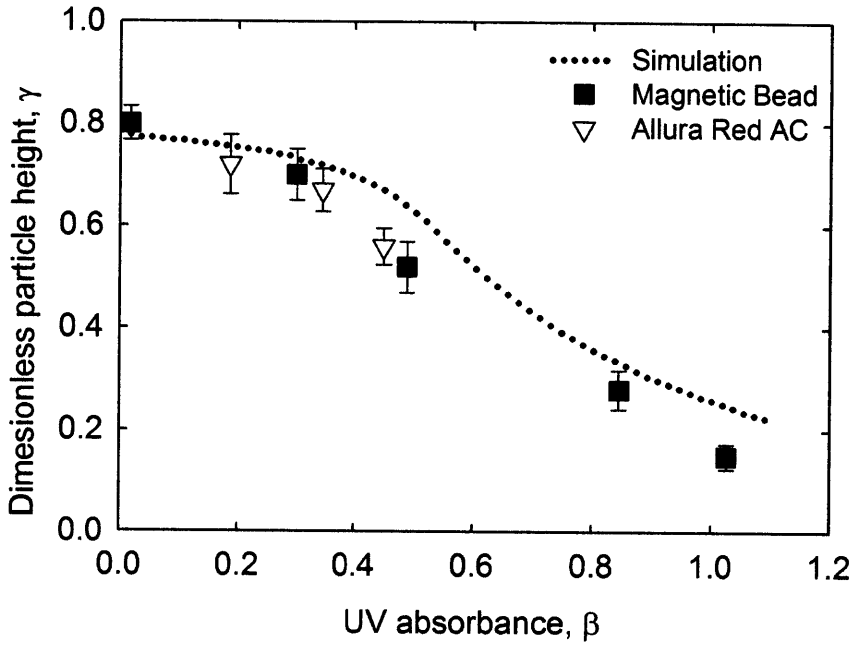

Figure 4-5: Comparison of experimental data and modeling results. Dimensionless particle height γ (scaled by channel height) versus UV absorbance β. Dotted line is from simulations. Solid squares and open triangles are from experiments using magnetic beads and UV absorbing dye, respectively.

Figure 4-5 compares the normalized particle heights obtained experimentally with the simulation predictions as a function of β. The simulation heights were estimated by selecting the region $\xi <$ 0.98 to be the cross-linked particle network, while the particle heights were determined experimentally using the software Image J. The measured particle heights are provided in Table 4-3. In general, particles synthesized in the presence of the UV absorbing dye had difficult-to-distinguish boundaries, as discussed above, and hence particle heights for these particles were delineated by fluorescence intensity measurements in which particle regions were defined by a fluorescent signal-to-noise ratio greater three. UV-vis spectrometry was employed to measure the UV absorbances of the magnetic beads and the UV absorbing dye; dilute conditions, 25 mg/ml for the magnetic bead suspension and 9 mg/ml for the dye solution, with a path length of 0.1 mm, were used in these measurements. The absorbance at higher concentrations was obtained by extrapolating from the low-concentration measurements. The relative UV absorbances of various concentrations are shown in Figure 4-6. While the comparison between experimental and predicted results is good over the whole range of β-values studied, the

experimental results for particles with relatively low β are in particularly good agreement with the simulation predictions. The success of our model-based height predictions suggests that we can estimate the particle heights that would be obtained with any given magnetic bead or dye concentration. With magnetic particles, in particular, where the loading of magnetic beads determines the particle magnetic response characteristics, it is important to be able to optimize the tradeoff between increased magnetic bead concentration and the decreased particle height, since their product determines the total magnetic response of the particle. In our case, a concentration of 50 mg/ml leads to the maximum total magnetic bead loading in the particles. Another consideration in the selection of the initial magnetic bead concentration is that the decreased height that results in regions with high magnetic loading can lead to mechanical instability in the particle architecture. Similar arguments hold for the particles based on UV absorbing dyes which can be designed to provide suitable optical characteristics. The model developed here provides important criteria for the design of particles with desired magnetic or optical properties.

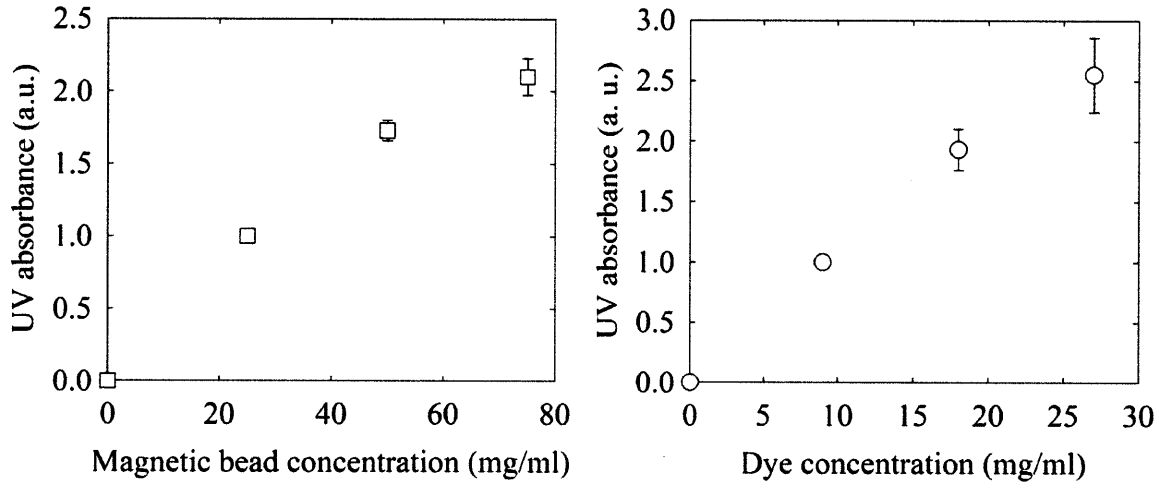

Figure 4-6: The relative, background-subtracted UV absorbance for the magnetite and opaque dye solutions tested.

Table 4-3: Measured particle heights

Material	Variables	1	2	3	4
Magnetic beads	Concentration (mg/ml)	0	25	50	75
	Height (μm)	24.0	15.6	8.4	4.5
UV Absorbing dye	Concentration (mg/ml)	0	9	18	27
	Height (μm)	24.0	21.6	20.1	16.8

In addition to providing predictions on the effects of absorbing materials on the morphologies of particles prepared by SFL, the model developed here can also provide insights into the cross-linking densities in the polymer network. Experimentally-determined fluorescence intensity profiles across each of the four sections of the particle shown in Figure 4-3 (c), corresponding to the four different UV absorbing dye concentrations used, are plotted using solid lines. Simulation results using the β-values appropriate for each of the UV dye concentrations in our experiments are shown in broken lines for comparison with the experimentally-derived profiles. The agreement is good, although the fluorescent signal profiles do not exhibit edges as sharp as those in the simulations near $\eta = 0.1$ and 0.9, but they are consistent with the simulations in terms of relative intensities and internal slopes over the internal position range $0.3 < \eta < 0.7$.

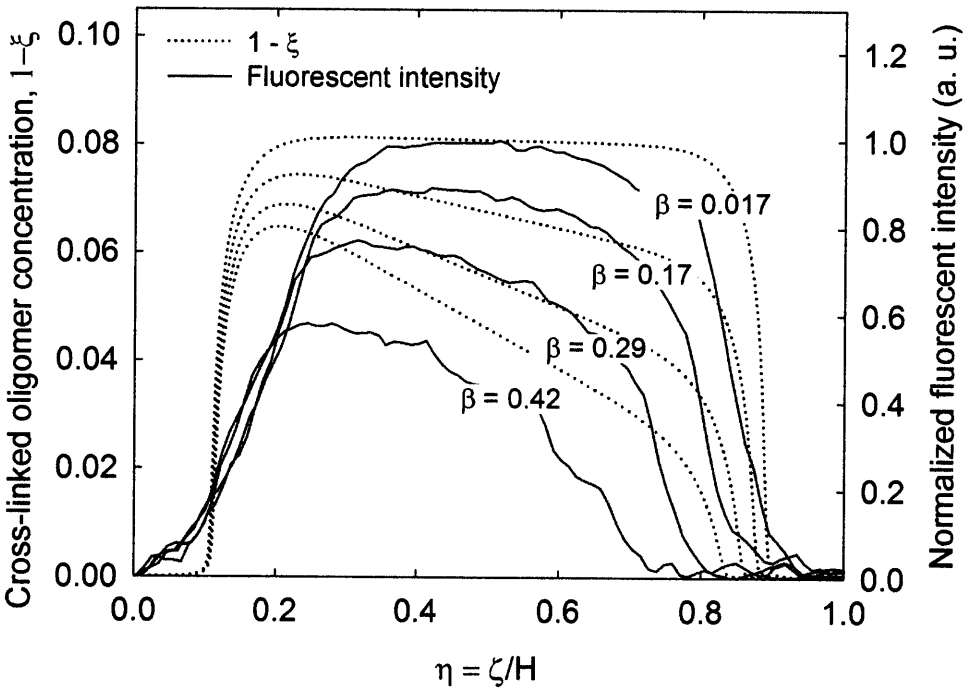

Figure 4-7: Comparison of experimental data and modeling results. Cross-linked oligomer concentration (1- ξ, shown as dotted lines and acquired from simulation) versus dimensionless height in channel η. Right axis and solid curves show for comparison the fluorescent signals across the η-direction as acquired from particles synthesized in the presence of UV absorbing dye.

We have identified two potential explanations for the discrepancies between the simulation results and the experimental profiles at the top and bottom edges of the particles. First, the simulation of particle formation does not take into account swelling effects after particle synthesis. The lower the crosslinking density of a gel network, the more likely it is that network will swell in a solvent. The gradient in the crosslink density across the particle when it is prepared in the presence of UV absorbing entities should then result in the particle swelling to different extents within the particle. The second reason is that we used rhodamine B bearing a methacrylate group in order to incorporate it covalently within the gel. The assumption behind Figure 4-7 is that the rhodamine incorporation rate in the four cases is the same, providing an estimate of the relative cross-linked monomer concentrations. However, the reaction rate of rhodamine could depend on the local concentration of free-radicals, which is not taken into account for this species in the model. This may explain why the results for the particle region with 45 mg/ml of dye concentration do not agree with our model predictions as well as it does for other concentrations. We believe that Figure 4-7 provides useful information on hydrogel particle synthesis with non-functionalizing UV absorbing materials, given the limited set of assumptions applied.

4.4.4 Particle synthesis under uniform magnetic field

To better understand the effects of magnetic bead distribution within the monomers during polymerization, we performed an experiment under an applied uniform magnetic field directed normal to the observation plane (Figure 4-8) to assemble the magnetic particles in chains in the same direction in which light propagates through the monomer. This provided bead-free spaces for light penetration through to the top of the channel (Figure 4-8(a)). Our hypothesis was that nearby free-radicals would polymerize around magnetic chains due to slight free radical diffusion. Magnetic beads in the monomer solution were chained in the microfluidic channel with spaces between chains and particles were polymerized as in other syntheses as shown in Figure 4-8 (b). As expected, the height of the particle prepared under the uniform magnetic field (0.76 H) was larger than that without a magnetic field (0.69 H). This trend can be qualitatively discerned in Figure 4-8 (c-f). The dimensionless particle height of 0.76 with the chained beads was very close to the expected value of 0.78 predicted in the simulation with $\beta = 0.017$, value when no opaque material is added. In this case, the microscopic or local UV absorbance in the channels between the chains determined the particle height and the degree of cross-linking, rather than total absorbance averaged over the entire particle. Additionally, because it is the local absorbance between the chains that largely determines the overall particle thickness, chaining of the beads allows us to create thicker particles compared to randomly dispersed beads under the same synthesis conditions.

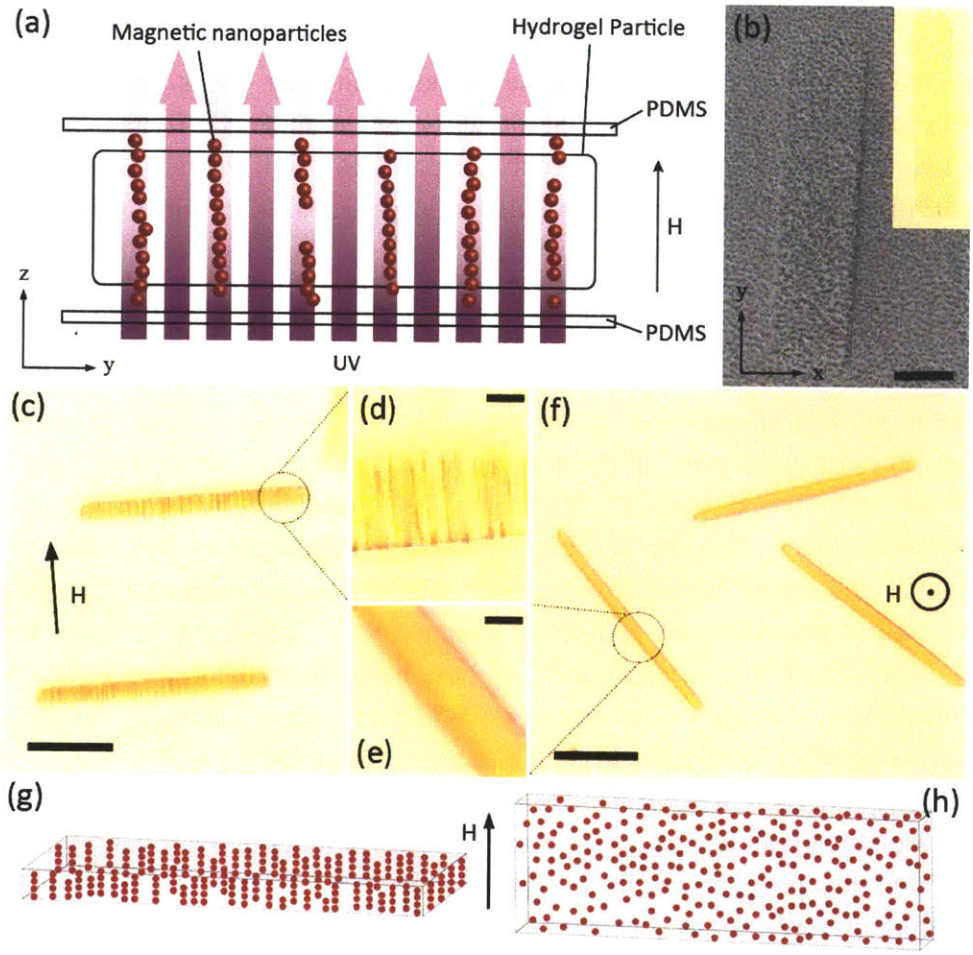

Figure 4-8: Particles synthesized in the presence of an external magnetic field. (a) A uniform magnetic field was applied just before UV exposure to form chained magnetic beads. Although the chains absorb UV, microparticles can be created due to polymerization reaction nearby the chains (shown schematically as purple in the image). (b) Top-view of the microfluidic channel with 25 mg/ml magnetic beads during the synthesis. The inset image is a washed particle after the synthesis. (c) Particles with magnetic chains embedded. A uniform magnetic field was applied to conveniently observe the side of particles. (d), (e) Magnified image of the circled part of (c), (f) respectively. (f) Particles with 25 mg/ml magnetic beads synthesized with no magnetic field present. (g-h) Illustration of particle alignments under the magnetic field. The particle in (g) contains chained magnetic beads while the particle in (h) has embedded magnetic beads with a random distribution.

We next applied a magnetic field to flip the particles on their edges, so that they could be observed from their sides. Interestingly, the direction of the magnetic field required to flip the particle for height observation was different for particles with chained magnetic beads and homogenously distributed magnetic beads. Magnetic particles align with a field based on the most energetically favorable orientation; therefore, in the case of particles generated in the presence of a field, the already chained magnetic beads align with the field, while for homogeneously distributed beads, it is the entire hydrogel particle that aligns with the field, as shown experimentally in Figure 4-8 (c) – (f) and schematically in Figure 4-8 (g) and (h). These figures represent particle alignment under weak fields; with stronger fields, the particles would overcome the forces of gravity and align along their longest axes. Although particle synthesis in the presence of an external magnetic field has been reported by other groups,[44,54-57] the significance of our work is that the particle synthesis approach allows for independent control over its geometric and magnetic anisotropies. This enables the assembly of magnetic particles in a desired orientation regardless of geometric anisotropy. This method provides the ability to create many other functional anisotropies, i.e. mechanical strength, dielectric constant and elasticity. Furthermore, we believe that our work can lead to a new method to fabricate phononic particles by applying other external fields, such as an electric field.

We have discussed the effect of opaque materials on the synthesis of hydrogel microparticles and have demonstrated the application of these understandings in the design of new types of hydrogel particles. For certain applications, one can functionalize hydrogel particles with nanoparticles. First, it is necessary to examine the feasibility and ease of nanoparticle incorporation by investigating the UV absorptivity of the material. Table 4-4 includes published UV absorptivity data as a function of material, size, and wavelength. One can examine our model with dimensionless numbers to gain an understanding of the nature of the resulting particles. To calculate the dimensionless numbers used in our model, the experimental parameters [PI], I_0, H, D_O and ε_2 are needed. In the case of incorporating materials of high UV absorbance, an external field can often be used to improve the outcome as external fields can create patterns in the monomer solutions and allow for increased local UV intensities. In the presence of an external field, ε_2 should be a local UV absorptivity rather than a bulk parameter. These parameters are calculated as follows:

$$\alpha = 1.72\times10^{-8}[\mathrm{PI}]I_0 \tag{4-11}$$

$$\beta = \left(1.6\cdot[\mathrm{PI}]+\varepsilon_2[\mathrm{OM}]\right)H \tag{4-12}$$

$$Da_1 = 7.44\times10^{7}\frac{H^2}{D_O} \tag{4-13}$$

$$Da_2 = 3.72\times10^3 \frac{H^2}{D_O} \qquad (4\text{-}14)$$

The dimensionless numbers α, Da_1, and Da_2, are also dependent on other parameters of the system, and were discussed in our previous work.[45]

Table 4-4: UV absorbance information from literature. UV absorbance depends on the size, nanoparticle concentration, and wavelength.

Material	Size (nm)	Molar Absorptivity (cm^{-1} M^{-1})	Wavelength (nm)	Ref
CdS	2.4	2×10^5	365	58
CdSe	4	7×10^5	365	58
	5.5	1×10^6		
CdSe	15	2×10^5	350	59
	18	3×10^5		
	21	1×10^6		
	23	2×10^6		
	27	3×10^6		
	30	4×10^6		
Au	9	5×10^7	400	60
	22	8×10^8		
	48	7×10^9		
	99	5×10^{10}		
TiO_2	2.1 – 26.7	2×10^2	350	61
TiO_2	60	5×10	350	62
	175	3×10		

4.5 Conclusion

In summary, we demonstrate the synthesis of opaque hydrogel particles using flow-lithography and simulate the properties of the particles. We investigated the effect of UV absorbance on the particle synthesis, comparing empirical observations with modeling results. The insight from our understanding enabled us to create a particle architecture with two independent anisotropies by using magnetic beads chained under a uniform magnetic field during synthesis. This study helps

advance the understanding of the synthesis of a diverse class of particles with variable shape, chemistry, and functionality. We believe that our model and new synthesis techniques with opaque materials can lead to rational particle design with minimal experimentation.

4.6 Reference

(1) Cushing, M. C.; Anseth, K. S. *Science* **2007**, *316*, 1133.

(2) Peppas, N. A.; Hilt, J. Z.; Khademhosseini, A.; Langer, R. *Adv Mater* **2006**, *18*, 1345.

(3) Ulijn, R. V.; Bibi, N.; Jayawarna, V.; Thornton, P. D.; Todd, S. J.; Mart, R. J.; Smith, A. M.; Gough, J. E. *Mater Today* **2007**, *10*, 40.

(4) Lee, K. Y.; Mooney, D. J. *Chem Rev* **2001**, *101*, 1869.

(5) Malkoch, M.; Vestberg, R.; Gupta, N.; Mespouille, L.; Dubois, P.; Mason, A. F.; Hedrick, J. L.; Liao, Q.; Frank, C. W.; Kingsbury, K.; Hawker, C. J. *Chem Commun* **2006**, 2774.

(6) Nath, N.; Chilkoti, A. *Adv Mater* **2002**, *14*, 1243.

(7) Anseth, K. S.; Metters, A. T.; Bryant, S. J.; Martens, P. J.; Elisseeff, J. H.; Bowman, C. N. *J Control Release* **2002**, *78*, 199.

(8) Kawaguchi, H. *Prog Polym Sci* **2000**, *25*, 1171.

(9) Smith, W. V.; Ewart, R. H. *J Chem Phys* **1948**, *16*, 592.

(10) Dendukuri, D.; Tsoi, K.; Hatton, T. A.; Doyle, P. S. *Langmuir* **2005**, *21*, 2113.

(11) Hwang, D. K.; Dendukuri, D.; Doyle, P. S. *Lab Chip* **2008**, *8*, 1640.

(12) Shepherd, R. F.; Conrad, J. C.; Rhodes, S. K.; Link, D. R.; Marquez, M.; Weitz, D. A.; Lewis, J. A. *Langmuir* **2006**, *22*, 8618.

(13) Xu, S.; Nie, Z.; Seo, M.; Lewis, P.; Kumacheva, E.; Stone, H. A.; Garstecki, P.; Weibel, D. B.; Gitlin, I.; Whitesides, G. M. *Angewandte Chemie-International Edition* **2005**, *117*, 734.

(14) Kumacheva, E.; Garstecki, P. *Microfluidic reactors for polymer particles*; Wiley: Hoboken, N.J., 2011.

(15) Rolland, J. P.; Maynor, B. W.; Euliss, L. E.; Exner, A. E.; Denison, G. M.; DeSimone, J. M. *J Am Chem Soc* **2005**, *127*, 10096.

(16) Dendukuri, D.; Pregibon, D. C.; Collins, J.; Hatton, T. A.; Doyle, P. S. *Nat Mater* **2006**, *5*, 365.

(17) Dendukuri, D.; Gu, S. S.; Pregibon, D. C.; Hatton, T. A.; Doyle, P. S. *Lab Chip* **2007**, *7*, 818.

(18) Haghgooie, R.; Toner, M.; Doyle, P. S. *Macromol Rapid Comm* **2010**, *31*, 128.

(19) Bong, K. W.; Bong, K. T.; Pregibon, D. C.; Doyle, P. S. *Angew Chem Int Edit* **2010**, *49*, 87.

(20) Pregibon, D. C.; Toner, M.; Doyle, P. S. *Science* **2007**, *315*, 1393.

(21) Shepherd, R. F.; Panda, P.; Bao, Z.; Sandhage, K. H.; Hatton, T. A.; Lewis, J. A.; Doyle, P. S. *Adv Mater* **2008**, *20*, 4734.

(22) Panda, P.; Ali, S.; Lo, E.; Chung, B. G.; Hatton, T. A.; Khademhosseini, A.; Doyle, P. S. *Lab Chip* **2008**, *8*, 1056.

(23) Appleyard, D. C.; Chapin, S. C.; Doyle, P. S. *Anal Chem* **2011**, *83*, 193.

(24) Chapin, S. C.; Pregibon, D. C.; Doyle, P. S. *Angew Chem Int Edit* **2011**, *50*, 2289.

(25) Murray, C. B.; Kagan, C. R.; Bawendi, M. G. *Annu Rev Mater Sci* **2000**, *30*, 545.

(26) Im, J. S.; Bai, B. C.; In, S. J.; Lee, Y. S. *J Colloid Interf Sci* **2010**, *346*, 216.

(27) Li, J.; Hong, X.; Liu, Y.; Li, D.; Wang, Y. W.; Li, J. H.; Bai, Y. B.; Li, T. J. *Adv Mater* **2005**, *17*, 163.

(28) Pankhurst, Q. A.; Connolly, J.; Jones, S. K.; Dobson, J. *J Phys D Appl Phys* **2003**, *36*, R167.
(29) Isojima, T.; Suh, S. K.; Vander Sande, J. B.; Hatton, T. A. *Langmuir* **2009**, *25*, 8292.
(30) Harada, T.; Hatton, T. A. *Langmuir* **2009**, *25*, 6407.
(31) Singh, H.; Laibinis, P. E.; Hatton, T. A. *Nano Lett* **2005**, *5*, 2149.
(32) Zerrouki, D.; Baudry, J.; Pine, D.; Chaikin, P.; Bibette, J. *Nature* **2008**, *455*, 380.
(33) Chen, C. H.; Abate, A. R.; Lee, D. Y.; Terentjev, E. M.; Weitz, D. A. *Adv Mater* **2009**, *21*, 3201.
(34) Bucak, S.; Jones, D. A.; Laibinis, P. E.; Hatton, T. A. *Biotechnol Progr* **2003**, *19*, 477.
(35) Moeser, G. D.; Roach, K. A.; Green, W. H.; Hatton, T. A.; Laibinis, P. E. *Aiche J* **2004**, *50*, 2835.
(36) Gerber, R.; Birss, R. R. *High gradient magnetic separation*; Research Studies Press: Chichester, NY, 1983.
(37) Yavuz, C. T.; Mayo, J. T.; Yu, W. W.; Prakash, A.; Falkner, J. C.; Yean, S.; Cong, L. L.; Shipley, H. J.; Kan, A.; Tomson, M.; Natelson, D.; Colvin, V. L. *Science* **2006**, *314*, 964.
(38) Dreyfus, R.; Baudry, J.; Roper, M. L.; Fermigier, M.; Stone, H. A.; Bibette, J. *Nature* **2005**, *437*, 862.
(39) Zhang, L.; Abbott, J. J.; Dong, L. X.; Kratochvil, B. E.; Bell, D.; Nelson, B. J. *Appl Phys Lett* **2009**, *94*, 064107.
(40) Ghosh, A.; Fischer, P. *Nano Lett* **2009**, *9*, 2243.
(41) Yuet, K. P.; Hwang, D. K.; Haghgooie, R.; Doyle, P. S. *Langmuir* **2010**, *26*, 4281.
(42) Bong, K. W.; Chapin, S. C.; Doyle, P. S. *Langmuir* **2010**, *26*, 8008.
(43) Kim, H.; Ge, J.; Kim, J.; Choi, S.; Lee, H.; Lee, H.; Park, W.; Yin, Y.; Kwon, S. *Nat Photonics* **2009**, *3*, 534.
(44) Lee, H.; Kim, J.; Kim, H.; Kim, J.; Kwon, S. *Nat Mater* **2010**, *9*, 745.
(45) Dendukuri, D.; Panda, P.; Haghgooie, R.; Kim, J. M.; Hatton, T. A.; Doyle, P. S. *Macromolecules* **2008**, *41*, 8547.
(46) Suh, S. K.; Bong, K. W.; Hatton, T. A.; Doyle, P. S. *Langmuir* **2011**, *27*, 13813.
(47) Tang, J.; Myers, M.; Bosnick, K. A.; Brus, L. E. *J Phys Chem B* **2003**, *107*, 7501.
(48) Kızılel, S.; Pérez Luna, V. H.; Teymour, F. *Macromolecular theory and simulations* **2006**, *15*, 686.
(49) Decker, C.; Jenkins, A. D. *Macromolecules* **1985**, *18*, 1241.
(50) Lecamp, L.; Lebaudy, P.; Youssef, B.; Bunel, C. *Polymer* **2001**, *42*, 8541.
(51) Goodner, M. D.; Bowman, C. N. *Chemical Engineering Science* **2002**, *57*, 887.
(52) Chen, C. C.; Hirdes, D.; Folch, A. *P Natl Acad Sci USA* **2003**, *100*, 1499.
(53) Andrzejewska, E. *Prog Polym Sci* **2001**, *26*, 605.
(54) Dyab, A. K. F.; Ozmen, M.; Ersoz, M.; Paunov, V. N. *J Mater Chem* **2009**, *19*, 3475.
(55) Seiffert, S.; Romanowsky, M. B.; Weitz, D. A. *Langmuir* **2010**, *26*, 14842.
(56) Nunes, J.; Herlihy, K. P.; Mair, L.; Superfine, R.; DeSimone, J. M. *Nano Lett* **2010**, *10*, 1113.
(57) Kim, S. H.; Sim, J. Y.; Lim, J. M.; Yang, S. M. *Angew Chem Int Edit* **2010**, *49*, 3786.
(58) Yu, W. W.; Qu, L. H.; Guo, W. Z.; Peng, X. G. *Chem Mater* **2003**, *15*, 2854.

(59) Leatherdale, C. A.; Woo, W. K.; Mikulec, F. V.; Bawendi, M. G. *J Phys Chem B* **2002**, *106*, 7619.
(60) Link, S.; El-Sayed, M. A. *J Phys Chem B* **1999**, *103*, 8410.
(61) Serpone, N.; Lawless, D.; Khairutdinov, R. *J Phys Chem-Us* **1995**, *99*, 16646.
(62) Cabrera, M. I.; Alfano, O. M.; Cassano, A. E. *J Phys Chem-Us* **1996**, *100*, 20043.

Chapter 5

Magnetic particles for enhanced biomolecule detection

5.1 Introduction

Magnetic particles have enhanced performance and simplified workflow in separation processes,[1-2] catalysis,[3] and biotechnology,[4-5] as magnetic particles can be manipulated using external magnetic fields and bear chemical or biological functionality. Within the field of microfluidics, multifunctional magnetic particles have been used for mixing,[6] display,[7] separation,[8] encoding,[9] and immunoassays.[10-11]

Magnetic particles can bring microscopic spatial control or local structure to a system in the presence of external magnetic fields. As an example, spherical magnetic particles assemble to form chains aligned with a homogeneous magnetic field. Field assisted patterning of magnetic particles has been used for DNA separation[12], cell enrichment[13] , and protein digestion,[14] by providing chain lattices with tunable spacing in confined systems. In addition, three-dimensional clusters of magnetic gels have been created on patterned magnets to study cellular structures.[15] Magnetic forces can not only for the assembly of microparticles, but also for the retrieval of particles from previously built structures. For example, cells grown on magnetic microrafts can be released from the patterned substrates and collected with magnets for sorting and subsequent single cell studies.[16]

We reported the combination of magnetic materials and graphically-encoded hydrogel particles, which were created via microfluidic stop-flow lithography (SFL).[17] Such particles can serve as a

versatile suspension-array platform for the high-performance, multiplexed detection of a range of biomolecules.[18] In multiplex assays, where multiple targets are simultaneously quantified in a single sample, each particle contains one or more spatially-separated probe regions and a unique graphical code region used to identify those probe species on that particle. The encoded particles have been used for sensitive, multiplexed quantitation of DNA,[18] microRNA (miRNA),[19] and proteins[20-21] with readout in static imaging or flow-based sysems.[22] In particular, our miRNA assays utilize not only hybridization of nucleic acids to probes embedded in the particles, but also enzymatic reaction within the substrate and subsequent binding of a protein reporter. These assays require non-fouling, porous substrates functionalized with DNA probes that are accessible for target capture and subsequent enzymatic manipulation.

Diagnostic tools capable of handling small sample volumes are important as most clinical samples are very limited and precious. To address this concern, researchers have used engineered devices such as substrate-patterned microwells to provide a dramatic improvement in assay sensitivity,[23-24] with the efficient use of samples. Unfortunately, microwells are not well-suited for reagent exchange due to practical limitations in liquid dispensing.[23] The use of particle-based biosensors may help overcome this shortcoming; the deposition of particles into patterned microwells can provide a simple means to achieve robust spatial control, small volume reaction, and ease of transport. However, the combination of microwells and particle-based biosensors has not been studied extensively due to difficulties in achieving uniform particle distribution and the lack of a means for single-particle manipulation. In this situation, multifunctional magnetic particles could be used to provide precise control and manipulation, but have been challenging to make in an efficient manner.

We demonstrated the synthesis and use of magnetic, barcoded hydrogel particles. While the addition of magnetic material to these particles simplified their manipulation and processing, their synthesis was greatly complicated by the need for a perfusion stream, with flow perpendicular to the monomer stream, in order to eliminate unincorporated magnetic beads that could foul the particles during collection.[17] An alternate approach to creating magnetic particles is two-step polymerization: after a magnetic region is made using one monomer, a new monomer is introduced and a region containing another chemistry is formed around it.[9] Beyond lithographic methods, other means to creating multifunctional magnetic particles face their own set of challenges. Two-region Janus magnetic microparticles, synthesized using two-phase microfluidic systems, require precise viscosity matching between phases[25-26] or the use of external magnetic fields during polymerization.[27-28] These requirements restrict the incorporation of magnetic material to certain regions of the particles, and limit their chemical complexity.

In this work, we present a new framework for the creation and use of magnetic barcoded particles in substrate-patterned microwells. To simplify the synthesis of magnetic bead embedded gel particles, we developed a pH-enhanced washing scheme that allows for the

removal of unincorporated magnetic material from the surface of the particle in a simple post-synthesis rinse. Although rinsing is carried out in high-pH solutions, we demonstrate that particles synthesized with magnetic code and probe regions maintain their chemical and biological functionality for decoding and miRNA detection. We also demonstrate uniform patterning of the magnetic particles in microwells and the selective collection and manipulation of individual particles. In addition to the flexibility afforded by magnetic patterning, the use of microwells also provides a nanoliter-scale volume that can serve as a reaction chamber for particle-based assays. The material in this chapter from Suh, Chapin, Hatton and Doyle, *Small*, submitted. was reproduced

5.2 Experiment methods

5.2.1 Materials

Polymeric particles were made from poly(ethylene glycol) (700) diacrylate (PEG-DA 700, Sigma-Aldrich) and 2-hydroxy-2-methylpropiophenon (Darocur 1173, Sigma-Aldrich) initiator. In pre-polymer solutions, we added poly(ethylene glycol) (200) (PEG 200, Sigma-Aldrich) to obtain desired solubility of Darocur and fluid viscosity. We used 800 nm diameter carboxylate-modified magnetic bead solutions (Seradyn Inc., carboxylate-modified, 5% solids) for magnetic functionalization. Tergitol NP-10 (Sigma Aldrich) or Tween-20 (Sigma Aldrich) was used at 0.05% (v/v) to prevent particle loss due to sticking on pipette tips or tubes. Tris-EDTA (TE) buffer (10 mM tris(hydroxymethyl)-aminomethane, 1 mM ethylenediaminetetraacetic acid, pH = 8.0) was purchased from Rockland Immunochemicals. Oligonucleotide probe for miR-145 (5Acryd/GAT ATA TTT TAA GGG ATT CCT GGG AAA ACT GGA C/3InvdT) was purchased from IDT with an acrydite modification on the 5' end (for covalent incorporation into the gel matrix) and mixed into the probe pre-polymer to give a final concentration of 50 μM. New England Buffer #2 (NEB2), ATP, and T4 DNA ligase were purchased from New England Biolabs. A universal labeling adapter (IDT) and streptavidin-r-phycoerythrin fluorophore (SA-PE, Invitrogen) were used to report binding events for miRNA assays, as described elsewhere.[19]

5.2.2 Microfluidic devices

Microfluidic channels for SFL were fabricated using standard soft-lithography techniques. Polydimethylsiloxane (PDMS, Sylgard 184, Dow Corning) in a 10:1 base-to-curing agent ratio was molded on a patterned silicon wafer (SU-8 photoresist, Microchem), then cured in an oven at 65 °C for 2 hours. Holes for connections to the inlets and outlet were punched with an 18 gauge luer stub adapter. Glass slides were coated with PDMS and partially cured at 65 °C for 22

min. The clean patterned PDMS was assembled with the PDMS-coated glass and then placed in the oven for 45 min. The prepared microfluidic channel was then connected with inlets that were made from pipette tips (ART 10 Reach and ART 200, Molecular BioProducts, Inc) and outlet aluminum tubing (1/16", K&S) for collecting particles after synthesis. For particle synthesis, the devices were mounted on an inverted microscope (Axiovert 200, Zeiss).

5.2.3 Stop-Flow-Lithography setup

We created hydrogel particles in microfluidic devices when flow was stopped. Formed particles were then moved out of the polymerization area via the inflow of fresh monomer solutions. Pulsed flow was operated using automated control scripts for the generation of stop-polymerization-flow cycles, alternating the pressure at all four inlets simultaneously from 0 to 3 psi. The relative width of the inlet streams was controlled by a pressure valve (ControlAir, Inc) and a digital pressure gauge (DPG 100G, Omega Engineering, Inc.). A microscope-mounted UV source (Lumen 200, Prior Scientific, 100% setting) initiated polymerization reactions (75 ms exposure time). Photomasks were placed in the field-stop slot of the microscope, and the desired excitation spectrum was selected using a UV filter (11000v2, Chroma). UV intensity with the 20× objective of the inverted microscope was 3400 mW/cm^2, as measured by a UV power meter (Accu-Cal 30, Dymax). The composition of each prepolymer stream used in this work is summarized in Table 5-1.

Table 5-1: Composition of prepolymer solution in volume %

	PEGDA 700	Darocur 1173	PEG 200	1 x TE	Rhoda-mine	Magnetic solution	DNA	Food coloring
Code	35 %	5 %	20%	39.85 %	0.15 %	N/A	N/A	N/A
Magnetic code	35 %	5 %	N/A	17.85 %	0.15 %	41.5 %	N/A	N/A
Probe	18 %	4.5 %	36 %	41.5%	N/A	N/A	50 μM	N/A
Magnetic probe	18 %	4.5 %	36 %	N/A	N/A	41.5 %	50 μM	N/A
Inert	35 %	5 %	30 %	28 %	N/A	N/A	N/A	2 %

5.2.4 *Washing scheme*

To remove unincorporated magnetic beads, we used high-pH rinse solutions. Particles were washed three times with 1M NaOH aqueous solution and 0.005% (v/v) Tergitol (to prevent sticking of hydrogel particles in pipette tips or Eppendorf tube). To separate unincorporated magnetic beads from hydrogel particles, centrifugation was performed for 10 s. Then, the particles were rinsed with deionized water with 0.005% (v/v) Tergitol three times to decrease pH. For miRNA detection, the particles were suspended and stored in TET (1x TE with 0.05% (v/v) Tween-20).

5.2.5 *miRNA incubation experiments*

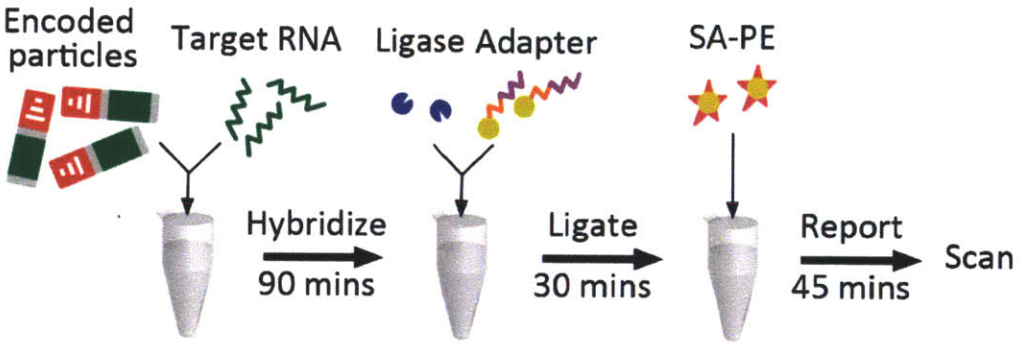

Figure 5-1: Schematic overview of the miRNA assay.

All incubations were carried out in 50 µl volumes of TET within 0.65-mL Eppendorf tubes at a final NaCl concentration of 350 mM. Synthetic miR-145 target sequences were diluted in 1x TE such that the addition of 0.5 µl of target solution to the incubation tube introduced 500 amol of target. A previously prepared mix of four types of particles (12.5 of each type per µl TET) was thoroughly vortexed for 1 min, and 4 µl was introduced to each incubation tube. Incubation with target was carried out at 55°C for 90 min in a thermomixer (Quantifoil Rio) with a mixing speed of 1500 rpm. After hybridization with target, the particles were washed three times with a solution of 500 µl TET containing 50 mM NaCl (R50). Supernatant resulting from centrifugal separation was manually removed from the tube. Following the protocol for a ligation-based labeling scheme described elsewhere (add Chapin Angewandte REF here), the 50 µl of solution at the bottom of the tube was preserved after the third rinse, and 245 µl of a previously prepared ligation master mix (100 µL 10x NEB2, 900 µl TET, 250 nM ATP, 40 nM biotinylated universal adapter sequence, and 800 U/ml T4 DNA ligase) was added to the tube. The mixture was placed

in a shaker (Multi-therm) at 21.5°C for 30 min with a mixing speed of 1500 rpm. After ligation of the biotinylated universal adapters to the captured targets, the particles were rinsed three times with R50. SA-PE (1 mg/ml) was diluted 1:50 in TET and added to the incubation mixture to provide a final dilution of 1:500. Samples were incubated at 21.5°C at 1500 rpm for 45 min. After another three-rinse cycle with R50, particles were rinsed once in 500 µl of PTET (5x TE with 25% (v/v) PEG 400 and 0.05% Tween-20). Prior to use, all PTET was sonicated for 5 min to eliminate aggregations of polymer. For fluorescence analysis, particles were either imaged individually with an Andor CCD camera or with a microfluidic, high-speed flow-through scanning system.[19]

5.2.6 Well experiments

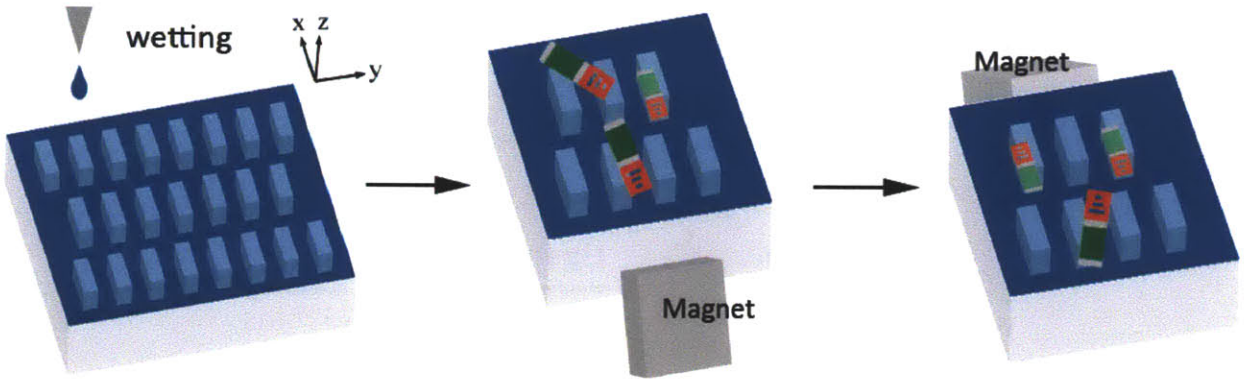

Figure 5-2: Schematic description showing patterned substrate with subsequent addition and manipulation of magnetic particles into microwells.

Wells (300 × 100 × 113 µm) were fabricated using standard soft-lithography techniques. PDMS was molded on a patterned silicon wafer, and then cured in an oven at 65 °C for 2 hours. After removing the PDMS from the wafer, 20 µL of TET was dropped onto the molded wells and distributed with a pipette tip so that the solution could wet the bottom of the wells. Next, 5 µl of particle solution (1 magnetic particle/µL) was dropped onto the wetted surface. Using a hand magnet (KS), particles were rotated to align with the long dimension of the rectangular array of wells and translated across the surface to begin the filling process. To facilitate loading via sedimentation, particles were translated slowly and the angle between the PDMS surface and the hand magnet was ~45°. After all particles had been placed in wells (~2-3 min), five additional particles were deposited and the process was repeated until the desired occupancy had been

reached. More TET solution was gently added every 10 min to prevent the wells and surfaces from drying.

5.2.7 Magnetic tweezer experiment

The magnetic tweezer device used in this work was originally developed by Lammerding *et al.*[29] The core in Figure 5-3 (a) was made of high-magnetic-permeability iron (CMI-C, CMI Specialty Products, Bristol, CT) machined to a sharp tip with a width of 200 μm. Then, it was subsequently annealed according to the manufacturer's specifications. The geometry of the sharp tip creates high magnetic field gradients and thus exerts large forces on magnetic particles. The core metal is wrapped with AWG 19 copper magnet wire over a length of 7.2, producing a wire turn density of approximately 4200 m^{-1}. By fitting the tweezer into a manual micromanipulator (MX110, Siskiyou, Grants Pass, OR), the instrument was able to be precisely placed beside an inverted microscope (Axiovert 40 CFL, Carl Zeiss AG, Oberkochen, Germany). The wires were connected to a DC power supply (GPS-2303, GWInstek, Taipei, Taiwan), and the magnetic tweezer was operated with current of $I = 0.15$ A. During manipulation, the average distance from magnetic particles to the tweezer was ~150 μm. As particles were collected from the wells using vertical forces, the magnetic tweezer was rotated 90° in order to measure the relevant force. Magnetic beads with a diameter of 800 nm (0.1 v/v %) were suspended in a glycerol (80 v/v %) and water (20 v/v %) solution with viscosity of 60 cP and exposed to the rotated tweezer. Images were taken at one-second intervals to obtain velocity estimates of the various beads, and then a magnetic force could be calculated from the velocity and distance measurements.

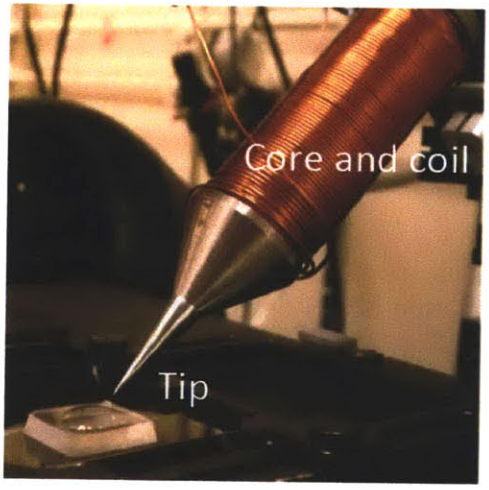

Figure 5-3: The magnetic tweezer set-up on the microscope stage. The tip was dipped in the solution when current was sent through the coil.

5.3 Results and discussion

5.3.1 pH enhanced washing

Figure 5-4 shows magnetic, barcoded hydrogel particles synthesized using SFL. In this process, the particle shape is dictated by the shape of features on a transparency mask in the path of the UV light used to form the particles, while functionalities of each region were determined by the fluid inlets in the microfluidic channel. Two inlets were involved in this synthesis, creating particles with two distinguishable regions, one of which contained magnetic materials embedded in the polymer matrix. As the size of magnetic beads used (800 nm) is bigger than typical pore size of our particles (5 nm), the beads are physically entrapped in hydrogel particles. Also, the internal features of barcode are well-defined, demonstrating that the magnetic beads do not significantly reduce the resolution of the SFL process.

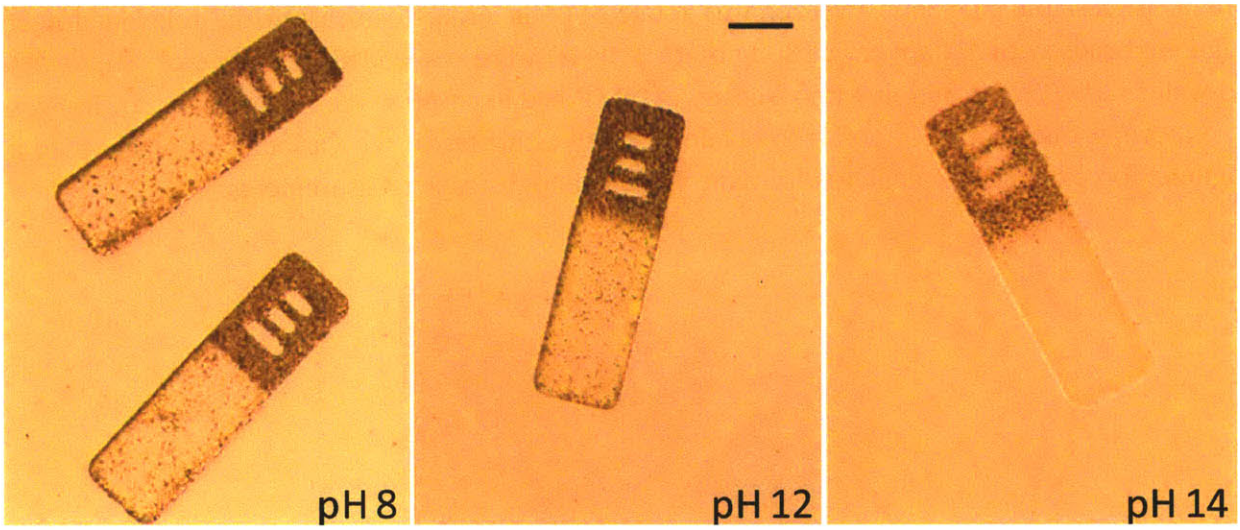

Figure 5-4: Demonstration of pH-enhanced rinsing. The high pH solution decomposes ester groups to carboxyl and alcohol groups. Optical images of magnetic barcode particles after rinsed with pH 8, 12, and 14 solutions, respectively. The scale bar is 50 μm.

After synthesis, particles are collected in a mixture of unreacted monomer, magnetic beads, and buffer. To avoid the issue of having magnetic beads attach to the surface of the hydrogel particles in this mixture, the Doyle group previously used a perfusion stream to immediately

remove the magnetic beads during synthesis.[17] However, it is not always desirable to handle multiple exit streams in a synthesis device. Here, we present another method to remove the magnetic beads that are not incorporated in the hydrogel particle matrix via rinsing with a high pH solution. We used carboxylated magnetic beads because they are dispersed easily in PEG-DA solutions. This is because the carboxylated bead surfaces are deprotonated in high pH solutions forcing the beads to electrostatically repel each other. Furthermore, well-dispersed magnetic beads are more easily removed from hydrogel surfaces than are aggregated beads. The hydrogel particles have characteristic sizes that are 100s of microns while the magnetic beads used have a characteristic size less than one micron; therefore, a short centrifugation of 10s can be used to effectively separate hydrogel particles from magnetic beads.

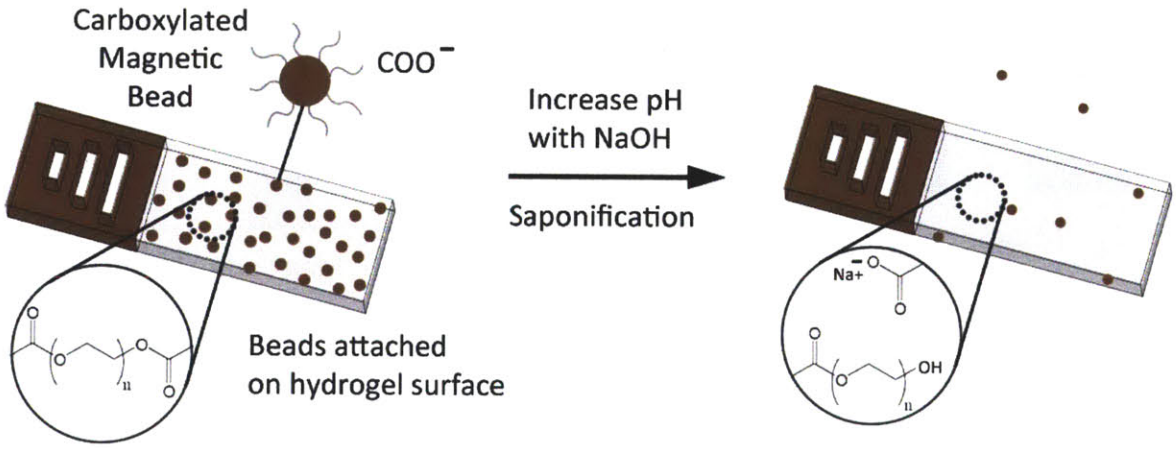

Figure 5-5: Schematic of polymer saponification with high pH.

A range of pH was tested for rinsing. As shown in Figure 5-5 higher pHs are more effective at removing the magnetic beads on the hydrogel particles. While the particles imaged after washing with pH 8 and 12 solutions still have magnetic beads on their surface, those rinsed with pH 14 show clean surfaces. We note that all of the solutions used have a higher pH than pKa of COOH.[30] This implies that the attachments of beads on the hydrogel surfaces are due to interaction between hydrogels and beads rather than beads with other beads. As ester groups like those present in the hydrogel network can be broken with high pH and increased temperature, it is likely that some of esters in cross-linked PEG-DA could be hydrolysized during high-pH rinsing as shown in Figure 5-5. This process of saponification produces carboxyl and alcohol groups from the broken esters in PEG-DA hydrogel particles.[30] Therefore, these newly created carboxyl groups on the hydrogel particles could repel the magnetic beads bound at their surface. To demonstrate the effect of saponification, we have observed complete decomposition of

hydrogel particles under 3M NaOH at 65°C in 10 mins. However, in the case of rinsing, only a small degree of decomposition occurs, as we exposed particles to pH 14 only for about 1 min at room temperature. This understanding about the effect of high pH on hydrogel particles enables us not only to create clean hydrogel particle surfaces but also to tune hydrogel pore size with controlled time and temperature.

5.3.2 miRNA detection

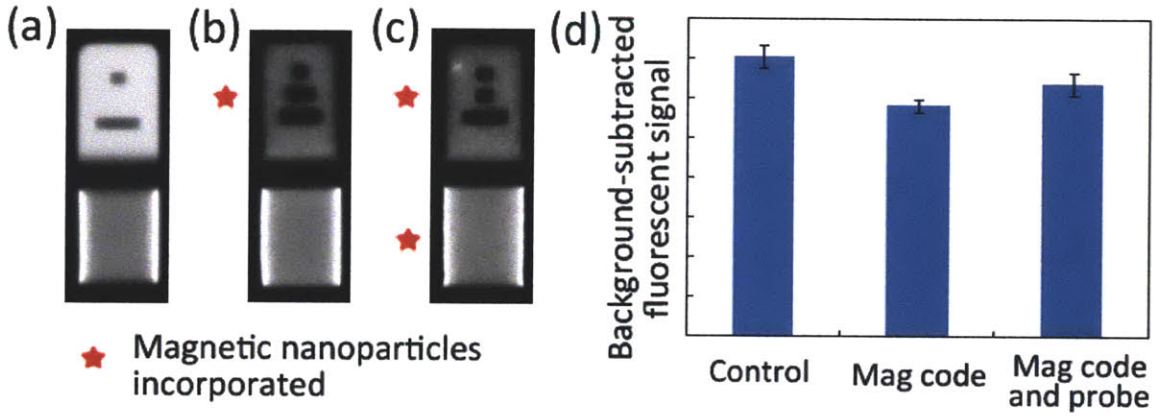

Figure 5-6: miRNA detection using magnetic barcode particles after high-pH rinsing. (a) Fluorescent images of control particle with no magnetic material (b), a particle with a magnetic code (c), and a particle with magnetic code and magnetic probe, all shown after a miRNA assay. (d) Fluorescent signal from miRNA detection after scanning in a flow-through device. The error bars represent intra-run standard deviation.

To ensure biofunctionality after the saponification process, we performed assays to quantify miRNA. Three types of particles were used in this experiment including control, non-magnetic particles (with barcode 103), particles with a magnetic code region (123), and particles with magnetic code and probe regions (113) were mixed with one tube and hybridized with target RNA. After target capture, we used T4 DNA ligase to attach a universal biotinylated oligonucleotide adapter to the 3' end of captured targets. Finally, a low-salt rinse was used to remove un-ligated adapter, and streptavidin-PE (SA-PE) was used for fluorescent reporting. Particles were imaged using a fluorescence microscope, as shown in Figure 5-6 (a), (b), (c). Captured target is indicated by fluorescent signal in the particle probe regions. Particles were also scanned using our flow-through system previously developed, and the results showing the

average over 10-15 particles of each type are presented in Figure 5-6 (d).[22] While the control particles have slightly higher integrated signals, the pH treated particles still show a bright signal with excellent particle-to-particle reproducibility. This suggests that the high-pH rinsing scheme does not degrade or release the DNA probes a significant enough amount to substantially decrease the performance of particles for miRNA detection.

We also observe signal reduction in the code regions that bear magnetic materials, though code features remain mechanically stable in high-speed scanning flows and can still be readily identified. Due to reduced UV penetration through magnetic-bead containing prepolymer during synthesis, the thickness of magnetic regions is smaller than that of non-magnetic regions. For coding regions covalently functionalized with rhodamine-acrylate, this leads to a reduction in the loading of fluorophore and thus lower fluorescent signal arising from the barcode during analysis.[22] This affect can easily be corrected by simply increasing the concentration of rhodamine-acrylate in the code pre-polymer. Regarding the magnetic probe regions investigated in this work, the miRNA hybridization events take place predominantly at the surface of the hydrogel (due to relatively faster reaction with probe than diffusion through the gel),[31] and therefore, the signal generated from the probe region is not affected by changes in the thickness to the same extent seen with the fluorophore loading of the code.

The ability to incorporate magnetic materials in both code and probe regions provides a significant amount of versatility, which is especially useful in multiplex assays that require efficient use of particle area. For example, with the methods presented here, code regions can have two simultaneous functionalities (identifying the particle and responding to external magnetic fields), and probe regions can also have two functionalities (embedding DNA probe molecules and responding to magnetic fields). This is in contrast to previously developed methods, which required a separate patch on the gel for the immobilization of magnetic material. Combining functionalities with the synthesis reported here preserves more of the particle for encoding and/or biomolecule capture. Also, the magnetic beads used here are stabilized with carboxylated groups – this chemistry has been used extensively for functionalization with DNA[32] or nanoparticles.[33] Although carboxylated magnetic beads can increase the functionality of hydrogel particles, we have encountered challenges incorporating them during synthesis due to a decrease in polymerization efficiency. This is because magnetic materials absorb UV, which is necessary for photolysis of the initiator. Therefore, optimization of prepolymer solutions might be necessary for some applications.

5.3.3 Magnetic particles in microwells

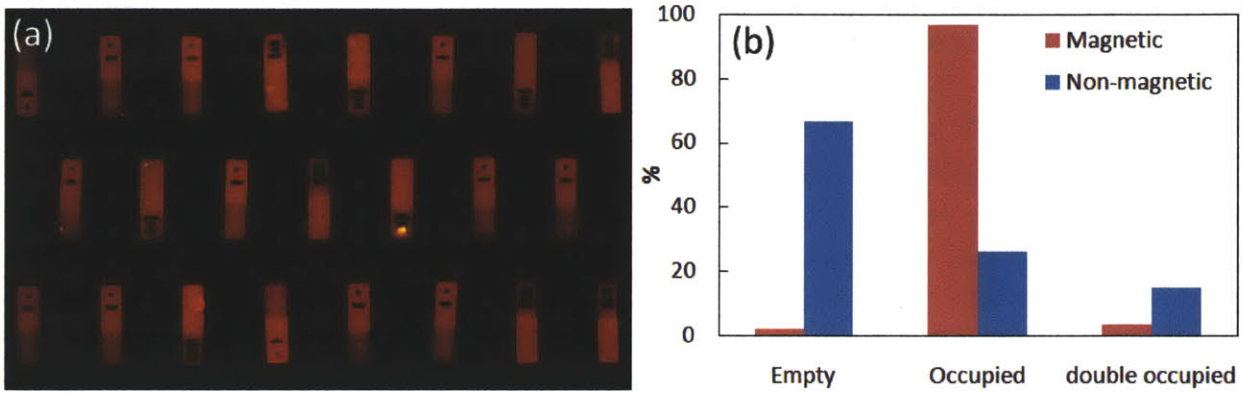

Figure 5-7: Patterning of the magnetic barcode particles in microwells using a hand magnet. (a) Fluorescent images of microwells occupied with the two types of magnetic particles. (b) Statistics of well occupancy with magnetic (red) and non-magnetic (blue) barcoded particles.

After demonstrating that the particles maintain functionality for biological assays, we developed a means of arranging the particles in small-volume microwells. Magnetic barcode particles were manipulated using hand magnets to position them in microwells as explained above. These magnets were able to rotate and translate magnetic particles effectively; the magnetic regions of the particles align with the magnetic field in energetically favored configuration. The hand magnet was rotated to align the particles with the x-axis, as shown in Figure 5-2. For translation of the particles into the microwells, we tilted the magnet 45 degrees downward to direct particles along the x-axis and also into the wells. If the magnet does not pull the particles downward, the particles pass by the wells rather than fall into them. As shown in Figure 5-7 (a), we were able to occupy all the wells with magnetic particles. As it is difficult to move many particles in the desired direction simultaneously, approximately five particles were dropped on the surface of PDMS at a time and the processes were repeated to occupy all the wells. As shown in Figure 5-7 (a), we used two types of particles were dropped sequentially to occupy the wells. These particles were not distributed randomly, as the particles initially dropped were located in the closest wells. If a random distribution is important for certain applications, the particle types may be mixed prior to deposition.

We investigated the statistics of hydrogel particle occupancy as shown in Figure 5-7 (b). While most of the wells contained magnetic particles, more than half of the wells did not. Non-magnetic particles can only be manipulated randomly with agitation, which is not a easily

controllable. We selected wells with the height of 113 μm in order to give a room to contain a reasonable sample volume, which could be biological fluids or cells, demonstrating potential use of microwells as microreactors. Due to large heights, more than two particles can be placed in one well. Depending on the initial dropping position, multiple particles can settle into each well. However, we were able to manipulate the magnetic particles before they settled in order to avoid the issue of double occupancy. Although double occupancy can be avoided by using shorter wells, the use of magnetic particles brings more freedom to this process. It becomes more challenging to fill wells with magnetic particles as occupancy is increased. Although we used rectangular arrangements for the wells in this experiment, various alternate configurations could be used to create more interesting patterns. Furthermore, particles can be recovered from or repositioned in wells using magnetic forces, allowing even more complex patterns to be built.

The deposition of hydrogel particles in patterned microwells using external magnetic forces could be very beneficial for high-throughput or high-sensitivity applications as each microwell can act as an isolated reaction chamber. To utilize microwells for reactions with multiple processing steps, it is necessary to retain the particles within the wells while solutions are exchanged. It is common practice to cover microwells with a glass substrate during reaction/incubation[19] in order to prevent fluid communication between wells and evaporation of liquid. When removing such a glass containment substrate from our well setup, it was observed that non-magnetic particles can easily be pulled out of the wells and adsorbed onto the glass surface due to strong suction forces. This issue can be overcome by using magnetic particles, which can be immobilized at the bottom of the wells by applying a downward magnetic force. This can be accomplished by simply placing hand magnets underneath the wells, as shown in Figure 5-8.

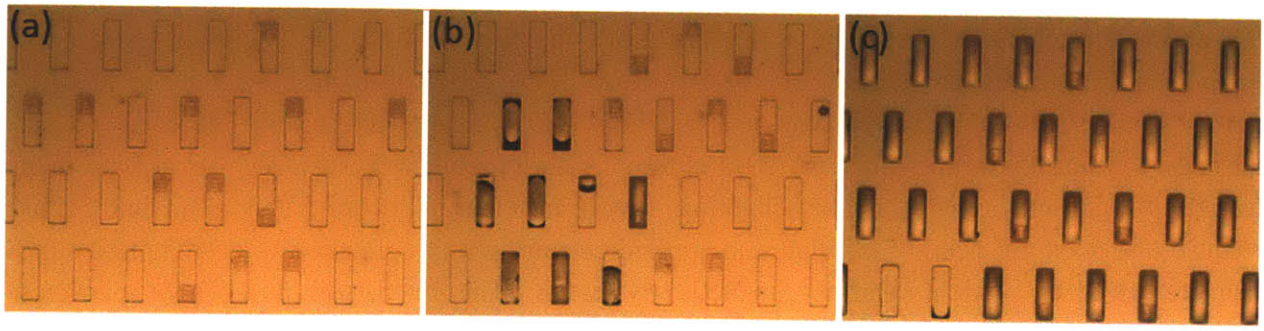

Figure 5-8: Usage of magnetic particles in microwells. (a) Particles were located in wells. (b) Wells were covered with cover-glass. (c) Cover-glass was removed while magnet attracted particles at the bottom of wells.

5.3.4 Selective recovery of particles using magnetic tweezer

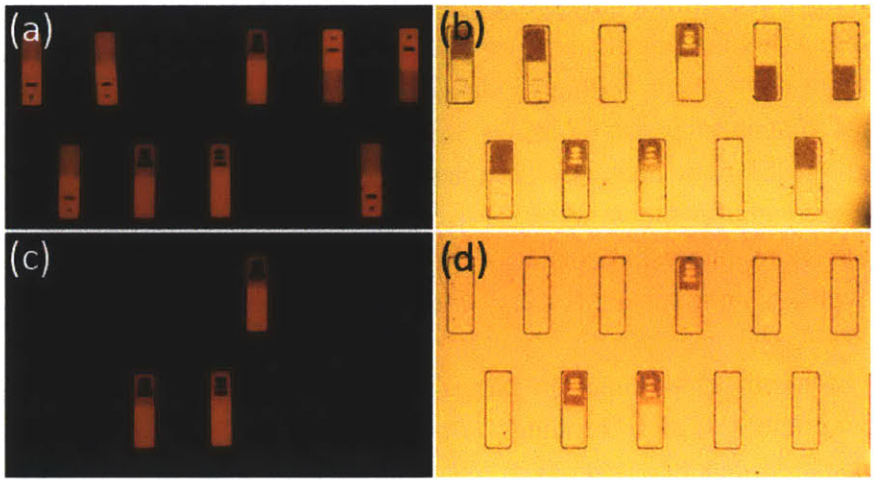

Figure 5-9: Selective collection of magnetic particles using a magnetic tweezer. (a) Fluorescent image of microwells filled with two types of particles with corresponding bright-field image (b). (c) Fluorescent image of microwells shown in (c) after removing particles with code 103 using the magnetic tweezer. (d) Bright field image of (c).

One can collect hydrogel particles from selective microwells for relocation, further analysis, or discarding. We investigated selective manipulation of individual magnetic particles using magnetic tweezer. As shown in Figure 5-9, two types of particles were used. We used magnetic tweezers to successfully remove only the particles with code 103 from the microwell array. We applied a lower current to the magnetic tweezer than in our previous work,[34] in order to provide better tweezing resolution. A current of I = 0.15 A provided a strong enough force to attract particles without disturbing other particles nearby. Also, the magnetic tweezer was able to pick up multiple particles, one at a time, enabling a more efficient collection. This is advantageous because one does not need to oscillate the applied currents every collection to de-magnetize the magnetic tweezer, which exhibits magnetic hysteresis. The maximum number of particles collected without turning the tweezer off was 43. These proof-of-concept experiments shows that particles can be collected effectively using a magnetic tweezer with precise control over single particles. Currently, this manual control might not be the most efficient way of particle collections, but can be dramatically improved with process automation.

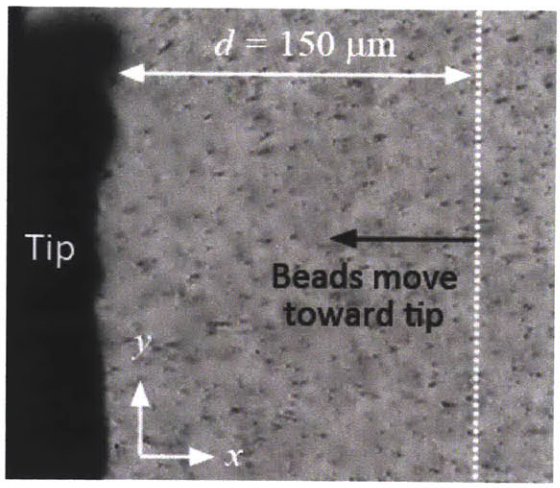

Figure 5-10: The set-up shown in Figure 5-3 was rotated 90 degree to observe vertical forces exerted on magnetic particles. The magnetic force was measured using drag force on magnetic beads.

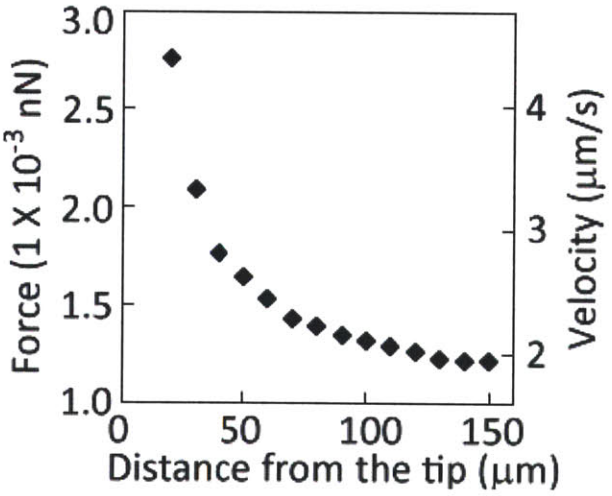

Figure 5-11: Average magnetic force exerted on one magnetic bead and average velocity as a function of distance from the tweezer tip.

To understand the magnetic forces we apply to the microparticles, we investigated the response of magnetic beads to a magnetic tweezer. With our experimental setup, only the horizontal forces can be measured, though the collection of barcode particles was based forces in the vertical direction. For a more accurate measurement, we rotated the tweezer 90°. Figure 5-11 shows the average velocity of magnetic beads as a function of distance from the tip of the magnetic tweezer.

The velocity of the beads increased as they approached the tip, where the largest gradient existed in the magnetic field. The drag force for steady viscous drag on a sphere can be calculated from Stokes' Law

$$F_{drag} = -6\pi\mu a U \tag{5-1}$$

where μ is the dynamic viscosity of the dispersed medium, a is radius of the bead, and U is the bead velocity. Assuming that the inertia is negligible, sum of the magnetic force and the drag force is zero (F_{mag} = -F_{drag}). As the distance from the barcode particles to the tip of magnetic tweezer was ~150 μm for particle collection, we obtained the velocity of the magnetic beads at the same distance, finding the average to be 1.9 μm/s. Using the equation above, the calculated magnetic force exerted on one magnetic bead was 1.2×10^{-3} nN. We note that the value is smaller than that found in our previous work due to the smaller volume of magnetic beads used here.[34] To calculate the magnetic force exerted on the microparticles, we assumed that all magnetic beads embedded within experience same force. We multiplied an estimated number of magnetic beads in microparticles to the force exerted on each, resulting in a total magnetic force on one barcode particle of ~22 nN. The magnetic force calculated represents the upper bound, as not all beads are 150 μm from the tips. There are two more forces related to magnetic particle collection: gravitational and buoyancy forces. For simplicity, we defined F_g as the summation of both. Using an estimated density of barcoded particle (ρ_p = 1.05 mg/ml) and a density of suspended solution (ρ_s = 0.998 mg/ml), F_g was calculated with the following equation

$$F_g = g\left(\rho_p - \rho_s\right)V \tag{5-2}$$

where g is the gravitational acceleration, and V is the volume of particles. The ratio between the magnetic to gravitational force exerted on a particle (F_{mag}/F_g) was 83. We note that this is the initial value, as the magnetic force (Figure 5-11) increases as particles approach the tip. It is possible larger forces are needed for manipulation in some cases; for example, recovery from sticky surfaces. In this case, the spaces between wells can be designed more carefully, in order to accommodate the force required to manipulate individual particles without disrupting neighboring particles.

5.4 Conclusion

We developed a new technique to prepare and manipulate magnetic hydrogel particles and arrange them in microwells using external magnetic forces. First, we demonstrated a modified synthesis process to remove magnetic debris from magnetic barcoded particles without the loss of biological functionality; we increased versatility significantly by enabling dual functionalities

in each region. We also showed that the magnetic particles could be efficiently manipulated to occupy substrate-patterned microwells for use in small volume analysis procedures. Furthermore, we selectively collected individual magnetic particles from the wells using a magnetic tweezer. The combination of encoded hydrogel particles with patterned substrates may be used to enable high-throughput analysis of small-volume multiplexed bioassays, chemical reaction, or single-cell analysis. Although most of the applications shown here are focused on bioassays, this versatile technique can be used for other methods including the templating of large arrays of gel pads. In addition, particles can be recovered from or repositioned in wells using magnetic forces, allowing even more complex patterns to be built.

5.5 Reference

(1) Miltenyi, S.; Müller, W.; Weichel, W.; Radbruch, A. *Cytometry* **1990**, *11*, 231.

(2) Bucak, S.; Jones, D. A.; Laibinis, P. E.; Hatton, T. A. *Biotechnol Progr* **2003**, *19*, 477.

(3) Stevens, P. D.; Fan, J.; Gardimalla, H. M. R.; Yen, M.; Gao, Y. *Organic Letters* **2005**, *7*, 2085.

(4) Pankhurst, Q. A.; Connolly, J.; Jones, S. K.; Dobson, J. *J Phys D Appl Phys* **2003**, *36*, R167.

(5) Mornet, S.; Vasseur, S.; Grasset, F.; Duguet, E. *J Mater Chem* **2004**, *14*, 2161.

(6) Jung, J. H.; Kim, G.-Y.; Seo, T. S. *Lab on a Chip* **2011**, *11*, 3465.

(7) Yin, S. N.; Wang, C. F.; Yu, Z. Y.; Wang, J.; Liu, S. S.; Chen, S. *Advanced Materials*, *23*, 2915.

(8) Pamme, N.; Manz, A. *Analytical chemistry* **2004**, *76*, 7250.

(9) Lee, H.; Kim, J.; Kim, H.; Kwon, S. *Nature Materials* **2010**, *9*, 745.

(10) Choi, J. W.; Oh, K. W.; Thomas, J. H.; Heineman, W. R.; Halsall, H. B.; Nevin, J. H.; Helmicki, A. J.; Henderson, H. T.; Ahn, C. H. *Lab on a Chip* **2001**, *2*, 27.

(11) Peyman, S. A.; Iles, A.; Pamme, N. *Lab on a Chip* **2009**, *9*, 3110.

(12) Doyle, P. S.; Bibette, J.; Bancaud, A.; Viovy, J. L. *Science* **2002**, *295*, 2237.

(13) Saliba, A.-E.; Saias, L.; Psychari, E.; Minc, N.; Simon, D.; Bidard, F.-C.; Mathiot, C.; Pierga, J.-Y.; Fraisier, V.; Salamero, J.; Saada, V.; Farace, F.; Vielh, P.; Malaquin, L.; Viovy, J.-L. *Proceedings of the National Academy of Sciences of the United States of America* **2010**, *107*, 14524.

(14) Slovakova, M.; Minc, N.; Bilkova, Z.; Smadja, C.; Faigle, W.; Futterer, C.; Taverna, M.; Viovy, J. L. *Lab on a Chip* **2005**, *5*, 935.

(15) Xu, F.; Wu, C. M.; Rengarajan, V.; Finley, T. D.; Keles, H. O.; Sung, Y.; Li, B.; Gurkan, U. A.; Demirci, U. *Advanced Materials* **2011**, *23*, 4254.

(16) Gunn, N. M.; Chang, R.; Westerhof, T.; Li, G. P.; Bachman, M.; Nelson, E. L. *Langmuir* **2010**, *26*, 17703.

(17) Bong, K. W.; Chapin, S. C.; Doyle, P. S. *Langmuir* **2010**, *26*, 8008.

(18) Pregibon, D. C.; Toner, M.; Doyle, P. S. *Science* **2007**, *315*, 1393.

(19) Chapin, S. C.; Appleyard, D. C.; Pregibon, D. C.; Doyle, P. S. *Angewandte Chemie* **2011**, *123*, 2337.

(20) Appleyard, D. C.; Chapin, S. C.; Doyle, P. S. *Analytical Chemistry* **2011**, *83*, 193.

(21) Srinivas, R. L.; Chapin, S. C.; Doyle, P. S. *Analytical Chemistry* **2011**, *83*, 9138.

(22) Chapin, S. C.; Pregibon, D. C.; Doyle, P. S. *Lab on a Chip* **2009**, *9*, 3100.

(23) Lindström, S.; Andersson-Svahn, H. *Biochimica et Biophysica Acta (BBA)-General Subjects* **2010**, *1810*, 308.

(24) Love, J. C.; Ronan, J. L.; Grotenbreg, G. M.; van der Veen, A. G.; Ploegh, H. L. *Nature Biotechnology* **2006**, *24*, 703.

(25) Seiffert, S.; Romanowsky, M. B.; Weitz, D. A. *Langmuir* **2010**.

(26) Yuet, K. P.; Hwang, D. K.; Haghgooie, R.; Doyle, P. S. *Langmuir* **2010**, *26*, 4281.

(27) Dyab, A. K. F.; Ozmen, M.; Ersoz, M.; Paunov, V. N. *J Mater Chem* **2009**, *19*, 3475.

(28) Kim, S. H.; Sim, J. Y.; Lim, J. M.; Yang, S. M. *Angew Chem Int Edit* **2010**, *49*, 3786.
(29) Lammerding, J., Massachusetts Institute of Technology, 2004.
(30) Fessenden, R. J.; Fessenden, J. S.; Logue, M. W. *Organic Chemistry*; 6th ed.; Brooks/Cole Publishing Co.: Pacific Grove, CA, 1998.
(31) Suh, S. K.; Bong, K. W.; Hatton, T. A.; Doyle, P. S. *Langmuir* **2011**, *27*, 13813.
(32) Cai, H.; Cao, X.; Jiang, Y.; He, P.; Fang, Y. *Analytical and Bioanalytical Chemistry* **2003**, *375*, 287.
(33) Zhang, J.; Xu, S.; Kumacheva, E. *Journal of the American Chemical Society* **2004**, *126*, 7908.
(34) Rich, J. P.; Lammerding, J.; McKinley, G. H.; Doyle, P. S. *Soft Matter* **2011**, *7*, 9933.

Chapter 6

Conclusions and Outlook

In this thesis, three new approaches to synthesize superparamagnetic units containing magnetic nanoparticles have been discussed. The primary focus of the thesis was the creation of magnetic particles with various morphologies and chemistries. We have characterized the properties of those particles and developed understanding of their synthesis processes. We also explored the use of our magnetic particles for biomolecule detection as used in clinical diagnostics.

In Chapter 2, we described a method for clustering magnetic nanoparticles and polymer particles using emulsions, controlling both the structure and coating layer of the resulting clusters. This technique provides a simple and versatile means to create uniquely-structured nanoparticle assemblies. The process is also scalable, showing great promise for a wide range of applications requiring large quantities of sophisticated magnetic materials.

In Chapter 3, we described a method to create micro particles with strong magnetic properties by combining stop-flow-lithography and *in-situ* co-precipitation. This new process, involving the post-synthesis of nanoparticles on hydrogel particle substrates also introduces new classes of responsive microparticles that exhibit interesting behaviors in magnetic fields in both static conditions or under flow. These particles can also be functionalized effectively to be used for high-throughput screening in biological and chemical processes.

In Chapter 4, we discussed the understanding of the process of hydrogel particle synthesis using stop-flow-lithography in the presence of opaque monomer constituents. This investigation into the synthesis mechanism can provide a guideline to design new opaque materials. Also, the technique provides a means of generating two independent anisotropies in one particle, enabling the assembly of new structures with external fields.

In Chapter 5, we demonstrated the manipulation of magnetic particles using magnetic field, locating magnetic particles in wells and collecting them using a magnetic tweezer. This technique gives freedom to handle individual particles during chemical processes for many applications. We showed the use of this process for biomolecule detection at low concentration by utilizing microwells containing a much smaller volume than in typical assays.

Although we have put a great effort in developing and understanding the synthesis systems, further work can improve the workflow or add more flexibility. In this chapter, we discuss a few aspects of the future work regarding the clustering of nanoparticles, post-synthesis of magnetic nanoparticles on polymer particles, and photo polymerization in the presence of magnetic beads.

6.1 Clusters of magnetic nanoparticles

In Chapter 2, we demonstrated the clustering of nanoparticle and polymers to generate submicron size magnetic units. Although we developed a robust process to create 100 – 200 nm size of clusters, each resulting batches typically had polydisperse size distributions. Using this method, the emulsions created are macroemulsions that are not thermodynamically stable, leading them to coalesce with nearby emulsions. One possible solution to this problem would be the use of membrane emulsification, as it results in narrow size distributions with small take-up volumes.

The clusters are stable in aqueous solutions; however, they are required to have stronger mechanical stability for use in many applications. To this end, one can create one more layer of shells not only to protect the clusters but also to add functionality. This can be realized by polymerizing the clusters with desirable materials or by using polymerizable surfactants. In collaboration with Emily Chang of the Hatton lab, we are perusing these ideas.

Using emulsions as a template, other nanoparticles, such gold, can be contained as long as the ligands are compatible with oil phase solvents. We synthesized gold nanoparticles stabilized with 1-octadecanethiol as well as gold and polystyrene Janus particles. This proof-of-principle experiment demonstrates the feasibility to of using emulsions as universal templates to create

nanoparticles clusters. If one can stabilize gold nanoparticles with a temperature-responsive polymer, gold Janus particles can be used for cell uptake and drug release.

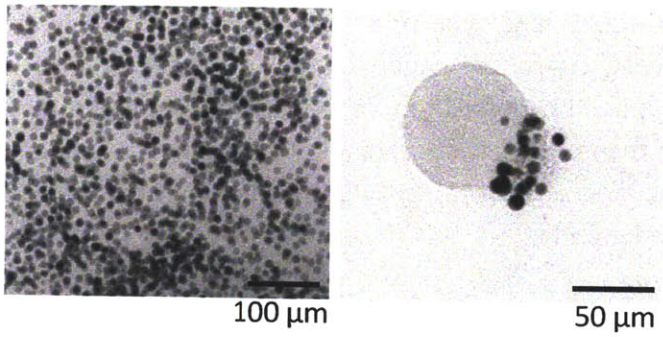

Figure 6-1: TEM images of gold nanoparticle and Janus particles.

Although we showed that the pervaporation can be used to reduce the time required for oil phase solvent removal, the conditions of this process can be optimized and modeled to obtain the desired internal structures of the clusters. Although we only used hexane with the unit, it would be interesting to create Janus particles using two oil phase solvents. This can be accomplished by changing the gas phase surrounding two pervaporation membranes as illustrated in Figure 6-2.

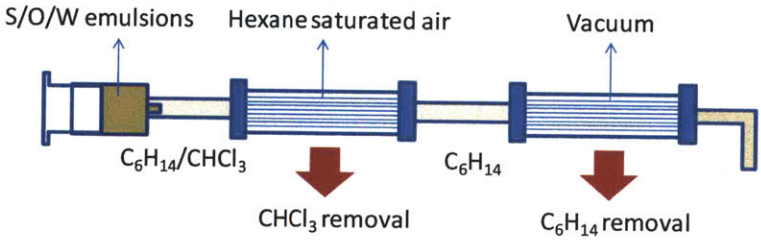

Figure 6-2: Schematic diagram of pervaporation modules used to obtain Janus type clusters.

6.2 Non-spherical magnetic microparticles

We created magnetic particles with strong magnetizations by repeating the co-precipitation of magnetite. Since there are remaining carboxylic groups after magnetite growth, we can increase the magnetization of micro particles with a second deposition. Similarly, we can have used these

carboxyl sites for other functionalizations. As a proof of concept, we attached single stranded DNA in magnetic micro particles.

Although we only synthesized one type of nanoparticles in micro hydrogel particles, one can easily distribute different types of nanoparticles over the hydrogel substrate using co-precipitation. For example, the deposition of conducting nanoparticles and/or light emitting materials can applied to many fields such as display technology where one can take advantage of various particle shapes. By successive growth of nanoparticles, the properties of hydrogel particles can be enhanced greatly.

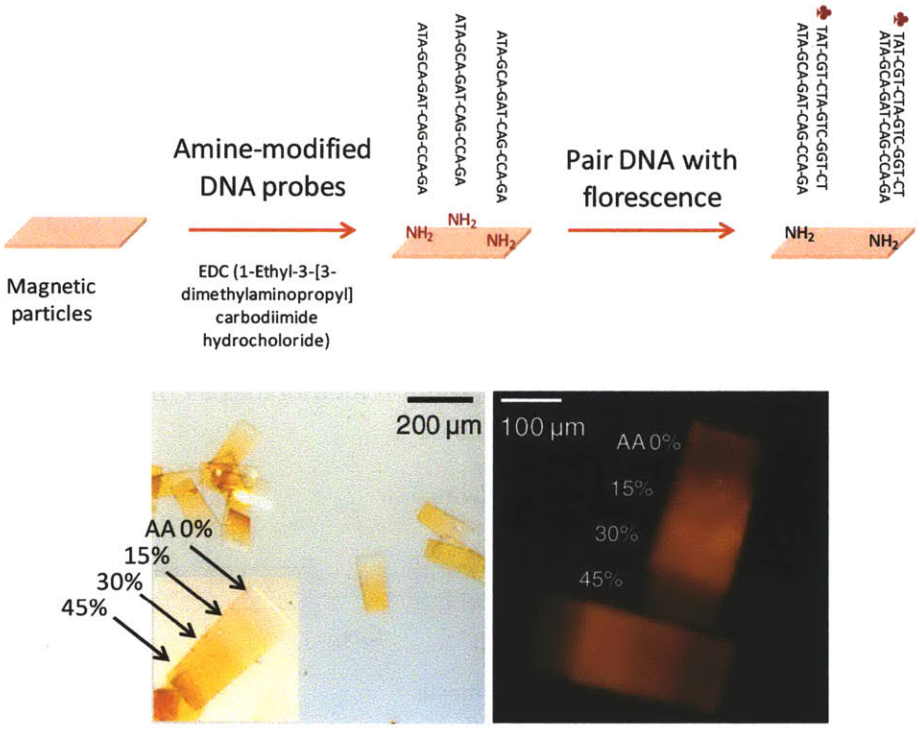

Figure 6-3: Procedure to create magnetic particles functionalized with DNA. The optical images show gradient magnetic particles before and after second functionalization.

6.3 Opaque particles

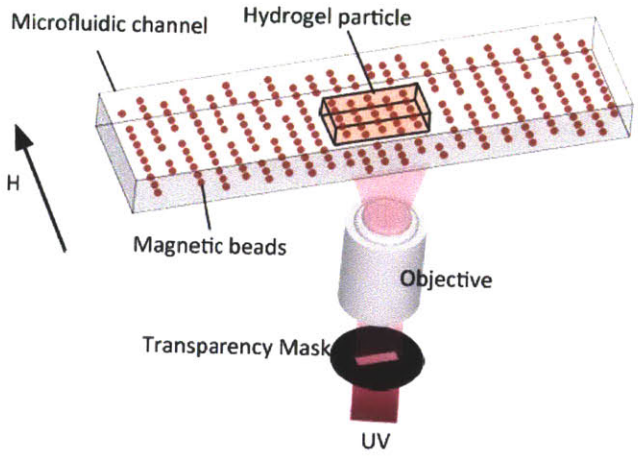

Figure 6-4: Chaining of magnetic bead under uniform magnetic field during polymerization of particles. The optical image shows created particles using the described method.

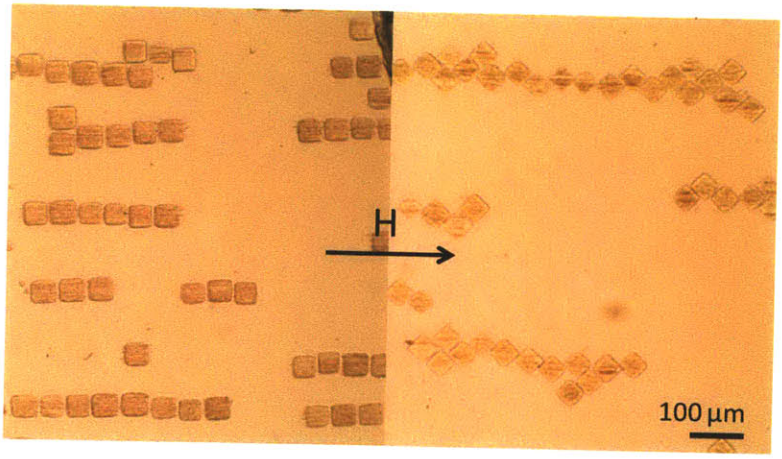

Figure 6-5: Assemblies of hydrogel particles containing magnetic chain under a uniform magnetic field. Magnetic beads were chained during the synthesis of particles.

We created hydrogel particles in the presence of a vertical magnetic field in order to understand the effects of UV absorption on the polymerization process; the presence of a field during synthesis allows us to create particles with two independent anisotropies. As vertical and horizontal magnetic fields can bring different anisotropies, the polymerization of monomer and magnetic beads under horizontal magnetic field can be pursued as shown in Figure 6-4.

As a proof of concept, we created particles of the same shape with anisotropies in different directions. The particles were assembled differently depending on the angle of the magnetic chains embedded in the particles as shown in Figure 6-5. One can build interesting structures mixing various shapes and anisotropies of particles. This work can be a starting point for future development in this area.

Magnetic hydrogel particles we created can be used for interesting assemblies. By assigning the directions of magnetic anisotropies during the polymerization, responses of those particles to the uniform magnetic field will depend on the designed anisotropies. We performed proof of concept experiments as shown in Figure 6-5. Both particles have same shape and size, while they assemble in different way under same uniform magnet field. If the assembled structure is useful for a certain application, one can polymerize the structure after assemblies.